

NON-PARAMETRIC AND SEMI-PARAMETRIC REGIONAL MODELING OF  
THE IONOSPHERIC VERTICAL TOTAL ELECTRON CONTENT USING  
GROUND-BASED GPS OBSERVATIONS

A THESIS SUBMITTED TO  
THE GRADUATE SCHOOL OF NATURAL AND APPLIED SCIENCES  
OF  
MIDDLE EAST TECHNICAL UNIVERSITY

BY

MURAT DURMAZ

IN PARTIAL FULFILLMENT OF THE REQUIREMENTS  
FOR  
THE DEGREE OF DOCTOR OF PHILOSOPHY  
IN  
GEODETICS AND GEOGRAPHICAL INFORMATION TECHNOLOGIES

SEPTEMBER 2013



Approval of the thesis:

**NON-PARAMETRIC AND SEMI-PARAMETRIC REGIONAL  
MODELING OF THE IONOSPHERIC VERTICAL TOTAL ELECTRON  
CONTENT USING GROUND-BASED GPS OBSERVATIONS**

submitted by **MURAT DURMAZ** in partial fulfillment of the requirements for the degree of **Doctor of Philosophy in Geodetics and Geographical Inf. Tech. Department, Middle East Technical University** by,

Prof. Dr. Canan ÖZGEN \_\_\_\_\_  
Dean, Graduate School of **Natural and Applied Sciences**

Prof. Dr. Ahmet ÇOŞAR \_\_\_\_\_  
Head of Department, **Geodetics and Geographical Inf. Tech.**

Prof. Dr. Mahmut Onur KARSLIOĞLU \_\_\_\_\_  
Supervisor, **Civil Engineering Dept., METU**

**Examining Committee Members:**

Prof. Dr. Gerhard-Wilhelm WEBER \_\_\_\_\_  
Institute of Applied Mathematics, METU

Prof. Dr. Mahmut Onur KARSLIOĞLU \_\_\_\_\_  
Civil Engineering Dept., METU

Prof. Dr. Zuhal AKYÜREK \_\_\_\_\_  
Civil Engineering Dept., METU

Assoc. Prof. Dr. Uğur Murat LELOĞLU \_\_\_\_\_  
Geodetics and Geographical Inf. Tech. Dept., METU

Assist. Prof. Dr. Kamil TEKE \_\_\_\_\_  
Geomatics Eng. Dept., Hacettepe University

**Date:** \_\_\_\_\_

**I hereby declare that all information in this document has been obtained and presented in accordance with academic rules and ethical conduct. I also declare that, as required by these rules and conduct, I have fully cited and referenced all material and results that are not original to this work.**

Name, Last Name: MURAT DURMAZ

Signature :

# ABSTRACT

## NON-PARAMETRIC AND SEMI-PARAMETRIC REGIONAL MODELING OF THE IONOSPHERIC VERTICAL TOTAL ELECTRON CONTENT USING GROUND-BASED GPS OBSERVATIONS

DURMAZ, Murat

Ph.D., Department of Geodetics and Geographical Inf. Tech.

Supervisor : Prof. Dr. Mahmut Onur KARSLIOĞLU

September 2013, 136 pages

Different global and regional models have been proposed for modeling of Vertical Total Electron Content(VTEC). Basis functions such as Spherical Harmonics and tensor products of univariate B-Splines are used for global and regional modeling respectively. The coefficients of the basis functions and Differential Code Biases (DCB) of satellites and receivers are treated as parameters and estimated from geometry-free linear combinations. In this work, a new approach based on non-parametric and semi-parametric methods is proposed to model spatio-temporal variations of VTEC. Multivariate Adaptive Regression Splines (MARS) and B-splines (BMARS) are adapted for regional VTEC modeling. Moreover, a semi-parametric modeling technique is developed where receiver DCBs can also be estimated. The parametric part of the semi-parametric model represents the receiver DCBs, whereas the non-parametric part is related to VTEC. The developed methods are implemented in an extensible software package. Both methods are applied to regional VTEC modeling over different regions and times. The results are compared both numerically and visually with another regional method and Global Ionosphere Maps (GIMs) provided by Center for Orbit Determination in Europe (CODE). The estimated receiver DCBs are also compared with the estimates of the other regional method and the ones that are published by CODE. Analysis of the results show that the developed technique can deliver similar VTEC maps and receiver DCB estimates with less number of terms. Additionally, the proposed method is validated by cross-validation and single-frequency point positioning indicating that the developed method is capable of delivering efficient and accurate regional VTEC models which provide better positioning estimates.

Keywords: MARS, BMARS, Semi-parametric, Ionosphere Modeling, Vertical Total Electron Content

# ÖZ

## YERSEL GPS ÖLÇÜMLERİ KULLANARAK BÖLGESEL İYONOSFERİK DİKEY TOPLAM ELEKTRON MİKTARININ YARI PARAMETRİK VE PARAMETRE DIŐI MODELLENMESİ

DURMAZ, Murat

Doktora, Jeodezi ve Coğrafi Bilgi Teknolojileri Bölümü

Tez Yöneticisi : Prof. Dr. Mahmut Onur KARSLIOĐLU

Eylül 2013 , 136 sayfa

Küresel ve bölgesel Dikey Toplam Elektron Miktarı (DTEİ) modellemesi için deđişik modeller önerilmiştir. Küresel modelleme için Küresel Harmonikler , bölgesel modelleme için ise tek deđişkenli B-Spline'ların tensör çarpımları gibi baz fonksiyonları kullanılmaktadır. Baz fonksiyonlarının katsayıları ve aynı zamanda Frekans Arası Gecikmeler (Differential Code Bias - DCB) parametre olarak belirlenir ve geometri bağımsız lineer kombinasyon ölçümlerinden kestirilirler. Bu çalışmada DTEİ'nin uzay-zamansal modellenmesi için yarı-parametrik ve parametre dışı yöntemlere dayalı yeni bir yaklaşım önerilmektedir. Bölgesel DTEİ modellemesi için Çoklu Uyabilen Spline (MARS) ve B-spline (BMARS) Regresyonu uryarlanmaktadır. Dahası, alıcı DCB değerlerinin kestirilebilmesi için yarı-parametrik modelleme tekniđi geliştirilmektedir. Yarı-parametrik modellemenin parametrik kısmı alıcı DCB değerleri ile, parametre dışı olan bölüm ise DTEİ ile ilgilidir. Bu yöntemler genişletilebilir bir yazılım kütüphanesi olarak geliştirilmektedir. Her iki yöntem de farklı bölgelerde ve zamanlarda bölgesel DTEİ modellemesi için uygulanmıştır. Sonuçlar hem görsel hem de sayısal olarak başka bir bölgesel modelleme yöntemi ve CODE tarafından yayınlanan Küresel İyonosfer Haritaları ile karşılaştırılmaktadır. Kestirilen alıcı DCB değerleri de diđer bölgesel modelleme yöntemi tarafından kestirilenler ve CODE tarafından yayınlananlar ile karşılaştırılmaktadır. Sonuçların analizi göstermektedir ki geliştirilen yöntem daha az sayıda terim kullanarak benzer DTEİ ve alıcı DCB kestirimleri üretebilmektedir. Dahası, önerilen method çapraz-geçerleme (cross-validation) ve tek frekanslı pozisyonlama ile geçerlenmektedir. Sonuçlar geliştirilen yöntemin daha iyi pozisyonlama kestirimleri veren etkin

ve dođru bölgesel DTEİ modelleri ürettiđini göstermektedir.

Anahtar Kelimeler: MARS, BMARS, Yarı-Parametrik, İyonosfer Modellemesi, Dikey  
Toplam Elektron Miktarı

*To my family...*

## ACKNOWLEDGMENTS

I would like to thank my supervisor Prof. Dr. Mahmut Onur KARSLIOĞLU for his endless support and guidance throughout my work. His friendly motivation, critical comments and suggestions and understanding was the driving force behind this work.

I would like to give my appreciation and thanks to the thesis jury members Prof. Dr. Zuhall AKYÜREK, Prof. Dr. Gerhard-Wilhelm Weber, Assoc. Prof. Dr. Ugur Murat LELOGLU and Assist. Prof. Dr. Kamil TEKE for their valuable suggestions, comments and critics.

I would like to thank my colleagues at work for their continuous support, motivation and understanding. It would be very hard to finish such a work without their friendship.

The GPS data and other products used in this thesis are based on the data archives of UNAVCO, IGS, CODE and EUREF which are greatly acknowledged.

Additionally, I am grateful for GPS data provided by Scientific and Technological Research Council of Turkey – Marmara Research Center (TUBITAK – MAM).

Without the endless support, motivation and understanding of my wife Melek Eda, I could not overcome the difficulties of finishing this work. The joy and energy from my daughter Ecem and son Can helped me to recover from hard times easily.

# TABLE OF CONTENTS

ABSTRACT . . . . .	v
ÖZ . . . . .	vii
ACKNOWLEDGMENTS . . . . .	x
TABLE OF CONTENTS . . . . .	xi
LIST OF TABLES . . . . .	xvi
LIST OF FIGURES . . . . .	xvii
CHAPTERS	
1 INTRODUCTION . . . . .	1
1.1 Motivation . . . . .	1
1.2 Objectives . . . . .	4
1.3 Methodology . . . . .	5
1.4 Thesis Structure . . . . .	5
2 OBSERVATION AND MODELING OF THE IONOSPHERE . . . . .	7
2.1 Ionosphere . . . . .	7
2.1.1 Regions of the Ionosphere . . . . .	8
2.1.2 Ionospheric Variations . . . . .	10
2.1.3 Ionospheric Effects on Wave Propagation . . . . .	12
2.2 Observation Methods . . . . .	14

2.2.1	Ionosonde . . . . .	14
2.2.2	Incoherent Scatter Radar . . . . .	15
2.2.3	Satellite Altimetry . . . . .	15
2.2.4	GNSS . . . . .	15
2.3	Global Ionosphere Models . . . . .	16
2.3.1	Klobuchar Model . . . . .	16
2.3.2	International Reference Ionosphere . . . . .	17
2.3.3	IGS Global Ionosphere Maps . . . . .	18
2.3.4	Global Assimilation of Ionospheric Measurements . . . . .	19
2.4	Local and Regional Ionosphere Models . . . . .	19
3	THE GLOBAL POSITIONING SYSTEM . . . . .	21
3.1	GPS Segments . . . . .	21
3.1.1	Space Segment . . . . .	22
3.1.2	Control segment . . . . .	23
3.1.3	User Segment . . . . .	24
3.2	GPS Observables . . . . .	25
3.2.1	Code Pseudo-ranges . . . . .	25
3.2.2	Carrier Phases . . . . .	26
3.2.3	Cycle-Slip Handling . . . . .	27
3.2.4	Error sources . . . . .	28
3.2.5	Code Smoothing . . . . .	29
3.3	Point Positioning . . . . .	29
3.3.1	Single Frequency Point Positioning . . . . .	30

	3.3.1.1	Point Positioning with Code Pseudo-ranges	31
	3.3.1.2	Point Positioning with Carrier Phases . . .	32
	3.3.1.3	Applying Atmospheric Corrections . . . . .	33
	3.3.2	Precise Point Positioning . . . . .	35
3.4		Extracting TEC from GPS Observables . . . . .	36
4		REGIONAL MODELING OF VTEC . . . . .	39
4.1		Reference Systems and Frames . . . . .	40
	4.1.1	The World Geodetic System - WGS84 . . . . .	40
	4.1.2	Spherical System . . . . .	41
	4.1.3	Sun-fixed Reference Frame . . . . .	41
	4.1.4	Sun-fixed Geomagnetic Reference Frame . . . . .	42
4.2		Observation Equation . . . . .	43
4.3		Parametric Modeling of VTEC . . . . .	45
	4.3.1	VTEC Modeling with Spherical Harmonics . . . . .	48
	4.3.2	Regional VTEC Modeling with B-splines . . . . .	49
4.4		Non-parametric Modeling of VTEC . . . . .	49
	4.4.1	Non-parametric Modeling with MARS . . . . .	50
		4.4.1.1 MARS Basis Functions . . . . .	50
		4.4.1.2 MARS Algorithm . . . . .	52
	4.4.2	Non-Parametric Modeling with BMARS . . . . .	59
		4.4.2.1 BMARS Basis Functions . . . . .	59
		4.4.2.2 BMARS Algorithm . . . . .	62
4.5		Semi-Parametric Modeling of VTEC . . . . .	68

4.5.1	Extensions and Limitations . . . . .	70
5	APPLICATIONS . . . . .	73
5.1	Regional Non-Parametric VTEC Modeling . . . . .	73
5.1.1	Regional VTEC Modeling with MARS . . . . .	73
5.1.2	Regional VTEC Modeling with BMARS . . . . .	74
5.2	Regional Semi-Parametric VTEC Modeling . . . . .	75
5.2.1	Experiment Setup and Modeling . . . . .	76
5.2.1.1	Experiment Region . . . . .	76
5.2.1.2	Data Preparation . . . . .	80
	Observation and Navigation Files . . . . .	80
	IGS Orbit Products . . . . .	80
	Code DCB Estimates . . . . .	81
	Code GIMs . . . . .	81
	Extracting STEC . . . . .	82
5.2.1.3	Modeling . . . . .	82
5.2.2	Visual Comparison of Results . . . . .	83
5.2.3	Numerical Comparison of Results . . . . .	89
5.2.4	Validation Results . . . . .	94
5.2.4.1	Cross-Validation Results . . . . .	94
5.2.4.2	Point Positioning Results . . . . .	96
5.2.5	Discussions . . . . .	102
6	THE SOFTWARE . . . . .	107
6.1	Software Development Environment . . . . .	107

6.1.1	Python Development Environment . . . . .	108
6.1.2	Development with GPStk . . . . .	109
6.1.3	TECMapper . . . . .	109
6.2	Software Design . . . . .	110
6.2.1	Interfaces . . . . .	110
6.2.2	Software Modules . . . . .	113
6.2.2.1	BMARS . . . . .	113
6.2.2.2	IonTrace . . . . .	115
6.2.2.3	Utilities and Positioning . . . . .	116
7	CONCLUSION . . . . .	119
7.1	Future Work . . . . .	122
	REFERENCES . . . . .	123
	APPENDICES	
A	RECEIVER DCB ESTIMATES . . . . .	127
	CURRICULUM VITAE . . . . .	135

## LIST OF TABLES

### TABLES

Table 2.1	Ionospheric Regions according to ion composition . . . . .	9
Table 5.1	The ground stations used for VTEC modeling in the study . . . . .	78
Table 5.2	The RMS of differences between BMARS and both CODE GIMs and 3D-Bsplines for 8 March 2012 . . . . .	91
Table 5.3	The RMS of differences between BMARS and both CODE GIMs and 3D-Bsplines for 9 March 2012 . . . . .	91
Table 5.4	The RMS of differences between BMARS and both CODE GIMs and 3D-Bsplines for 10 March 2012 . . . . .	91
Table 5.5	The number of selected terms for BMARS models with different orders on 8, 9 and 10 March 2012 . . . . .	93
Table 5.6	Reference stations for point positioning with ECEF positions . . . . .	97
Table 5.7	Single-Frequency static point positioning results for day 8 March 2012	103
Table 5.8	Single-Frequency static point positioning results for day 9 March 2012	104
Table 5.9	Single-Frequency static point positioning results for day 10 March 2012	105

# LIST OF FIGURES

## FIGURES

Figure 2.1 Typical height profile of atmospheric temperature and electron density at mid latitudes . . . . .	8
Figure 2.2 Typical composition of the ionosphere at mid-latitudes for quite days	10
Figure 2.3 Monthly mean and 13 months smoothed sunspot numbers over last 60 years . . . . .	11
Figure 2.4 The drift of charged particles at the equator . . . . .	11
Figure 3.1 GPS constellation . . . . .	22
Figure 3.2 The distribution of the station and antennas of GPS Control Segment	24
Figure 3.3 Simple interpretation of phase observables and cycle-slips . . . . .	27
Figure 3.4 Single layer model for ionosphere . . . . .	37
Figure 4.1 The International Terrestrial Reference System and Ellipsoidal Coordinates . . . . .	41
Figure 4.2 The International Terrestrial Reference System and Spherical Coordinates . . . . .	42
Figure 4.3 The astronomical triangle formed by the North Pole (N), IPP and receiver (Rc) . . . . .	45
Figure 4.4 Sample piece-wise linear basis function . . . . .	52

Figure 4.5	Tensor product of piece-wise linear basis functions . . . . .	53
Figure 4.6	Tensor product of MARS cubic basis functions . . . . .	54
Figure 4.7	Sample BMARS basis functions . . . . .	61
Figure 4.8	Uniform B-splines with different levels . . . . .	62
Figure 4.9	BMARS basis functions with B-splines of order 1 for levels 1 and 2 defined over non-uniform data sampling . . . . .	63
Figure 4.10	BMARS basis functions with B-splines of order 2 for levels 1 and 2 defined over non-uniform data sampling . . . . .	64
Figure 4.11	BMARS basis functions with B-splines of order 1 and 2 for levels 2 over uniform data sampling . . . . .	65
Figure 5.1	The distributions of EUREF stations used in this study. Blue labeled stations are also used for CODE Global Ionosphere Models . . . . .	77
Figure 5.2	IPP coverages from some ground stations, as well as full day coverage from all selected stations on day 8 March 2012 with a decimation of 10 min.	79
Figure 5.3	Global and Regional VTEC maps for day 8th of March 2012 . . . . .	84
Figure 5.4	Global and Regional VTEC maps for day 9th of March 2012 . . . . .	85
Figure 5.5	Global and Regional VTEC maps for day 10th of March 2012 . . . . .	86
Figure 5.6	VTEC Difference Maps between different BMARS Models and CODE GIM on the 8th of March 2012 . . . . .	87
Figure 5.7	VTEC Difference Maps between different BMARS Models and CODE GIM on the 9th of March 2012 . . . . .	88
Figure 5.8	VTEC Difference Maps between different BMARS Models and CODE GIM on the 10th of March 2012 . . . . .	88
Figure 5.9	VTEC Difference Maps between different BMARS Models and 3D B-splines on the 8th of March 2012 . . . . .	89

Figure 5.10 VTEC Difference Maps between different BMARS Models and 3D B-splines on the 9th of March 2012 . . . . .	90
Figure 5.11 VTEC Difference Maps between different BMARS Models and 3D B-splines on the 10th of March 2012 . . . . .	90
Figure 5.12 RMSE of BMARS and 3D B-spline models for three days . . . . .	92
Figure 5.13 DCB estimates of selected ground stations for each days . . . . .	94
Figure 5.14 10-Fold Cross Validation Results of BMARS models with B-splines of different orders . . . . .	96
Figure 5.15 Ionospheric range delays calculated by CODE GIMs and BMARS d=2 on each day between the MEDI station and GPS satellite with PRN=4	101
Figure 6.1 Software block diagram . . . . .	110
Figure 6.2 Basic interfaces for Ionosphere modeling . . . . .	111
Figure 6.3 BMARS Module Class Diagram . . . . .	114
Figure 6.4 BMARS based Ionosphere Modeling class diagram . . . . .	115
Figure 6.5 IPP coverage and correction viewer utilities . . . . .	117
Figure 6.6 GPSTk based positioning module . . . . .	118
Figure A.1 DCB estimates for ground stations (ANKR, BUCU, CAGZ and GLSV from top to bottom) for each days . . . . .	127
Figure A.2 DCB estimates for ground stations (GRAZ, GUIP, HERS, INVR and ISTA from top to bottom) for each days . . . . .	128
Figure A.3 DCB estimates for ground stations (LEON, MALL, MAR6, MATE and METS from top to bottom) for each days . . . . .	129
Figure A.4 DCB estimates for ground stations (NEWL, NOA1, NOT1, ORID and OSLs from top to bottom) for each days . . . . .	130

Figure A.5 DCB estimates for ground stations (PAT0, PTBB, RIGA, SFER and STAS from top to bottom) for each days . . . . . 131

Figure A.6 DCB estimates for ground stations (SULP, SWKI, TUC2, VIS0 and YEBE from top to bottom) for each days . . . . . 132

Figure A.7 DCB estimates for ground stations ZIMM and GOPE for each days 133

# CHAPTER 1

## INTRODUCTION

This PhD thesis is about the study and the achievements on regional Vertical Total Electron Content (VTEC) modeling of the ionosphere with non-parametric and semi-parametric approaches. In the study, non-parametric and semi-parametric methods for VTEC modeling are adapted. Additionally, algorithms and software tools are developed for both data-processing and VTEC modeling using real ground-based Global Positioning System (GPS) observations. The next subsections describe the motivation behind the study, the objectives and the methodology applied. The structure of the thesis is given in the last section.

### 1.1 Motivation

Ionosphere is a reflective and refractive medium for electromagnetic waves. It is important to monitor and model the ionosphere since it affects communication systems, space based navigation systems and space weather, among others. Although ionospheric effects on electromagnetic waves are seemed to be a drawback for positioning and communication, it appears to be a valuable source of information related to the electron content of ionosphere (Schaer, 1999). Using geometry-free linear combination of code and phase observables from dual frequency GPS receivers, one can extract the total electron content (TEC) along the ray-path from the satellite to the receiver (Hofmann-Wellenhof et al., 2008). The integral of the number of electrons along the ray-path is usually called Slant Total Electron Content (STEC) and measured in units of TEC Units (TECU: 1TECU =  $10^{16}$  electrons/ $m^2$ ). Since the electron content is related to an integral along the ray-path, tomographic reconstruction of 3D or 4D ionospheric electron density is extensively studied in the literature (Liu and Gao, 2003; Pallares et al., 2005; Wen et al., 2007). However, limited reconstruction can be achieved when only ground-based observations are used. In order to increase the number of ray-paths at different angles, other measurement methods such as GPS radio-occultation from Low Earth Orbiting (LEO) satellites and satellite altimetry are used.

When ground based receivers are used to monitor and model the electron content, ionosphere can be simplified to a thin spherical shell with a certain height, which is assumed to represent all of the total electron content (Dettmering, 2003; Jin et al., 2008, 2006; Schaer, 1999). Then, STEC can be transformed into the Vertical Total Electron Content (VTEC) by an appropriate mapping function (Schaer, 1999). The spatio-temporal distribution of VTEC can be estimated as a 2D function in a Sun-fixed reference frame Dach et al. (2007); Schaer (1999). Another approach is to model VTEC in an Earth-fixed reference frame with geographic latitude and longitude for spatial distribution and time for temporal distribution (Nohutcu, 2009). There are plenty of studies related to the generation of regional or global VTEC maps in the literature (Brunini et al., 2004; Hernandez-Pajares and Sanz, 1999; Jin et al., 2004; Mannucci et al., 1998; Schaer, 1999; Schmidt et al., 007b; Yuan and Ou, 2002). Hernández-Pajares et al. (2011) provide a valuable review on the current state of the art in ionosphere modeling and outlook for further research areas. Spherical harmonics expansions are usually used to model global distribution of VTEC. It is an effective model as long as the data is evenly distributed (Hernández-Pajares et al., 2011). Different gridding techniques can be used to overcome irregular data and data gaps (Mautz et al., 2005; Yuan and Ou, 2002). For regional and local modeling, a multi-dimensional tensor product B-splines based approach is presented by Schmidt (2007), Schmidt et al. (007a,b), Zeilhofer (2008) and Nohutcu et al. (2010, 2007). Besides the parametric approaches, other methods such as krigging (Wielgosz et al., 2003), neural networks (Hernández-Pajares et al., 1997) have also been developed.

The geometry-free linear combination depends not only on spatio-temporal distribution of VTEC but also on Differential Code Biases (DCB) of satellites and receivers (Hernández-Pajares et al., 2011). Kao et al. (2013) have shown that estimates of DCBs of satellites and receivers are strongly related to the estimation accuracy of mathematical models representing the spatio-temporal distribution of VTEC. Thus a good mathematical model for spatial distribution of VTEC is also a key to the better receiver DCB estimations.

Main motivation of this study is to develop an adaptive and flexible regional VTEC model from ground-based GPS observations. Such a modeling approach can deliver models that have a good spatio-temporal representation of VTEC and receiver DCB estimations. An adaptive VTEC model can be built from the data at hand, assuming no prior mathematical form for the spatio-temporal distribution of VTEC. The model is built from the ground-based GPS observations in order to find a best fitting mathematical function, which also delivers a good prediction performance. A flexible VTEC model is a form of a mathematical function that can represent both linear and non-linear relationships among the predictor variables.

An algorithm named Multivariate Adaptive Regression Splines (MARS) introduced by Friedman (1991) can generate a flexible and adaptive multi-dimensional model. It uses truncated power-series as simple basis functions to build a regression function

that fits to the data and has a good prediction performance in terms of Generalized Cross Validation (GCV). In its simple form, the MARS algorithm searches for best-fitting piece-wise linear functions that have distinct knot locations at each observation point in the forward stage. This overfitting model is then reduced by eliminating the least significant terms leading to an optimized model in terms of GCV score in the backward stage. The algorithm can handle large number of predictor variables and large number of observations by utilizing an update formula while searching for candidate basis functions (Friedman, 1991). Moreover, it uses the observations directly without requiring gridding, scaling or a reference model for data gaps.

MARS algorithm can be adapted to produce adaptive and flexible VTEC models. This adoption can deliver interesting results for regional VTEC estimations. Due to the definition of its basis functions MARS in its basic form can not deliver smooth models. To overcome this issue MARS algorithm is extended to include cubic basis functions (Friedman, 1991). Although this extension can deliver smooth approximations the basic form of the basis functions remain the same and also they do not have compact support.

Bakin et al. (2000) introduced an extended version of the MARS algorithm named Multivariate Adaptive Regression B-splines (BMARS) by introducing compactly supported B-splines as basis functions. BMARS can produce smoother models depending on the order of B-splines used. The univariate B-splines are defined over the observation locations called knots on a scale-by-scale basis. At the largest scale BMARS searches for B-splines that define the overall representation of the data leading to large-scale features. When enough large scale features are added, smaller scale features are selected by decreasing the support of basis functions. With this approach the search space of BMARS basis functions is smaller compared to MARS. In this regard, BMARS algorithm can deliver smoother VTEC maps and can be an alternative modeling strategy to regional tensor-product univariate B-spline based modeling.

Non-parametric modeling can be used to find best fitting mathematical relationships between the VTEC observations and predictor variables (generally geographic latitude, longitude and time). However, they can be used if the VTEC observations are extracted from the geometry-free linear combinations. This can be achieved by subtracting known DCB values from the observations. Satellite DCB estimations are considered stable and can be downloaded from different analysis centers such as Centre of Orbit Determination in Europe (CODE). They also deliver receiver DCB estimations of ground stations that are used in global ionosphere modeling. Thus, for regional applications receiver DCBs of ground stations must be extracted from the observations or must be estimated to obtain VTEC.

Estimation of receiver DCBs with a non-parametric VTEC modeling can be accomplished by a semi-parametric modeling approach, where a combined model with unknown fixed-parameters of receiver DCBs and a non-parametric function of VTEC can

be estimated together. MARS algorithm can be modified to estimate both a parametric part and a non-parametric part (Friedman, 1991). The same approach can be adopted to BMARS to deliver both estimations of receiver DCBs and smooth VTEC distribution in regional applications. The semi-parametric approach inherits both parametric modeling and non-parametric modeling combining their strengths. In this regard the resulting VTEC model is adaptive and flexible, at the same time a good estimate of receiver DCBs can be obtained. Thus developing a semi-parametric method for VTEC modeling can not only leads to delivering adaptive and flexible VTEC models that fit better to the data, but also can give better estimates of the unknown receiver DCBs as well.

## 1.2 Objectives

With the motivation outlined in the previous section, the main goal of this PhD Thesis is to develop an adaptive and flexible spatio-temporal representation of the VTEC for regional applications. To achieve this goal the following objectives are considered:

- A non-parametric 2D and 3D VTEC modeling approach in both Sun-fixed and Earth-fixed reference frames should be developed. The method should be Implemented and tested with real GPS observations: MARS algorithm should be applied to build regional VTEC models using ground-based GPS observations.
- A non-parametric and smooth VTEC modeling approach should be developed. The method should be implemented and tested with real ground based GPS observations: BMARS algorithm should be applied to build regional VTEC models using ground-based GPS observations and compared with MARS algorithm results.
- A semi-parametric approach based on BMARS, which can also estimate the unknown receiver DCBs with VTEC at the same-time, should be developed. The method should be implemented and tested with ground-based GPS observations.
- A testing and validation framework for VTEC models to find their applicability for single frequency point-positioning should be developed.
- A software package should be developed that can handle the ground-based observations, implements the non-parametric and semi-parametric approaches. This package should be extensible to support further development and use open-source software whenever applicable.

### 1.3 Methodology

The methodology applied in the thesis mainly contains three stages which are summarized below.

- First stage: The mathematical formulation of VTEC modeling with MARS algorithm is developed. Scripting languages are used to adapt existing implementations of the MARS algorithm for regional VTEC modeling. And then, the algorithm is applied to regional VTEC modeling and compared to global ionosphere models visually and numerically.
- Second stage: VTEC modeling with BMARS algorithm is developed and implemented in MATLAB. The algorithm is then applied to regional VTEC modeling and compared to MARS and another regional VTEC model based on univariate tensor product B-splines.
- The Last stage: A semi-parametric method based on BMARS is developed for both VTEC and receiver DCB estimation. A software package is designed for data processing, VTEC representation and testing. The BMARS algorithm is ported to Python programming language. A single frequency point positioning tool is implemented in C++ programming language using GPStk open-source library. The algorithm is applied to regional VTEC modeling and receiver DCB estimation. The results are compared visually and numerically with both global ionosphere model and regional model. Furthermore, the VTEC models are validated by single frequency point positioning.

### 1.4 Thesis Structure

This PhD Thesis is organized as follows.

- **Chapter 1, Introduction:** The motivation, objectives, methodology and structure are given.
- **Chapter 2, Observation and Modeling of The Ionosphere:** Fundamental information of the structure and physics of the Ionosphere are summarized. Ionospheric measurement techniques and widely used Ionosphere models are introduced.
- **Chapter 3, The Global Positioning System:** A summary of the Global Positioning System with its segments and observables are given. Methods for point positioning and extracting ionospheric electron content from the observations are described.

- **Chapter 4, Regional Modeling of VTEC:** Widely used global and regional mathematical models for the ionosphere are introduced. Mathematical foundations for MARS and BMARS algorithms and their application to regional non-parametric VTEC modeling are explained in detail. Moreover, the regional semi-parametric VTEC modeling is extensively described.
- **Chapter 5, Applications:** The experimental setup and the observation data are illustrated in detail. The analysis and the results of applying non-parametric and semi-parametric modeling techniques are listed and compared to other modeling techniques both visually and numerically. The results of validation with single-frequency point positioning are shown both numerically and graphically.
- **Chapter 6, The Software:** The design and the development of the software package are described.
- **Chapter 7, Conclusion:** The conclusions of the study are presented and future research directions are outlooked.

## CHAPTER 2

# OBSERVATION AND MODELING OF THE IONOSPHERE

Ionosphere is the upper part of the atmosphere which is dominated by charged particles. The existence of such a layer in the atmosphere results in important consequences. Firstly, flow of electrical currents occur in the ionosphere leading to changes in magnetic field of earth. This affect was foreseen by Gauss in 1839 and later by Kelvin in 1860. Moreover, Ionosphere influences the space weather in upper atmosphere by affecting thermospheric winds. Finally, it disturbs the electromagnetic wave propagation by reflection, refraction, change of polarization and attenuation (Prölss, 2004). This effect helped Marconi to transmit radio-waves across the Atlantic.

The existence of Ionosphere is later proved by radio wave experiments conducted by two independent groups; Appleton and Bernet from England and Breit and Tuve from USA in 1924 (Prölss, 2004). Monitoring and modeling the Ionosphere is still an active research area today. This chapter provides a basic understanding of the structure and physics of the ionosphere and introduces mostly used observation methods. The next subsection gives an overview of the Ionosphere with its structure and variations. The following section presents the observation methods of the Ionosphere. Finally, a summary of global ionosphere models are given in the last section.

### 2.1 Ionosphere

The Ionosphere extends from 50 km to 1000 km in height above sea level. The main quantity that describes the ionosphere is the number of free electrons in unit volume. Free electrons are mainly a result of photoionization by the Ultra Violet (UV) light from the Sun. There are also various ionization and transportation processes leading to variations in electron content of the ionosphere. Moreover, charged particles coming from the sun also influence the Ionosphere especially when there is a solar storm. Ionosphere consists of different regions depending on height and particle diversity. The following subsections describe the layered structure of the Ionosphere and the variations within them.

### 2.1.1 Regions of the Ionosphere

As the main quantity describing the ionosphere is the electron density, a structure of the ionosphere can be defined depending on the density profile of the electrons with respect to height (Kelley, 2009). Fig. 2.1 presents change of the temperature and electron density with height. Various atmospheric and ionospheric regions are also shown. The atmospheric regions are distinguished by the temperature, whereas it is better to use the electron density (presented as plasma density in the figure) to distinguish the regions of the ionosphere namely D Region, E Region and F Region (Kelley, 2009). Also note the variation of the ionospheric electron density with day and night in the right subfigure of Fig. 2.1.

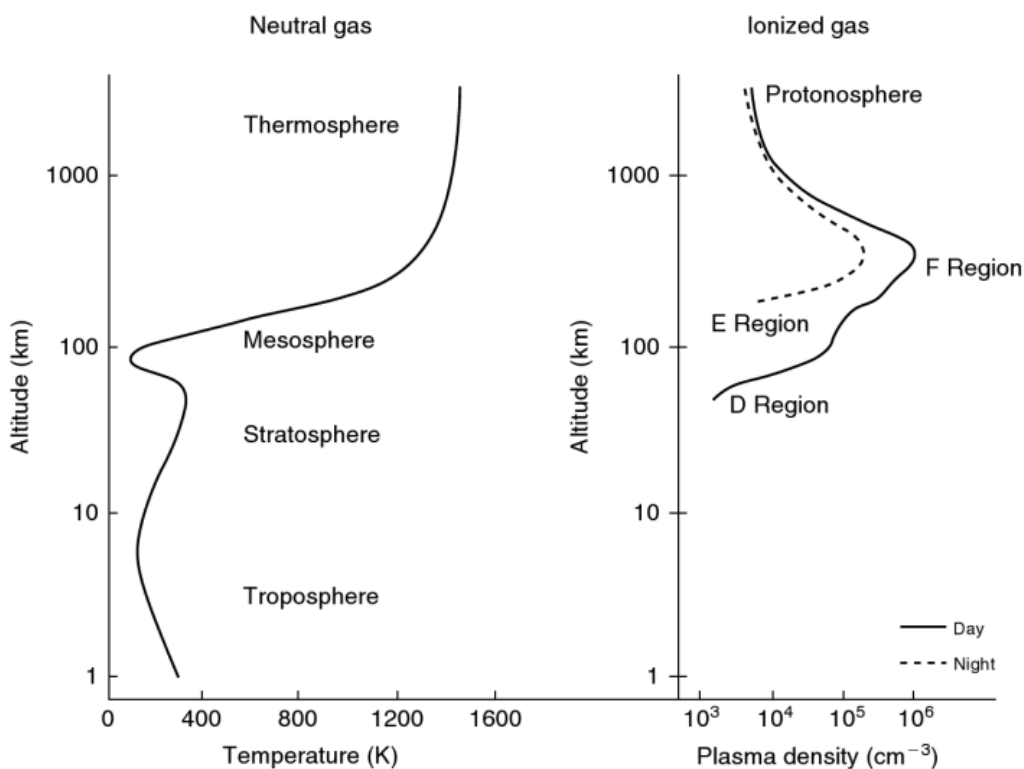


Figure 2.1: Typical height profile of atmospheric temperature and electron density at mid latitudes(Kelley, 2009)

Fig. 2.2 presents the ionic composition of the ionosphere (Prölss, 2004). The plasma density profile in Fig. 2.1 is shown with electron profile  $e^-$  in the figure. According to the figure at lower part of the ionosphere is dominated by the  $O_2^+$  and  $NO^+$  molecular ions, whereas  $O^+$  and  $H^+$  dominate the upper ionosphere. Prölss (2004) provides a classification of the ionospheric regions with typical height values and ion constituents in Table 2.1. The lower part of the ionosphere ranging from 50 to 90 km is called the D Region, where the positive and negative ions present. The ionization density

depends mainly on the sun light (see Fig. 2.1). The E Region, which consists of mainly  $O_2^+$  and  $NO^+$  ions, is above the D Region with heights ranging from 90 km to 170 km. The E Region is also called the Kennely-Heaviside layer for which the ionization density is caused by ultraviolet and X-rays in daytime, cosmic rays and meteors at night (Hofmann-Wellenhof et al., 2008). The region with dominated  $O^+$  above the E Region is called the F Region (also called Appleton Layer). The electron density depends mainly on the solar zenith angle. The number of electrons increases with Sun reaching its maximum at noon, and decreasing with sunset. The F Region is commonly split into two sub regions called F1 (150 to 200 km) and F2 (200 to 1000 km) during daytime. It is the F2 layer that contains the maximum number of electrons in the Ionosphere (Hofmann-Wellenhof et al., 2008).

Table 2.1: Ionospheric regions according to ion composition (Prölss, 2004)

Region	Height (h)	Ions
D Region	$h \lesssim 90$ km	$H_3O^+, (H_2O)_n, NO_3^-$
E Region	$90$ km $\lesssim h \lesssim 170$ km	$O_2^+, NO^+$
F Region	$170$ km $\lesssim h \lesssim 1000$ km	$O^+$
Plasmasphere	$h \gtrsim 1000$ km	$H^+$

Different processes contribute to the ion density inside the Ionosphere. Processes that contribute to the ion production and loss are listed below (see (Prölss, 2004) for further descriptions):

- Primary Photoionization:  $X + photon(\lambda \lesssim 100nm) \rightarrow X^+ + e$ . where  $X$  is one of the dominant gases  $O, N_2$  and  $O_2$  inside the atmosphere. Moreover, the photoelectrons released with high enough energy can attract other molecules which is called secondary ionization process.
- Charge Exchange: where the electrons are exchanged by neutral gas and positive ions.
- Particle Precipitation: The upper atmosphere can be ionized by precipitating electrons with high energy.  $X + e_p \rightarrow X^+ + e_p + e_s$ , where  $e_p$  is the primary electron with high energy,  $e_s$  is the secondary electron.
- Disassociative Recombination of Molecular Ions: where the electron is consumed by the molecular ion and separates the molecular ion into its constituents.  $XY^+ + e \rightarrow X^* + Y^*$ .
- Radiative Recombination: where the electron is consumed by the positive ion which results in an emission of photons.  $X^+ + e \rightarrow X^* + photon$ .

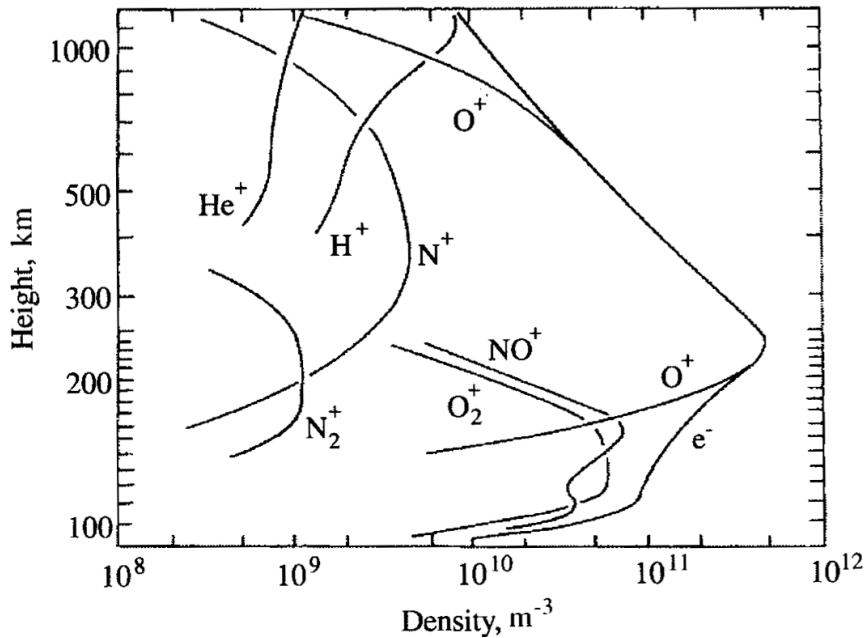


Figure 2.2: Typical composition of ionosphere at mid latitudes for quiet days (Prölss, 2004)

### 2.1.2 Ionospheric Variations

The Sun is the driving force of photoionization in the Ionosphere causing both temporal and spatial variations. Thus the electron content of the ionosphere changes with the solar zenith angle during day. It increases rapidly around 10h local-time and attains its maximum around local-time of 14h (Hofmann-Wellenhof et al., 2008). Moreover, the solar radiation intensity is another parameter for ion production rate. The radiation intensity coming out of the Sun depends on the solar cycle and its own rotation. The solar cycle has a period of 11 years (see Fig. 2.3), whereas the rotation of the Sun about its own axis of rotation is 27 days. The seasonal variations of the ionospheric electron content attain their maximums in spring and fall, whereas minimums occur at winter and summer (Hernández-Pajares et al., 2011). Coronal Mass Ejections (CME) cause geomagnetic storms over the Earth, affecting the Earth's magnetic field and Ionosphere. This results in strong spatial and temporal variations on the electron content and may affect signal transmissions through the Ionosphere. There are also short-term variabilities or irregularities inside the ionosphere called scintillations (periods in seconds) and traveling ionospheric disturbances (periods in minutes) (Seeber, 2003).

Spatial variations of the Ionosphere are observed since the atmospheric conditions change with latitude (especially the radiation intensity of the Sun). The special condition at the geomagnetic equator causes distinctive variations of the ionospheric electron content at low latitudes, which is called equatorial anomaly. Fig. 2.4 presents the mo-

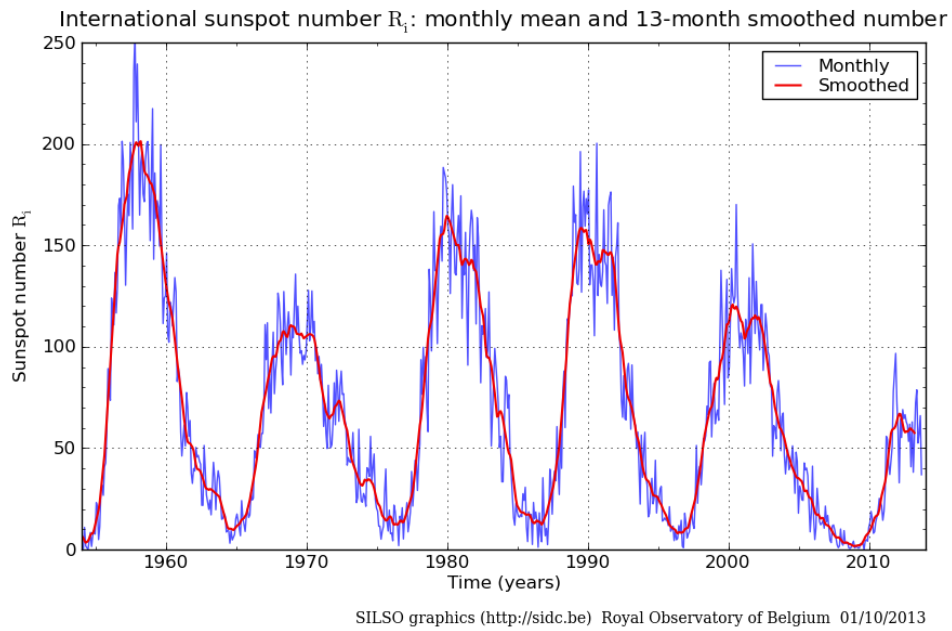


Figure 2.3: Monthly mean and 13 months smoothed sunspot numbers over last 60 years (Credit: Solar Influences Data Analysis Center, 2013)

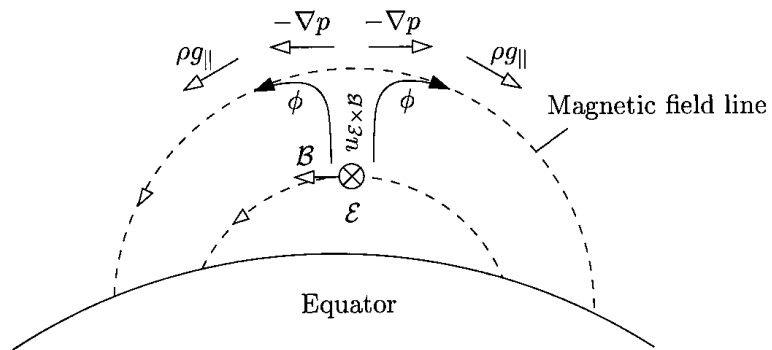


Figure 2.4: The drift of charged particles at the equator (Pröls, 2004)

tion of charged particles at the geomagnetic equator because of the west-to-east electric field  $\epsilon$  and the south-to-north magnetic field  $B$ . The drift causes the free electrons inside the F Region to be pushed to reach greater ionospheric heights and fall on both sides of the geomagnetic equator, which is generally called equatorial plasma fountain (Prölss, 2004).

### 2.1.3 Ionospheric Effects on Wave Propagation

Since the Ionosphere is a kind of plasma, electromagnetic waves propagating through it are affected by the electron content. The important effects related to the communication and GNSS can be listed as reflection, refraction and attenuation. The properties of reflection and refraction especially are important since they can deliver important characteristics of the medium that they propagate in (Prölss, 2004). Since the observations used in this study are based on the refraction of electromagnetic waves through the Ionosphere, we will focus on this property.

An electromagnetic wave with frequency  $f$  and wavelength  $\lambda$  propagates with the speed of light  $c$  in vacuum. The properties of light have the following well-known formula:

$$v_{ph} = f\lambda, \quad (2.1)$$

where,  $v_{ph}$  is the velocity of the phase. For a group of waves (generally the result for modulated signals), one can consider the group velocity  $v_{gr}$ , which is also related to the velocity of the resultant energy (Hofmann-Wellenhof et al., 2008).

$$v_{gr} = -\frac{df}{d\lambda}\lambda^2. \quad (2.2)$$

The Eq. (2.2) can be used to derive a relationship between the group velocity and the phase velocity as:

$$v_{gr} = v_{ph} - \lambda \frac{dv_{ph}}{d\lambda}. \quad (2.3)$$

It can be observed from the equation that if the phase velocity does not change in the medium (a non-dispersive medium), then the group velocity and phase velocity are equal to each other. In vacuum, the group velocity and the phase velocity are the same, which is speed of light. The velocity of an electromagnetic wave depends on the refractive index  $n$  in a dispersive medium with  $v = \frac{c}{n}$ . This relation can be written for the phase velocity as:

$$v_{ph} = \frac{c}{n_{ph}}. \quad (2.4)$$

And using the relation between the phase and group velocities the relation between the phase and group refractive index can be written as:

$$n_{gr} = n_{ph} - \lambda \frac{dn_{ph}}{d\lambda}. \quad (2.5)$$

The Ionosphere is a dispersive medium for which the phase refractive index  $n_{ph}$  can be written as a series (Hofmann-Wellenhof et al., 2008):

$$n_{ph} = 1 + \frac{c_2}{f^2} + \frac{c_3}{f^3} + \frac{c_4}{f^4} + \dots \quad (2.6)$$

The coefficients  $c_i, i = 2, 3, 4, \dots$  depends on the number of electrons along the propagation path of the signal. Moreover, the term  $\frac{c_2}{f^2}$  have been shown to correspond to the 99.9 % of the ionospheric effect (Hernández-Pajares et al., 2011). Thus the phase refractive index can be simplified into:

$$n_{ph} = 1 + \frac{c_2}{f^2} \quad (2.7)$$

and using the relation between the phase and group refractive index defined in Eq. (2.5), the group refractive index can be written as:

$$n_{gr} = 1 - \frac{c_2}{f^2}. \quad (2.8)$$

These results show that the phase and group velocities have the relation  $v_{ph} > v_{gr}$  since the  $c_2$  term depends on the number of electrons inside the Ionosphere, which is always positive. This results in a delay in modulated signals whereas the phase is advanced. The length of the path of an electromagnetic wave propagating through a medium can be written according to the Fermat's principle of least time as:

$$s = \int nds. \quad (2.9)$$

The integral is a line (actually a column) integral through the ray path. The length  $s$  can be considered as the length of the ray from a GNSS satellite antenna to the receiver antenna. The geometric range  $s_0$  between the satellite and receiver can be written as:

$$s_0 = \int ds_0. \quad (2.10)$$

The delay of electromagnetic wave phase caused by Ionosphere can be written as the difference between the  $s$  and  $s_0$ .

$$I_{ph} = s - s_0 = \int n_{ph} ds - \int ds_0 = \int (1 + \frac{c_2}{f^2}) ds - \int ds_0, \quad (2.11)$$

where,  $I_{ph}$  is the range delay for carrier phases caused by the Ionosphere. A further simplification of the integrals leads to the important relationships of carrier phase delay to the number of electrons inside the Ionosphere by using the estimate  $c_2 = -40.309N_e$  (Hernández-Pajares et al., 2011):

$$\begin{aligned} I_{ph} &= -\frac{40.309}{f^2} \int N_e ds_0, \\ I_{gr} &= \frac{40.309}{f^2} \int N_e ds_0, \end{aligned} \quad (2.12)$$

where,  $N_e$  is the electron density along the ray-path through the Ionosphere. The integral of electron density along the propagation path can be defined as the Slant Total Electron Content (STEC). Note that the observations related to the carrier phases give shorter ranges, whereas observations related to the modulated code on carrier (see group velocity) give longer ranges (Hofmann-Wellenhof et al., 2008). Introducing the STEC to replace the integrals in Eq. (2.12) one can obtain the relation of ionospheric delay and Total Electron Content (TEC) as:

$$\begin{aligned} I_{ph} &= -\frac{40.309}{f^2} STEC, \\ I_{gr} &= \frac{40.309}{f^2} STEC, \end{aligned} \quad (2.13)$$

where STEC is measured in TECU (TEC Units), for which 1 TECU is equal to  $10^{16}$  electrons per  $m^2$ . The relationship in Eq. (2.13) is very important for observing the Ionosphere in terms of GNSS measurements which is described in the Chapter 3.

## 2.2 Observation Methods

As previously mentioned, the effects of Ionosphere on the electromagnetic waves can be regarded as sources of information about the ionosphere.

### 2.2.1 Ionosonde

Reflection is an important effect of the ionosphere that causes certain critical frequencies of electromagnetic waves to be reflected back to the Earth. Ionosonde measurement devices use this principle to measure the height profile for critical frequencies. The electromagnetic waves are transmitted vertically towards the ionosphere and if

they are below a certain energy they are reflected back to the receiver. The receiver then measures the traveling time which is related to the height of the reflection. Since the wave propagation velocity is variable inside the ionosphere, the height is generally called virtual height. The frequency of the wave is incremented to find height profile corresponding to the frequency of the waves. However, this method can only reveal height profiles up to the ionospheric electron density peak, since increasing the frequency further will not result in reflected waves (see Fig. (2.1)) (Prölss, 2004). The plots of height against frequency is called the ionogram, which is used to classify the ionospheric layers up to the peak electron density. A Chapman profile provides a simple model for the vertical distribution of electron density (Hernández-Pajares et al., 2011).

### **2.2.2 Incoherent Scatter Radar**

Ionosondes could not provide information related to the topside of the ionosphere since the electromagnetic waves will not be reflected back after the electron density peak at the F Region. The Incoherent Scatter Radar (ISR), which analyses scattered echoes of incoherent radar pulses from the ionosphere, can be used to obtain useful information not only related to the electron density but also the temperature for ionosphere, upper atmosphere and magnetosphere. The motion of electrons can also be detected by an ISR (Alcaydé, 2001).

### **2.2.3 Satellite Altimetry**

Satellite altimetry is a method of measuring the altitude of a satellite from the Earth's surface by measuring the travel time of microwave signals emitted by the satellite towards to Earth. Satellite altimetry measurements have been widely used in different disciplines from geoid determination to ocean dynamics (Seeber, 2003). Since the measurement principle depends on the propagation of electromagnetic waves, altimeter measurements are also affected by the ionosphere. Thus, dual-frequency altimeter observations can deliver vertical ionospheric electron content measurements. These measurements then can be used as validation tools for ionosphere models, or can be assimilated to obtain more accurate global or regional ionosphere models.

### **2.2.4 GNSS**

Since ionospheric effect depends on the frequency, the dual frequency signals emitted from the GNSS satellites provides invaluable data for monitoring the ionosphere. The geometry-free linear combination of range measurements on different carrier frequencies results in an observation for ionospheric delays eliminating satellite-receiver geometry related errors. This ionospheric observable corresponds to the integral of electron

density along the satellite-receiver signal path (see Eq. 2.13) plus the time delays between the different signals paths in the satellite and receiver electronics which are called Differential Code Biases (DCB) of satellites and receivers. At each epoch a new set of ionospheric observables are acquired which are linked to different satellite-receiver paths. The measurements collected from a network of ground based receivers can be combined to generate regional or global electron content distributions with estimations of receiver and satellite DCBs. Moreover, the GPS receivers mounted on low orbiting satellites provides increased resolution of ionospheric observables with different slant angles. For example COSMIC satellite provides radio occultation measurements of GPS signals which results in horizontal scanning of the atmospheric regions including ionosphere. The electron density inside the ionosphere can be modeled by tomographic reconstruction from all of these measurements including satellite altimetry (Dettmering et al., 2011). A detailed description of using GPS for ionospheric monitoring and modeling is given in Chapters 3 and 4.

## 2.3 Global Ionosphere Models

For dual frequency GPS receivers, the ionospheric effects can be removed by a linear combination of the pseudo-ranges or carrier phases called ionosphere-free linear combination (Hofmann-Wellenhof et al., 2008). However, most of the receivers can only work on single frequency. Moreover, because of anti-spoofing the precise observables on the L1 and L2 frequency are only available to authorized users. Thus, there is a strong need for ionospheric models for single frequency users to correct the ionospheric delay. The ionosphere models are not only required for positioning but also for frequency planing, orbit predictions etc. The ionosphere models currently available are generally empirical. However, physics based models that use data assimilation are also an important research area. The empirical models utilize the collected information about the ionosphere to obtain the key ionospheric parameters. Although there are many ionosphere models developed by different research groups around the world, we focus on the ones listed in the following subsections.

### 2.3.1 Klobuchar Model

The Klobuchar model is an approximation for vertical time delay caused by the ionospheric total electron content. The model parameters are uploaded to the GPS satellites and downloaded by receivers to estimate the vertical ionospheric time delay in seconds, which can reduce the ionospheric effect by 50 % (Hofmann-Wellenhof et al., 2008). The calculated time delay can be converted to slant ionospheric delay in meters via multiplying with speed of light and applying the mapping function in Eq. (3.22). The model is defined as:

$$I_{klo}(t) = A_1 + A_2 \cos\left(\frac{2\pi(t - A_3)}{A_4}\right), \quad (2.14)$$

where,  $I_{klo}(t)$  is the vertical ionospheric delay,  $A_1$  and  $A_3$  are constants with values 5 ns and 14 h local-time respectively and  $t = \frac{\lambda}{15} - t_{UT}$  is the local time of ionospheric pierce point.  $A_2$  and  $A_4$  are calculated from Klobuchar ionosphere parameters as (Hofmann-Wellenhof et al., 2008):

$$\begin{aligned} A_2 &= \alpha_1 + \alpha_2 \varphi_m + \alpha_3 \varphi_m^2 + \alpha_4 \varphi_m^3, \\ A_4 &= \beta_1 + \beta_2 \varphi_m + \beta_3 \varphi_m^2 + \beta_4 \varphi_m^3, \end{aligned} \quad (2.15)$$

where the  $\alpha_i$  and  $\beta_i$  for  $i = 1, 2, 3, 4$  are parameters downloaded in the navigation message,  $\varphi_m$  is the distance between geomagnetic pole denoted by spherical coordinate pair  $(\varphi_P, \lambda_P)$  and the ionospheric pierce point  $(\varphi, \lambda)$  which is introduced in Chapter 4. The distance then can be calculated by:

$$\varphi_m = \arccos(\sin\varphi \sin\varphi_P + \cos\varphi \cos\varphi_P \cos(\lambda - \lambda_P)), \quad (2.16)$$

### 2.3.2 International Reference Ionosphere

The International Reference Ionosphere (IRI) is the standard ionosphere model developed by a working group of the Committee on Space Research (COSPAR) and the International Union of Radio Science (URSI) with approximately 50 international experts. The model has been continuously evolved using the worldwide data from ionosonde stations as well as incoherent scatter radar, rocket measurements and satellite data. It is used as background ionosphere model for many studies about ionospheric electron content. Unlike the Klobuchar model, IRI provides the global electron density profiles. Thus, numerical integration is used to obtain electron content estimates from IRI. As a standard ionosphere model, IRI not only provides the electron density values, but also the ion compositions, temperature and drift. As an empirical model, IRI predictions are better for areas where the measurement density is high. This results in better prediction accuracy on northern mid-latitudes. IRI-2007 model provides an option to select NeQuick model for the topside ionosphere (Bilitza and Reinisch, 2008). The NeQuick model is a 3D time-dependent electron density model developed by The Aeronomy and Radiopropagation Laboratory (ARPL) from Abdus Salam International Centre for Theroretical Physics and The Institute for Geophysics, Astrophysics and Meteorology of the University of Graz. The model is proposed for the ionosphere model for single-frequency users of European Galileo project (Hofmann-Wellenhof et al., 2008).

As of 2009, IRI is an international Standards Organization (ISO) Technical Specification with ISO/TS 16457:2009 reference number. The IRI model is a combination of COSPAR international reference atmosphere, international Telecommunication Union ITU-R model, international reference geomagnetic field and STROM model to obtain different parameters related to different regions of the ionosphere. The model takes R12 (mean sunspot number for 12 months), IG (mean of global ionospheric index for 12 months) and three-hourly magnetic *ap* indices of for last 39 hours. Moreover, real-time updating of the above parameters can lead to real-time ionospheric specifications, which is currently an active research area.

The web-based software for IRI-2007 model can be found on the [http://ccmc.gsfc.nasa.gov/modelweb/models/iri\\_vitmo.php](http://ccmc.gsfc.nasa.gov/modelweb/models/iri_vitmo.php) There is also a software implementation available as FORTRAN source code. The website <http://modelweb.gsfc.nasa.gov/ionos/iri.html> can be used for more information related to IRI.

### 2.3.3 IGS Global Ionosphere Maps

The ionosphere working group of International GNSS Service (IGS) is established in 1998 to provide reliable Vertical Total Electron Content (VTEC) maps generally known as Global Ionosphere Maps (GIMs). The resultant VTEC maps are the weighted combination of VTEC maps generated by independent Ionospheric Associate Analysis Centers (IAAC). The raw GNSS data are obtained from IGS network of more than 350 ground station distributed around the World. The IAACs use mainly the GPS geometry-free linear combination data to extract both VTEC and DCB values. The Center for Orbit Determination in Europe (CODE), which is an IAAC of IGS, also uses GLONAS data for producing VTEC maps. The IAACs are agreed upon a common interface format, which is called the Ionosphere Exchange Format (IONEX), for sharing the resultant VTEC maps. The global VTEC data is dumped as a grid on longitude and latitude with 5x2.5 degrees respectively. The temporal resolution is two hours. The format also handles the estimated DCB values for satellites and receivers.

The quality of VTEC maps produces by IAACs are evaluated by comparing the STEC and DCB values obtained from the maps with the ones observed from the test data. The inverse Root Mean Squared differences are then used as weights for combining VTEC maps to obtain the final product. Due to ground station distribution, GIMs provide better accuracies for the mid-latitudes of the northern hemisphere (Hernández-Pajares et al., 2009).

Unlike IRI, IGS GIMs provide the total electron content of the ionosphere. However, the long time series of IGS GIM products are also an invaluable source of information for updating key parameters in IRI as well as other ionosphere models.

IGS website (<http://igsceb.jpl.nasa.gov/components/prods.html>) provides links

to the rapid and final VTEC maps and other products such as precise orbits, satellite clocks and earth rotation parameters among others. The website for CODE GIMs (<http://aiuws.unibe.ch/ionosphere/>) also gives links to the GIM products and monthly average values for P1-C1 and P1-P1 DCB for the satellites mentioned in previous chapter. More information related to the mathematical functions used for GIMs are given in Chapter 4.

### 2.3.4 Global Assimilation of Ionospheric Measurements

The Global Assimilation of Ionospheric Measurements (GAIM) is derived from assimilation of the ionosphere related data from various sources utilizing physics-based models with a Kalman filter. Unlike the models presented in previous sections, the model utilize Ionospheric Forecast Model (IFM), which provides global electron density distributions from 90 to 1600 km altitude. Then, observations are brought to update some key empirical parameters, which are fed into another physics-based Ionosphere-Plasmasphere Model (IPM) to improve the obtained electron density profile. The generated electron density is then combined with the real-time data collected from different sources via data assimilation techniques based on Kalman filtering. The updated electron density with other parameters are combined to forecast electron density, which is then given to the next step of data assimilation. The result is globally reconstructed continuous electron density in real-time. The algorithm is able to assimilate data from different sources such as digisondes (modern ionosondes), GPS derived STECs, occultation measurements among others (Schunk et al., 2004).

## 2.4 Local and Regional Ionosphere Models

The global ionosphere models mentioned in previous sections use ionospheric measurement from sites distributed around the world. The prediction accuracies depend on the spatial distributions of the sites. The IGS GIMs, for example, deliver better prediction performance over north-hemisphere mid latitudes due to the ground station density (Hernández-Pajares et al., 2011). For regions with rare IGS stations the prediction performance starts to degrade. Moreover, the DCB estimates for the receivers are only available for IGS ground stations. However, many local or regional networks exists in the world that require accurate ionosphere models for both real-time and post-processing needs.

For regional applications, tensor product of univariate B-splines can represent regional spatio-temporal VTEC variations (Schmidt, 2007; Schmidt et al., 2007b) using IRI as a reference ionosphere model. Moreover, other measurements such as satellite altimetry and radio-occultations can also be included to achieve higher dimensional regional models (Dettmering et al., 2011). There are also regional iono-

sphere models which utilize tomographic reconstruction techniques. MIDAS (<http://www.bath.ac.uk/elec-eng/invert/iono/rti.html>) for example provides 2D and 3D ionosphere models for European region. Space Weather Application Centre Ionosphere (SWACI) is another regional ionosphere model where local ionosphere models of second-order polynomials are used for individual stations to estimate the STEC and DCBs in a Kalman filter. The STEC values are then combined to provide regional VTEC maps (Le et al., 2008).

## CHAPTER 3

### THE GLOBAL POSITIONING SYSTEM

The Navigation System with Time and Ranging Global Positioning System (NAVSTAR GPS) or shortly, GPS is a satellite based time transfer, positioning, and navigation system developed by the Department of Defence of USA. The system consists of 24 or higher satellites at an altitude of 20200 km above the Earth, each of which emits specially designed signals towards the Earth. The receivers on Earth or above the Earth decode the signals, and use the information embedded into the signals to obtain the position, velocity and time at anywhere, any time and any weather condition. The system relies on precise timing and orbits of satellites which are broadcast to the receivers. The receivers then use the well-known structure of the signals to acquire and track the satellite signals. The information inside the signal is extracted to obtain the pseudo-ranges from the receiver to individual satellites. At least four pseudo-range measurements are enough for the receiver to estimate the 3D position and clock offset to the GPS time, which is another unknown since the receiver clocks are not synchronized to the GPS time (Seeber, 2003). The segments of the system with the flow of information on each segment are described in the next subsection, with observables related to positioning and Ionosphere monitoring which were explained in the previous Chapter.

#### 3.1 GPS Segments

The GPS has in its full operational capability since 1994. The system mainly contains three segments (Seeber, 2003):

- The Space Segment contains the satellites in their predetermined orbits.
- The Control Segment monitors and controls the health, parameters, orbits and time synchronization of the satellites and upload updated navigation message to them.
- The User Segment consists of various types of receivers using the broadcast signals emitted from the satellites.

### 3.1.1 Space Segment

The Space Segment contains nominally 24 GPS satellites rotating around the Earth in 12 hours with nearly circular orbits. Fig. 3.1 shows the current constellation of the satellites.

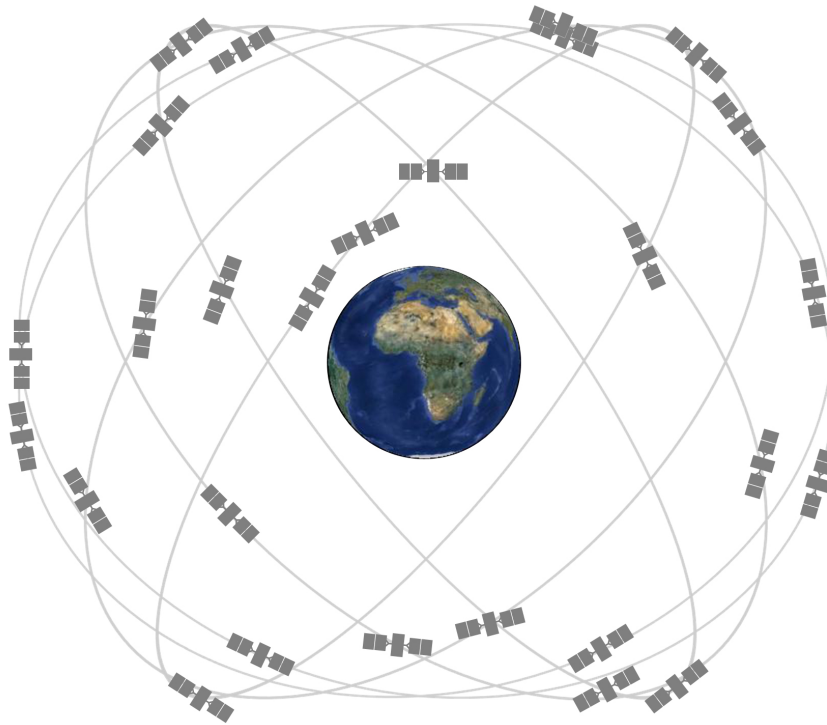


Figure 3.1: The constellation of GPS satellites (gps.gov, 2013)

The orbits of the satellites are arranged so that at least four satellites are in view anywhere at any time on Earth. There are six orbital planes with an inclination of  $55^\circ$ . US Air Force successfully completed an arrangement on the orbits of the current satellites so that constellation reached 27 satellites in June 2011 (gps.gov, 2013). Since GPS continues to evolve and due to the satellite lifetime, different types of satellites are currently active. The currently active satellites and their properties are listed below:

- BLock IIA Satellites: are an enhanced version of Block II satellites. There are 8 Block IIA satellites in the current constellation.
- Block IIR Satellites: are produced to replace the Block II and IIA satellites of which the lifetime is ended. There are 12 Block IIR satellites in the current constellation with on-board clock monitoring.
- Block IIR(M) Satellites : are upgraded version of IIR satellites to complete the current constellation. These satellites provide second civilian signal with two new military signals. There are currently 7 IIR(M) satellites in the constellation.

Other than the ones listed above, there are four Block IIF which provide third civilian signals for transportation safety with extremely precise atomic clocks. The GPS continues to evolve with the upcoming Block III satellites, which will provide fourth civilian signal with a lifetime up to 15 years (gps.gov, 2013).

The satellites in the space segment are responsible to broadcast signals which contain both the ranging codes and the navigation message uploaded by the control segment. The signals are down by a frequency standard of 10.23 MHz provided by the atomic clocks on board. Although there are newly introduced carrier frequencies, we will focus on two signals with carrier frequencies namely L1 and L2. The frequency of the L1 signal is 1575.42 MHz, whereas the L2 frequency is 1227.60 MHz. Each satellite emits modulated ranging codes and messages on both frequencies. The modulation technique is a direct sequence spread spectrum which enables Code Division Multiple Access (CDMA). Thus, even though the satellites emit the signals on the same frequency, individual satellite signals can be separated out by the unique bit sequence assigned to the satellites called Pseudo Random Noise (PRN) (Hofmann-Wellenhof et al., 2008).

The ranging code consists of C/A code and P(Y) code. C/A code is the coarse or acquisition code which is less precise than the P(Y) code. The P code is a ranging code for military purposes which is replaced by the Y code when Anti-Spoofing is on. Anti-Spoofing is a mode of operation where the P code is intentionally changed to an encrypted Y code denying access to unauthorized users. Moreover, there is a mode of operation called Selective Availability (SA), which is an intentional degradation of the accuracy for the C/A code. However, SA was turned-off with an intent not to activate it again in May 2000 (gps.gov, 2013).

### 3.1.2 Control segment

The GPS Control Segment is responsible for tracking the satellites for the purpose of obtaining precise orbits and clocks, then uploading the updated navigation message to the satellites. The control segment is formed of Master Control Station, Monitor Station and Ground Antennas. Fig. 3.2 shows the global distribution of monitor and control stations.

The Master Control Station is responsible for obtaining precise positions of the GPS satellites and precise clock parameters via the information gathered by the monitor stations. The information is then fused into the navigation message and upload to the GPS satellites by ground antennas.

The Monitor stations are responsible for collecting the signals emitted by the satellites with atmospheric data and then submitting the information to the Master Control Station for further processing (gps.gov, 2013).

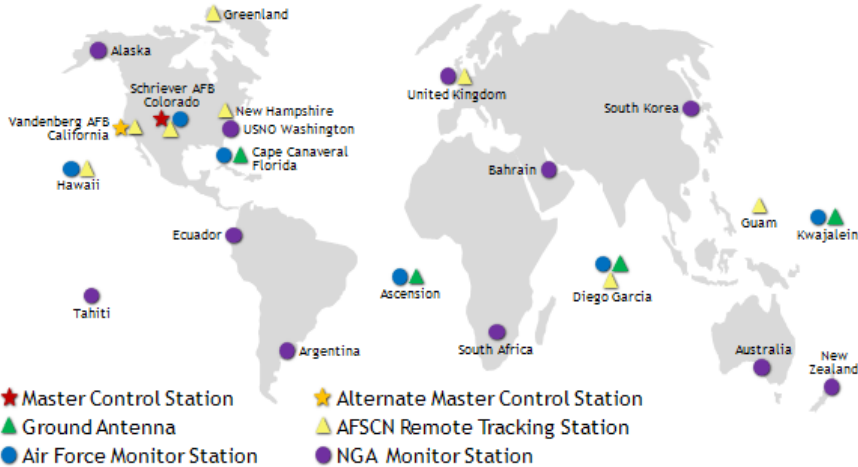


Figure 3.2: The distribution of Master Control Station, monitoring stations and ground antennas(gps.gov, 2013)

### 3.1.3 User Segment

The user segment is composed of a variety of receivers both for civilian and military use. The main responsibility of the receiver is to use the replayed satellite signal inside the receiver to acquire and lock on satellite, decode the ranging codes (pseudo-ranges) and navigation messages to obtain 3D position and velocity information on or over the Earth. A Typical GPS receiver consists of the following parts (Hofmann-Wellenhof et al., 2008):

- Radio Frequency Front-end: consists of the antenna with a low noise amplifier, a reference frequency source and RF section. The antenna provides good signal reception and conversion to the electrical current by amplifying the relatively weak signals. The RF section then uses the reference frequency, which is generally derived from a quartz crystal oscillator to convert the analog signals to digital form.
- Digital Signal Processor: is responsible for signal acquisition, multiplexing the signal into channels, tracking and maintaining the lock on the carrier phases. The trackers maintain locks on the carrier phases and ranging codes by using a replica code generator that generates the ranging codes of the individual satellites. This replica is then correlated with the received signal to maintain the locks. Moreover, it provides information to the navigation processor for decoding the navigation messages and current phase and code measurements.
- Navigation Processor: uses the demodulated signals to decode navigation message and use the information to obtain position and velocity estimations. Moreover, it provides feedback to the tracking loops to aid in maintaining the lock for individual satellite signals.

Since some ranging codes maybe be encrypted (for example Y), different types of mitigation are developed in literature such as cross-correlation, Z-tracking or squaring (Hofmann-Wellenhof et al., 2008). Thus, care must be taken into account for the receiver type since the ranges calculated by them rely on different data processing schemes.

The user segment can be considered to include other voluntary agencies that have their own network of ground stations and provide scientific, educational or other civilian products. The International GNSS Service (IGS) is the well known federation of over 200 agencies around the World that share ground based GNSS data for precise products. There are many Analysis Centers that process the collected information to produce precise orbits and clocks as well as Ionosphere models. Jet Propulsion Laboratory (JPL), Center for Orbit Determination in Europe (CODE), GeoForschungsZentrum, (GFZ) are to name a few among them. Moreover, many national agencies are providing valuable information to the users for correcting their measurements to improve the positioning accuracy.

The receivers in the user segment provide different kind of observables introduced in the following subsection for various positioning, navigation as well as geodetic and scientific research.

## 3.2 GPS Observables

As a one-way ranging system, the basic observable of the GPS is the time of flight of the GPS signal from the satellite antenna to the receiver antenna. This delay is obtained by the receiver via correlating the self generated replica of the ranging codes with the received signals. The time delays related to ranging codes are called pseudo-ranges. There are two kinds of pseudo-ranges; one is related to the less precise C/A ranging code and the other related to the precise P(Y) codes. For the sake of clarity, the pseudo-ranges will be identified as C1 and P1 on L1 carrier frequency, P2 on L2 frequency. Another observable that can be obtained is related to the count of cycles after the carrier phase is locked by the receiver. This observable will be identified by  $\phi_1$  and  $\phi_2$  for L1 and L2 respectively. Although receivers may provide measurements related to Doppler shift or Signal to Noise Ratio (SNR) as well, we will focus on pseudo-ranges and carrier phases in this study. See (Hofmann-Wellenhof et al., 2008) for further information related to the observables.

### 3.2.1 Code Pseudo-ranges

Assume the Earth Centered Earth Fixed (ECEF) position vector of the satellite  $s$  given as  $\mathbf{r}^s(t) = [X^s(t), Y^s(t), Z^s(t)]^T$  at epoch  $t$  and the unknown position vector of a stationary receiver  $r$  as  $\mathbf{r}_r = [X_r, Y_r, Z_r]^T$ . The geometric distance  $\rho_r^s$  from satellite

to the receiver at epoch  $t$  can be written as:

$$\rho_r^s(t) = \sqrt{(X^s(t) - X_r)^2 + (Y^s(t) - Y_r)^2 + (Z^s(t) - Z_r)^2}, \quad (3.1)$$

Then, the basic equation for pseudo-ranges obtained from the ranging codes can be defined as (Hofmann-Wellenhof et al., 2008):

$$P_{r,i}^s = \rho_r^s + c\delta t_{i,r} - c\delta t_i^s + I_{r,i}^s + T_r^s + \epsilon, \quad (3.2)$$

where,  $P_{r,i}$  is observed pseudo-range on carrier frequency  $L_i$  at receiver  $r$  related to satellite  $s$ ,  $\rho_r^s$  is the geometric range from satellite to receiver,  $I_{r,i}^s$  is the ionospheric range delay on frequency  $f_i$ ,  $T_r^s$  is the tropospheric delay, and  $\epsilon$  is the measurement error. Although there are other systematic errors (or biases) that affect the pseudo-ranges such as antenna phase center variation, multipath, orbit errors, we do not introduce them here for the sake of simplicity. The same equation applies to both P1, P2 and C1, however, note that the accuracies are different. The accuracy of the C1 pseudo-ranges are 3 m whereas P1 pseudo-ranges are 0.3 m, which is approximately the 1% of their corresponding chip length. Also note that the coarse range code is only available in L1 frequency, and different receiver types do not provide P1 observable due to different code-less signal processing methods. Thus, whenever possible the P1 code is used instead of C1 code. However, for the receivers without P1 observable, C1 can be used instead.

The use of C1 code instead of P1 code introduces a new bias term into the satellite and receiver clocks since the P1 and C1 code following different processing paths on both receiver and satellite. This bias is called the P1-C1 differential code bias (DCB). Moreover, same kind of bias exists between the P1 and P2 called P1-P2 DCB. These biases must be taken into account when the differencing techniques are used to remove common systematic biases (Hofmann-Wellenhof et al., 2008).

### 3.2.2 Carrier Phases

The basic equation for carrier phase observation is defined as (Hofmann-Wellenhof et al., 2008):

$$\lambda_i \phi_{r,i}^s = \rho_r^s + N_r^s \lambda_i + c\delta t_{i,r} - c\delta t_i^s - I_{r,i}^s + T_r^s + \epsilon, \quad (3.3)$$

where,  $\lambda_i$  is the wavelength of carrier  $L_i$ ,  $N_r^s$  is the number of wavelengths of the geometric range between the satellite and the receiver at the time when the receiver got lock on the carrier  $L_i$ . This term is generally known as the integer ambiguity since

it is related to the number of cycles between the satellite and the receiver initially. Note also that the coefficient of the ionospheric delay  $I_{r,i}$  is negative indicating that the measured ranges are shorter. When the signal tracker inside the receiver loses the lock on a satellite, the lock could be retrieved back. However, an unknown number of cycles would be lost, and the count of cycles will restart. This event is generally called cycle-slip (Hofmann-Wellenhof et al., 2008). Fig. 3.3 shows a simple view of carrier phase observable on the left and the time of a cycle-slip on the right. The processing of carrier phase based pseudo-ranges must consider the cycle-slips as well as integer ambiguities.

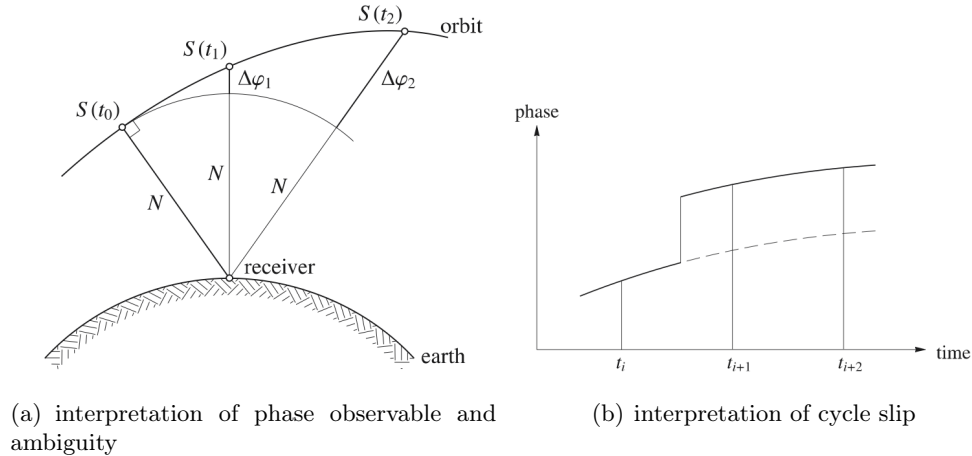


Figure 3.3: Simple interpretation of phase observable and cycle slip (Hofmann-Wellenhof et al., 2008).

There are a number of different techniques for finding and fixing the cycle-slips. For single receiver applications, raw phase measurements or combination of raw phases can be used. Since we use the combination of raw phases and code pseudo-ranges it will be described here. The author is referred to Seeber (2003) or Hofmann-Wellenhof et al. (2008) for further information related to other methods.

### 3.2.3 Cycle-Slip Handling

The combination of code pseudo-ranges defined in Eq. (3.2) and carrier phase observable defined in Eq. (3.3) can be used for detecting the cycle-slips for single receiver applications.

$$\lambda_i \phi_{r,i} - P_{r,i} = \lambda_i N - 2I_{r,i}^s. \quad (3.4)$$

As can be seen from the equation, the terms except the ionospheric delay are eliminated. Since the deviation of the ionospheric observable can be considered small

for close epochs, the deviation in this quantity can be attributed to the variation related to the ambiguity term, which provides an ideal testing quantity for cycle-slips (Hofmann-Wellenhof et al., 2008). When cycle-slips are detected, a new continuous arc is identified and further processing uses this flag in the following steps. Additionally, this flag can be used to level the carrier phases to code pseudo-ranges.

### 3.2.4 Error sources

There are various kind of errors introduced for code pseudo-ranges and carrier phases. Some of the errors among others can be categorized as follows with corresponding error budget:

- Measurement noise on C1 pseudo-ranges: 3 m
- Measurement noise on P1,P2 pseudo-ranges: 0.3 m
- Measurement noise on carrier phases: 5 mm
- The error of satellite orbits: the satellite orbits are estimated by the control segment of GPS and uploaded to the satellites. The error related to orbit is around 2 m. Note that the post-processed orbits published by IGS and other analysis centers can provide orbits with less than 5 cm accuracy.
- The Multipath error: is caused by reception of the satellite signal from different paths generally caused by reflections from nearby features such as buildings or trees. The error related to multipath is about 1-3 m for code pseudo-ranges and about 5 cm for phase observables. The multipath error can be mitigated by proper selection of receiver site location.
- Atmospheric delays: The ionospheric and tropospheric delays are caused by the refraction of the satellite signal propagating through them. The error terms strongly depend on the weather conditions above the receiver as well as the electron content of the ionosphere. This study describes models for correcting the ionosphere related errors, for tropospheric error correction different models have been proposed, a summary of which can be obtained from Hofmann-Wellenhof et al. (2008).
- Relativistic Effects: The GPS satellites are in an accelerated motion relative to the Earth, both the effects of general and special relativity should be considered in observables. The observations are affected by special relativity since the satellite and receiver have a relative motion with respect to each other. Moreover, Since the satellite operates at a different gravitational potential field observations are affected by general relativity (Seeber, 2003).

- **Antenna Phase Center Variations:** The actual measurements of the GPS observables are based on the emission of electromagnetic waves from the satellite antenna and reception at the receiver antenna. However, these points are not fixed and change with frequency, elevation, azimuth and signal intensity, which results in a deviation of phase centers at both satellite and receiver antenna from a reference point (Antenna Reference Point) Hofmann-Wellenhof et al. (2008).
- **The Windup Effect:** The windup effect is related to phase shifts mainly due to change in relative orientation of the receiver and satellite.
- **Earth Tide and Ocean Loading:** Earth tides are related to deformation of the body of Earth in the gravitational influence of Moon and Sun, which could reach up to 60 cm in some places. The ocean tides also cause a deformation on Earth's surface due to varying load which could reach up to 10 cm in some coastal regions (Xu, 2007).
- $\delta t_i^s$ , The clock bias of the satellite: 2m.
- $\delta t_{r,i}$ . The receiver clock bias which is usually treated as an unknown quantity with the receiver position.

Since the code pseudo-ranges have more observation noise than the carrier-phases, they are smoothed by the carrier phases by combining observations belonging to the same satellite arc. The code smoothing algorithm is outlined below.

### 3.2.5 Code Smoothing

The less precise code pseudo-ranges can be smoothed with the carrier phases by the following moving average Hatch process (Hofmann-Wellenhof et al., 2008).

$$\overline{P_{r,i}^s} = \frac{1}{n} P_{r,i}^s + \frac{n-1}{n} (\overline{P_{r,i_{n-1}}^s} + \lambda_i \phi_{r,i_n} - \lambda_i \phi_{r,i_{n-1}}) \quad (3.5)$$

with  $n < N$ ,  $N$  being the maximum window size. The process is valid for continuous satellite arcs where no cycle-slip occurs. If a cycle-slip occurs, the index  $n$  is reset to 1. This method can be used in real-time for single frequency code pseudo-range smoothing with carrier phases.

## 3.3 Point Positioning

The main use of GPS is to find positions of a receiver on or above the Earth. The process of estimating the 3D coordinates of the receiver with respect to a reference frame from the measured ranges to the satellites is called "point positioning". The four

unknowns of receiver coordinates (X,Y,Z) and the receiver clock bias can be estimated if range measurements are available to at least four satellites. As mentioned in the previous sections, the GPS constellation is designed to meet this requirement. The measured ranges are affected by many random and systematic errors, some of which can be mitigated to some degree by correction techniques. There are also combination techniques, which assume that the geometric or systematic biases cancel out when forming linear combination of observables. For example, differencing the pseudo-ranges to the same satellite at the same epoch will result in an elimination of satellite related errors. Similarly, the differencing of observables of different receivers (close enough to each other) will eliminate some receiver related errors as well as frequency and geometry related errors. Receivers with dual frequency measurements can utilize the so called ionosphere-free combination scheme for precise point positioning. Many different combination schemes are available in the literature with varying success and limitations (Hofmann-Wellenhof et al., 2008; Seeber, 2003).

This study is focused on the modeling and use of regional VTEC. Thus, we will consider single receiver applications with single frequency measurements. The following subsections give a short summary of single-frequency point positioning with code pseudo-ranges and carrier-phases as well as precise point positioning with ionosphere-free combinations.

### 3.3.1 Single Frequency Point Positioning

Single frequency point positioning rely on the use of observables coming from one carrier frequency. Generally, the single frequency receivers operate on the C1 pseudo-ranges since this signal is available to the civilian use and is a part of the Standard Positioning Service (SPS). More precise carrier phase observables can also be used in single-frequency point positioning. The point positioning is based on the observed ranges from receiver to the satellites which can be written in simple form as:

$$P_r^s(t) = \sqrt{(X^s(t) - X_r)^2 + (Y^s(t) - Y_r)^2 + (Z^s(t) - Z_r)^2} + c\delta t_r(t) - c\delta t^s(t) + \epsilon(t), \quad (3.6)$$

where,  $\mathbf{r}^s(t) = [X^s(t), Y^s(t), Z^s(t)]^T$  and  $\mathbf{r}_r = [X_r, Y_r, Z_r]^T$  are the position vectors of the satellite  $s$  and receiver  $r$ ,  $P_r^s(t)$  is the measured pseudo-range to the satellite,  $c\delta t^s(t)$  is the range error caused by satellite clock bias,  $\delta t_r(t)$  is the unknown clock error of the receiver,  $c$  is the speed of light and  $\epsilon(t)$  is the measurement noise. The satellite position and clock error can be calculated from the broadcast navigation message or by other means such as precise orbit products from IGS. Thus, the unknowns are related to the receiver position  $\mathbf{r}_r$  and the receiver clock error. In order to solve for four unknowns we need at least four pseudo-range measurements to individual satellites. An estimate for the receiver position can be obtained by a linearization of observation

equation around an approximate receiver position  $\mathbf{r}_0 = [X_0, Y_0, Z_0]^T$ . The resulting linearized observation equation can be written as:

$$\Delta \mathbf{y} = \mathbf{X}|_{\beta=\beta_0} \Delta \boldsymbol{\beta} + \mathbf{e}, \quad (3.7)$$

where, the vector  $\Delta \mathbf{y}$  contains the observed minus modeled pseudo-ranges to individual satellites  $s^k$ ,  $\mathbf{X}|_{\beta=\beta_0}$  is the design matrix which contains the partial derivatives of the observations with respect to the parameters  $\boldsymbol{\beta}$  evaluated at  $\beta_0$  and  $\mathbf{e}$  is the vector of measurement errors. The observation vector can be written as:

$$\Delta \mathbf{y} = \begin{bmatrix} P_r^{s1} - P_{r0}^{s1} \\ P_r^{s2} - P_{r0}^{s2} \\ \vdots \\ P_r^{sk} - P_{r0}^{sk} \end{bmatrix}. \quad (3.8)$$

The contents of design matrix  $\mathbf{X}|_{r=r_0}$  will be given in the next subsections. The parameters  $\Delta \boldsymbol{\beta}$  can be defined as:

$$\Delta \boldsymbol{\beta} = \boldsymbol{\beta} - \beta_0 = \begin{bmatrix} X_r \\ Y_r \\ Z_r \\ \delta t_r \end{bmatrix} - \begin{bmatrix} X_{r0} \\ Y_{r0} \\ Z_{r0} \\ \delta t_{r0} \end{bmatrix}, \quad (3.9)$$

where, the parameter vector  $\boldsymbol{\beta}$  contains both the receiver coordinates and the unknown receiver clock error. With the assumption of a Gauss-Markoff model (introduced in Chapter 4) an estimate for the corrections  $\hat{\Delta \boldsymbol{\beta}}$  can be found by least squares method. Then position and clock error for the receiver can be calculated as:

$$\hat{\boldsymbol{\beta}} = \beta_0 + \hat{\Delta \boldsymbol{\beta}}. \quad (3.10)$$

The following sections describe the contents of the design matrix and parameter vectors for point positioning methods with code pseudo-ranges and carrier-phases.

### 3.3.1.1 Point Positioning with Code Pseudo-ranges

The pseudo-range observable given in Eq. (3.2) can be used to produce the following observation vector:

$$\Delta \mathbf{y} = \begin{bmatrix} P_r^{s1} - \rho_{r0}^{s1} + c\delta t^{s1} - I_{r0}^{s1} - T_{r0}^{s1} \\ P_r^{s2} - \rho_{r0}^{s2} + c\delta t^{s2} - I_{r0}^{s2} - T_{r0}^{s2} \\ \vdots \\ P_r^{sk} - \rho_{r0}^{sk} + c\delta t^{sk} - I_{r0}^{sk} - T_{r0}^{sk} \end{bmatrix}, \quad (3.11)$$

where,  $\rho_{r0}^{si}$ ,  $i = 1, 2, \dots, k$  are the modeled geometric range,  $k$  is the number of satellites in view,  $I_{r0}^{si}$  and  $T_{r0}^{si}$  are the modeled ionospheric and tropospheric range delays,  $c\delta t^{si}$  is the range delay caused by the satellite clock error. The design matrix for the observations can be written as:

$$\mathbf{X}|_{\beta=\beta_0} = \begin{bmatrix} -\frac{X_1-X_{r0}}{\rho_{r0}^1(t)} & -\frac{Y_1-Y_{r0}}{\rho_{r0}^1(t)} & -\frac{Z_1-Z_{r0}}{\rho_{r0}^1(t)} & c \\ -\frac{X_2-X_{r0}}{\rho_{r0}^2(t)} & -\frac{Y_2-Y_{r0}}{\rho_{r0}^2(t)} & -\frac{Z_2-Z_{r0}}{\rho_{r0}^2(t)} & c \\ \vdots & \vdots & \vdots & \vdots \\ -\frac{X_S-X_{r0}}{\rho_{r0}^S(t)} & -\frac{Y_S-Y_{r0}}{\rho_{r0}^S(t)} & -\frac{Z_S-Z_{r0}}{\rho_{r0}^S(t)} & c \end{bmatrix}. \quad (3.12)$$

The parameter vector  $\beta$  is the same given in previous section. The equation system can be solved by least squares method. Satellite elevation dependent observation weighting can be used to find a weighted least squares solution (Hofmann-Wellenhof et al., 2008). The ionospheric and tropospheric delay models are given in the following sections. The carrier smoothed pseudo-ranges  $\bar{P}_r^s$  introduced in previous sections can also be used instead of raw pseudo-ranges  $P_r^s$  for decreasing the measurement noise.

### 3.3.1.2 Point Positioning with Carrier Phases

Although the carrier phase observables are much more precise than the code pseudo-ranges they introduce a new unknown to the system of linear equations, which is generally called the carrier phase ambiguity. The Eq. (3.3) can be used to obtain the following observation vector:

$$\Delta \mathbf{y} = \begin{bmatrix} \lambda\phi_r^{s1} - \rho_{r0}^{s1} + c\delta t^{s1} + I_{r0}^{s1} - T_{r0}^{s1} \\ \lambda\phi_r^{s2} - \rho_{r0}^{s2} + c\delta t^{s2} + I_{r0}^{s2} - T_{r0}^{s2} \\ \vdots \\ \lambda\phi_r^{sk} - \rho_{r0}^{sk} + c\delta t^{sk} + I_{r0}^{sk} - T_{r0}^{sk} \end{bmatrix}. \quad (3.13)$$

Note that that the sign of the ionospheric delay is different from the pseudo-range, which is the result ionospheric effect described in Chapter 2. Since the Eq. (3.3) contains additional unknown quantities related to the carrier-phase ambiguities the parameter vector is enlarged as:

$$\Delta\boldsymbol{\beta} = \boldsymbol{\beta} - \boldsymbol{\beta}_0 = \begin{bmatrix} X_r \\ Y_r \\ Z_r \\ \delta t_r \\ \lambda N_r^1 \\ \lambda N_r^2 \\ \vdots \\ \lambda N_r^k \end{bmatrix} - \begin{bmatrix} X_{r0} \\ Y_{r0} \\ Z_{r0} \\ \delta t_{r0} \\ \lambda N_{r0}^1 \\ \lambda N_{r0}^2 \\ \vdots \\ \lambda N_{r0}^k \end{bmatrix}. \quad (3.14)$$

The ambiguities  $N_r^s$  are integer quantities which are constant while the carrier phase-lock is maintained inside the receiver electronics. Thus, the ambiguities must be carefully handled. Although there are many ambiguity resolution techniques developed in the literature (Hofmann-Wellenhof et al., 2008), we will consider float ambiguities here, because point positioning is only applied for validation and comparison of different ionosphere models in this study. The design matrix for the observations can be written as:

$$\mathbf{X}|_{\beta=\beta_0} = \begin{bmatrix} -\frac{X_1(t)-X_{r0}}{\rho_{r0}^1(t)} & -\frac{Y_1(t)-Y_{r0}}{\rho_{r0}^1(t)} & -\frac{Z_1(t)-Z_{r0}}{\rho_{r0}^1(t)} & c & 1 & 0 & \dots & 0 \\ -\frac{X_2(t)-X_{r0}}{\rho_{r0}^2(t)} & -\frac{Y_2(t)-Y_{r0}}{\rho_{r0}^2(t)} & -\frac{Z_2(t)-Z_{r0}}{\rho_{r0}^2(t)} & c & 0 & 1 & \dots & 0 \\ \vdots & \vdots & \vdots & \vdots & \vdots & \ddots & \ddots & \vdots \\ -\frac{X_S(t)-X_{r0}}{\rho_{r0}^S(t)} & -\frac{Y_S(t)-Y_{r0}}{\rho_{r0}^S(t)} & -\frac{Z_S(t)-Z_{r0}}{\rho_{r0}^S(t)} & c & 0 & \dots & 0 & 1 \end{bmatrix}. \quad (3.15)$$

The number of unknown ambiguities  $N_r^s$  are equal to the number of observation equations (one per satellite), which leads to underdetermined equation system (less number of observations than the unknowns). Thus, more than two epochs must be combined to obtain a solution based on carrier phases. This requires monitoring of the cycle-slips (loss of phase-lock in receiver signal processing) epoch by epoch and introducing a new ambiguity parameter whenever a cycle-slip is detected (Hofmann-Wellenhof et al., 2008). Additionally, observation of code pseudo-ranges and carrier phases can be combined together by introducing appropriate weighting to increase the number of observations (see Eq. (5.6)).

### 3.3.1.3 Applying Atmospheric Corrections

#### Ionospheric Range Delay

Ionosphere is a frequency dependent refractive medium and affects satellite signals depending on the carrier frequency as described in Chapter 2. The ionospheric ranging delay  $I_{r,i}^s(t)$  for frequency  $f_i$  at epoch  $t$  can be written as:

$$I_{r,i}^s(t) = \frac{40.309}{f_i^2} \int_r^s N_e(l,t) dl \approx \frac{40.309}{f_i^2} STEC_r^s(t), \quad (3.16)$$

where,  $f_i$  is the carrier frequency of carrier  $L_i$  for  $i = 1, 2$ ,  $N_e$  is electron density along the ray-path and the integral is a line integral along the ray-path from receiver  $r$  to satellite  $s$  at epoch  $t$ . Assuming a direct path from satellite to receiver the line integral in Eq. (3.16) can be replaced by Slant Total Electron Content (STEC), which is measured in TECU ( $10^{16}$  electrons/ $m^2$ ) (Hofmann-Wellenhof et al., 2008; Schaer, 1999). The ionospheric range delay can be computed if accurate TEC or electron density model is available. Chapter 2 provides some of the mostly used ionosphere models that are used for electron density or STEC modeling. If an electron density model is available, the line integral in Eq. 3.16 can be obtained by numerical integration from approximate receiver position to the satellite. Generally, for receivers on the ground the Vertical Total Electron Content (VTEC) Models are used. The VTEC values at ionospheric pierce points can be transformed to STEC by using an appropriate mapping function which will be defined in Section 3.4. The IGS Global Ionosphere Models (GIM) introduced in Chapter 2 is an example of this kind of models which are provided in the IONEX format. The GIMs include 13 VTEC maps for even hours in a day (from 00:00 to 00:00 the other day). The VTEC maps are frozen snapshots of the VTEC distribution defined on a grid of  $5 \times 2.5$  degrees on longitude and latitude respectively. The temporal and spatial intermediate VTEC values are obtained by interpolation (Schaer et al., 1998). Assume that snapshot VTEC maps are given as  $VTEC_k(\lambda, \varphi) = VTEC(\lambda, \varphi, t_k)$  where  $\lambda$  is the geographic latitude,  $\varphi$  geographic latitude and  $t_k$  is the time in UT. Then, temporal interpolation given below can be used to obtain VTEC values between consecutive snapshot maps.

$$VTEC(\lambda, \varphi, t) = \frac{t_{k+1} - t}{t_{k+1} - t_k} VTEC_k(\lambda, \varphi) + \frac{t - t_k}{t_{k+1} - t_k} VTEC_{k+1}(\lambda, \varphi), \quad (3.17)$$

where,  $t_k \leq t < t_{k+1}$ . One can also use the nearest VTEC map or interpolate between rotated VTEC maps. The spatial interpolation scheme uses bi-linear interpolation of four nearest grid points to obtain VTEC for a point  $(\lambda_0 + p\Delta\lambda, \varphi_0 + q\Delta\varphi)$  where  $\lambda_0$  and  $\varphi_0$  are the lower left grid coordinates,  $0 \leq p < 1$ ,  $0 \leq q < 1$ . The intermediate VTEC value can be obtained by :

$$\begin{aligned} VTEC(\lambda_0 + p\Delta\lambda, \varphi_0 + q\Delta\varphi) &= (1 - p)(1 - q)VTEC(\lambda_0, \varphi_0) \\ &+ p(1 - q)VTEC(\lambda_0 + \Delta\lambda, \varphi) \\ &+ q(1 - p)VTEC(\lambda_0, \varphi_0 + \Delta\varphi) \\ &+ pqVTEC(\lambda_0 + p\Delta\lambda, \varphi_0 + q\Delta\varphi), \end{aligned} \quad (3.18)$$

where,  $\Delta\lambda$  is equal to 5 degrees and  $\Delta\varphi$  is equal to 2.5 degrees for GIMs. The GIMs published by analysis centers such as CODE are post-processed ionosphere

maps. Thus, they can only be used for post-processing. However, parameters for the Klobuchar model defined in Chapter 2 are broadcast to the receivers in the navigation message to obtain real-time ionospheric corrections with degraded accuracy.

### Tropospheric Range Delay

The tropospheric range delay is the delay caused by the neutral atmosphere. Unlike ionospheric effects, the tropospheric effects are independent of the carrier frequency. Thus, the tropospheric effects can not be mitigated by the use of dual-frequency. The range delay can be defined as (Hofmann-Wellenhof et al., 2008):

$$T_r^s(t) = 10^{-6} \int_r^s N^{Trop} ds_0, \quad (3.19)$$

where,  $N^{Trop} = N_{dry} + N_{wet}$  is the total refractivity of the troposphere,  $N_{dry}$  is the dry component and  $N_{wet}$  is the wet component of the refractivity, which is related to the water vapor content. The dry component represents around 90 % of the total refractivity, whereas wet delay is attributed to around 10 %. Hofmann-Wellenhof et al. (2008) gives a summary of various empirical troposphere models. The models use all or combinations of temperature, pressure, partial water pressure, day of year, height and latitude of the observing site to obtain the delay caused by troposphere. Generally, the models give the the zenith path delay which is then converted to the slant delay by an appropriate mapping function. Since the water vapor distribution is hard to model, meteorological measurements are also utilized when available. Another approach to overcome the problem is to introduce the zenith wet delay as an unknown parameter in the least squares estimation process. The coefficients of the zenith wet delay is the mapping function value for each satellite zenith angle.

### 3.3.2 Precise Point Positioning

The Precise Point Positioning (PPP) uses precise orbit and clock products as well as other correction terms to obtain precise position estimations for single receiver applications. Systematic errors such as Earth tides, ocean loading and antenna phase center variations which are introduced in previous sections must all be taken into account. The ionosphere-free linear combination is preferred in PPP since it eliminates frequency dependent ionospheric effects. Although, the ionosphere-free linear combination requires dual-frequency measurements, the single frequency combination of code and phase observables can be also be utilized which leads to single frequency PPP (Hofmann-Wellenhof et al., 2008). The tropospheric delay can be estimated with other parameters as described in the previous section. The precise orbit and clock products can be obtained from IGS through Internet. For single-frequency applications the ionospheric delay can also be modeled by local, regional or global ionosphere

models. Different estimation methods can be applied such as recursive least squares or Kalman filter, where appropriate corrections mentioned above are taken into account.

### 3.4 Extracting TEC from GPS Observables

The electron content inside the ionosphere cause different delays depending on the frequency of the carrier. The difference of code pseudo-ranges on two carrier frequencies results in the so-called geometry-free linear combination of code pseudo-ranges. Satellite-receiver geometry related errors such as geometric range, satellite and receiver clock offset are cancelled out leaving only frequency dependent terms, namely the difference of ionospheric path delays and instrumental biases. The noise level of carrier phase observables is low compared to code pseudo-ranges. Hence, usually the code pseudo-ranges are smoothed with carrier phases and discontinuities in carrier phases are corrected with cycle-slip detection and repair methods (Hofmann-Wellenhof et al., 2008; Schaer, 1999). Then the geometry-free linear combination is derived from the carrier smoothed code observables. This combination removes the satellite receiver geometrical range and all frequency independent biases resulting in the so called ionospheric observable. The combination can be expressed by the following equation (Brunini et al., 2004; Schaer, 1999):

$$\overline{P4_r^s} = \overline{P_{r,1}^s} - \overline{P_{r,2}^s} = (I_{r,1}^s - I_{r,2}^s) + dcb^s + dcb_r + \epsilon_4, \quad (3.20)$$

where,  $\overline{P4_r^s}$  is the geometry-free linear combination,  $\overline{P_{r,1}^s}$  and  $\overline{P_{r,2}^s}$  are carrier phase smoothed pseudo-range observations of to receiver  $r$  and satellite  $s$  for  $L_1$  and  $L_2$  carrier signals,  $I_{r,1}^s$  and  $I_{r,2}^s$  are ionospheric delays on  $L_1$  and  $L_2$ ,  $dcb^s$  and  $dcb_r$  are delays in satellite and receiver hardware when emitting and receiving in different frequencies, generally called differential code biases or inter-frequency biases,  $\epsilon_4$  is the measurement error (Dach et al., 2007).

The STEC in TECU is obtained by inserting Eq. (3.16) into Eq. (3.20) as follows:

$$STEC_r^s = \frac{\left[ (\overline{P_{r,1}^s} - \overline{P_{r,2}^s}) - (dcb^s + dcb_r) \right] f_1^2 f_2^2}{40.309(f_2^2 - f_1^2)}. \quad (3.21)$$

Assuming a spherical Earth model with mean radius  $R$  and a thin spherical shell at a specific height  $H$ , STEC is converted to the height independent VTEC by using a mapping function  $F_r(z')$  :

$$F_r(z') = \frac{STEC_r^s}{VTEC(\lambda, \phi)} = \frac{1}{\cos(z')}, \text{ with} \quad (3.22)$$

$$\sin(z') = \frac{R}{R+H} \sin(z),$$

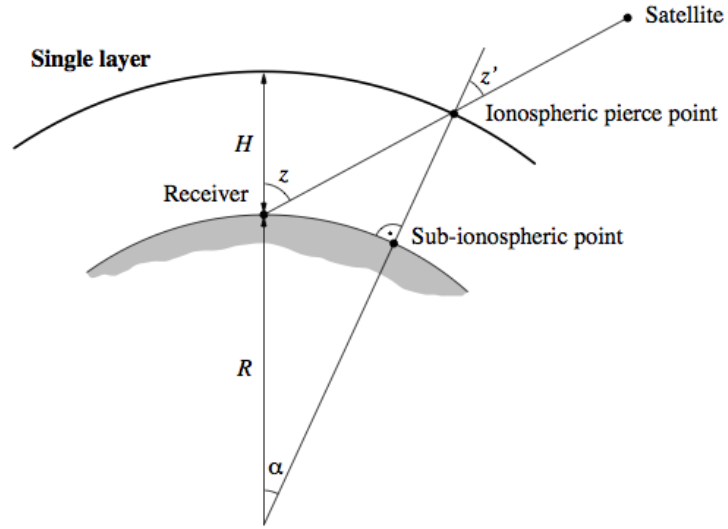


Figure 3.4: Single Layer Ionosphere Model Geometry (Schaer, 1999)

where,  $z$  and  $z'$  are the zenith angles of the satellite at the receiver position and at the ionospheric pierce point  $[\varphi, \lambda]^T$ , with  $\lambda$  and  $\varphi$  as the geographic longitude and latitude respectively (Hofmann-Wellenhof et al., 2008; Misra and Enge, 2003; Schaer, 1999; Seeber, 2003).

The relation of geometry-free linear combination and VTEC at a specific epoch  $t$  can be written as:

$$\overline{P4}_r^s(t) = \alpha F_r(z'_t) VTEC(\lambda, \phi, t) + dcb_r + dcb^s + \epsilon_4, \quad (3.23)$$

where,  $\alpha = 40.309 \frac{f_2^2 - f_1^2}{f_1^2 f_2^2}$  is a constant term,  $\epsilon_4$  is the error in geometry-free linear combination,  $dcb_r$  and  $dcb_s$  are differential code biases in meters. The geometry-free linear combination introduced in this section depends on the carrier-phase smoothed pseudo-range measurements. Chapter 4 gives a modified ionospheric observable which is used in this study as well as a description on how to obtain the IPPs.



## CHAPTER 4

### REGIONAL MODELING OF VTEC

This chapter provides the theoretical background for obtaining non-parametric and semi-parametric regional Vertical Total Electron Content (VTEC) models. The previous chapters gave an overview of the ionosphere, some standard models for the ionosphere, the Global Positioning System (GPS) and extracting VTEC data from GPS observables. The VTEC model mentioned here is *a mathematical function that describes the spatio-temporal representation of the regional VTEC values in order to provide a prediction model for the unknown VTEC over the modeling region*. This kind of prediction models are generally established by fitting a parametrized mathematical function to the observation points via minimizing a Lack of Fit (LOF) criterion. The mostly used LOF criterion is the square of the Euclidean norm which is generally used in the sense of least squares estimation. Different numerical techniques are available for the least squares estimations of the parameters from the observations. If the parameters of the model describes the relationships of the observations to the physical reality, then these parameters can be defined as fixed parameters to be estimated from observations. For VTEC modeling with geometry-free linear observations, satellite and receiver DCBs are examples of parameters which are directly related to physical reality. As previously described, the spatio-temporal variations of the ionosphere is a complicated process although some temporal and spatial variations are known. Thus, if the parameters of the VTEC model cannot describe these variations properly the model not only will not be able to fit to the observations well, but also will provide less accurate predictions. This study introduces non-parametric and semi-parametric VTEC models to overcome this kind of limitations. The non-parametric and semi-parametric models are adaptive and flexible models that are driven from the observations themselves. Thus they also provide empirical models for the VTEC. However, they do not pose a VTEC model with fixed parameters, rather they build the mathematical model out of the observations.

The chapter is organized as follows to be complete and easy to follow. The first section provides reference frames used in VTEC modeling and validation with point positioning followed by a section describing ionospheric observation equation where CODE provided satellite DCBs are eliminated from geometry-free linear combination. The

next section provides some well known parametric VTEC models including the spherical harmonics and regional B-spline based methods as well as estimation of model parameters by least squares. The following section describes the non-parametric VTEC model using Multivariate Adaptive Regression Splines (MARS), proceeded by the non-parametric VTEC model based on Multivariate Adaptive Regression B-Splines. The final section explains the semi-parametric VTEC model, which also estimates the receiver Differential Code Biases (DCBs) as fixed parameters.

## 4.1 Reference Systems and Frames

This section provides a summary of reference systems and reference frames that are used in this study.

International Earth Rotation and Reference Systems Service (IERS) produces an important Terrestrial Reference Frame (TRF) named the International Terrestrial Reference Frame (ITRF) which is a realization of the International Terrestrial Reference System (ITRS). The ITRS is defined with origin at the geocentre, Z axis pointing towards to IERS Reference Pole, and X axis pointing towards the IERS Prime Meridian. Generally coordinates in such a reference frame are called Earth-Centered Earth-Fixed (ECEF) coordinates. The realization uses the position and velocities of observation stations. It is updated according to new measurements and published by IERS with ITRFxx where xx is the year of publication suffix. The latest realizations is the ITRF2008, which can be downloaded from the IERS web site in Solution Independent Exchange (SINEX) format. The 3D Cartesian coordinate system is not appropriate for situations when horizontal and vertical separation of the position is important especially on or above the surface of the Earth. Thus spherical and ellipsoidal coordinates are used to represent positions over the terrestrial reference frames. The following subsection gives a summary of reference systems and frames.

### 4.1.1 The World Geodetic System - WGS84

The World Geodetic System 1984 (WGS84) is the terrestrial reference system of GPS developed since 1960s. It follows the IERS conventions for prime meridian and north pole specification. In 1994, an updated reference frame called WGS84 (G730) by using the IERS published gravitational constant of Earth. Moreover, in 1996 and 2002 a refined parameter set is published leading to WGS84 (G873) and (G1150) (Seeber, 2003). As the number of stations and accuracy is increased, the WGS84 realizations get closer to the ITRS realizations. For the new realizations, the WGS84 is in agreement with the ITRF in centimeter levels, thus can be considered the same. The ellipsoidal coordinates on WGS84 are given in Fig. 4.1. The conversion formulas from the ellipsoidal coordinates  $(\lambda, \varphi, h)$  to 3D Cartesian coordinates  $(x, y, z)$  can be

found in Hofmann-Wellenhof et al. (2008). The reader is referred to NIMA (2000) for detailed information on WGS84 reference frames.

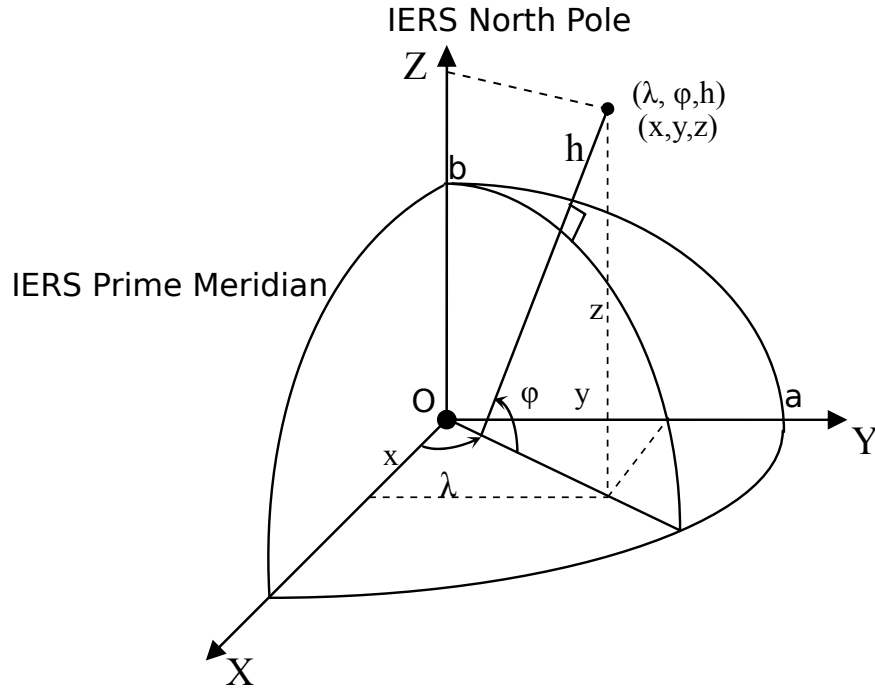


Figure 4.1: The International Terrestrial Reference System and Ellipsoidal Coordinates

#### 4.1.2 Spherical System

The spherical Earth model is defined by the mean radius  $R$  of Earth, which is generally taken as 6371 km. The spherical coordinates and the 3D cartesian coordinates are given in Fig. 4.2. The conversion from spherical coordinates to 3D Cartesian coordinates can be found in (Hofmann-Wellenhof et al., 2008). The spherical model is simple but effective model for representing coordinates on spherical approximation of Earth. It is also important in VTEC modeling since the Single Layer Model introduced in Chapter 3 is based on spherical approximations.

#### 4.1.3 Sun-fixed Reference Frame

The definition of the Sun-fixed reference frame is associated with the mean Sun position. The mean Sun is a fictitious Sun that moves around the equator with constant velocity. Thus the latitudes defined in previous Earth models are not affected by using Sun-fixed reference frame, but the longitude is affected by the following formula (Schaer, 1999):

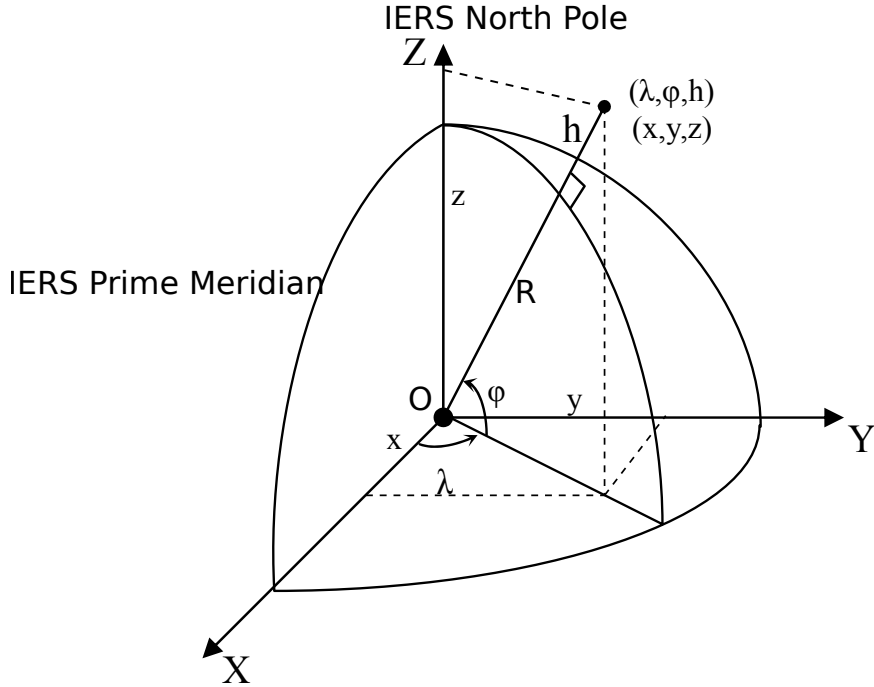


Figure 4.2: The International Terrestrial Reference System and Spherical Coordinates

$$\lambda_{SF} = \lambda - \lambda_0, \quad (4.1)$$

where, the  $\lambda_{SF}$  is the longitude in sun-fixed reference frame,  $\lambda_0$  is the longitude of the mean sun.

#### 4.1.4 Sun-fixed Geomagnetic Reference Frame

The Sun-fixed geomagnetic reference frame is defined by the geomagnetic pole with longitude  $\lambda_P$  and latitude  $\varphi_P$ . The geographic coordinates  $(\lambda, \varphi)$  are then converted to the sun-fixed geomagnetic frame by (Dettmering, 2003):

$$\begin{aligned} \lambda_m &= \lambda_{SF} \\ \varphi_m &= \arcsin(\sin\phi\sin\varphi_P + \cos\varphi\cos\varphi_P\cos(\lambda - \lambda_P)). \end{aligned} \quad (4.2)$$

The global ionosphere maps published by CODE are estimated in sun-fixed geomagnetic reference frame, but final predicted maps are published in Earth-Fixed reference frame in IONEX files.

## 4.2 Observation Equation

The main observable of ionospheric Vertical Total Electron Content (VTEC) is the so called geometry-free linear combination of the Global Positioning System observables in two carrier frequencies. The derivation and relation of the geometry-free linear combination to the VTEC has been introduced in Chapter 2. The geometry-free linear combination formed by carrier phase and pseudo-range measurements from receiver  $r$  to the satellite  $s$  at epoch  $t$  is defined as:

$$\overline{P4_r^s}(t) = \overline{P_{r,1}^s} - \overline{P_{r,2}^s} = \alpha F_r(z'_t) VTEC(\lambda, \varphi, t) + dcb_r + dcb^s + \epsilon_4, \quad (4.3)$$

where,  $\overline{P4_r^s}$  is the geometry-free linear combination calculated from pseudo-range measurements smoothed by carrier phases  $\overline{P_{r,i}^s}$  on two carrier frequencies  $L_i, i = 1, 2$ ,  $t$  is the epoch for which the combination is obtained,  $F_r(z'_t)$  is satellite elevation dependent mapping function defined in Eq. (3.22) with  $z'_t$  being the zenith distance of satellite at the Ionospheric Pierce Point (IPP) defined with geographic longitude  $\lambda$ , geographic latitude  $\varphi$ . The function  $VTEC(\lambda, \varphi, t)$  represents the unknown spatio-temporal distribution of VTEC values depending on geographic longitude  $\lambda$ , geographic latitude  $\varphi$  and time  $t$ . The unknown  $dcb_r$  and  $dcb_s$  are the hardware related differential code biases (DCB) of ranging codes on two carrier frequencies. The term  $\epsilon_4$  is the measurement noise.

Although carrier-smoothed pseudo-ranges are used to obtain  $\overline{P4_r^s}$ , Nohutcu (2009) suggests to perform the smoothing of  $P4_r^s$  directly instead of taking individual carrier-smoothed code observables, which is called carrier to code leveling. Taking the difference of carrier phase observables at two frequencies defined in Eq. (3.3), geometry-free linear combination of carrier-phases can be written as:

$$\phi 4_r^s = \lambda_1 \phi_{r,1}^s - \lambda_2 \phi_{r,2}^s = -\alpha STEC + \lambda_1 N_{r,1}^s - \lambda_2 N_{r,2}^s + ifb_r + ifb^s + \epsilon_4^{ph}, \quad (4.4)$$

where,  $\lambda_i$  is the wavelength of carrier  $L_i$ ,  $ifb_r$  and  $ifb_s$  are the instrumental delays on different frequencies and  $N_{r,i}^s, i = 1, 2$  are the unknown ambiguities on two frequencies. Although the noise level of geometry-free carrier phase observables is relatively low from the pseudo-ranges, using this observable requires solving for the unknown ambiguities. Another approach is to prefer the ionospheric observable of carrier-phases to smooth ionospheric observable of non-smoothed pseudo-ranges  $P4_r^s$  by averaging over continuous satellite receiver arcs (arcs where no cycle-slip occurs). The resulting code leveled ionospheric observable can be written as (Nohutcu, 2009):

$$\overline{P4_r^s}(t) = \overline{(P4_r^s + \phi 4_r^s)} - \phi 4_r^s(t) = \alpha F_r(z'_t) VTEC(\lambda, \varphi, t) + dcb_r + dcb^s + \epsilon_4, \quad (4.5)$$

where,  $\overline{(P4_r^s + \phi 4_r^s)}$  represents the average of the combination over the continuous arc.

This study focuses on estimation of spatio-temporal representation of VTEC and receiver DCBs. The separation of satellite DCB requires additional constraints on the solution since the satellite and receiver DCBs are linearly dependent. Generally a solution is obtained by imposing a zero-mean constraint on satellite DCBs. The satellite DCBs are considered more stable (stable over months). Thus we use satellite DCB eliminated observations in this study where satellite DCB estimations are obtained from CODE.

The satellite DCB eliminated observation  $y_{r,k}$  with respect to receiver  $r$  can be formed from geometry-free linear combination  $\overline{P4_r^s}$  for each epoch  $t_k$  as:

$$\begin{aligned} y_{r,k} &= \frac{1}{\alpha_{F_r(z'_k)}} (\overline{P4_r^s}(t_k) - dcb^s), \\ &= VTEC(\lambda_k, \phi_k, t_k) + \frac{1}{\alpha_{F_r(z'_k)}} dcb_r, \end{aligned} \quad (4.6)$$

where,  $r$  is the receiver number,  $k$  is the observation index,  $t_k$  is the epoch of  $k^{th}$  observation for  $k = 1, 2, 3, \dots, N_r$  with  $N_r$  being the number of observations related to receiver  $r$ . As can be seen from the Eq. (4.6) that all geometry related parameters such as satellite and receiver positions have been eliminated.

The geographic positions of the IPPs  $(\lambda_k, \varphi_k)$  can be obtained if the spherical coordinates  $(\lambda_r, \varphi_r)$  of the receiver, the zenith angle of the satellite at receiver ( $z$ ) and at IPP ( $z'$ ), which can be computed from the ITRF coordinates of the satellite and receiver in a Single Layer Model (see Chapter 3). The satellite coordinates at each epoch are obtained by interpolating precise ephemeris published by IGS. The receiver coordinates can either be estimated via Precise Point Positioning (PPP) techniques or obtained from the published coordinates of the ground network to which the receiver belongs (eg. IGS, EUREF). The geographical coordinates  $(\lambda_{IPP}, \varphi_{IPP})$  of IPPs can be obtained by spherical geometry as (Nohutcu, 2009):

$$\begin{aligned} \varphi_{IPP} &= \arcsin(\sin(\varphi_r)\cos(\Delta z) + \cos(\varphi_r)\sin(\Delta z)\cos(A)) \\ \lambda_{IPP} &= \lambda_r + \arcsin\left(\frac{\sin(A)\sin(\Delta z)}{\cos(\varphi_{IPP})}\right), \end{aligned} \quad (4.7)$$

where,  $\Delta z = z - z'$ . The geometry is shown in Fig 4.3.

For a network of  $R$  ground based GPS receivers, the observations  $y_{r,k}$  can be collected in vectors  $\mathbf{y}_r = [y_{r,1}, y_{r,2}, \dots, y_{r,N_r}]^T$ . Then, the observations from all receivers can be accumulated into the observation vector  $\mathbf{y} = [\mathbf{y}_1^T, \mathbf{y}_2^T, \dots, \mathbf{y}_R^T]^T$  with a total of  $N = \sum_{r=1}^R N_r$  observations. Let  $\mathbf{x}_k = [\lambda_k, \varphi_k, t_k]^T$  be the associated observation location (geographic location of IPP at epoch  $t_k$ ) for observation  $y_k$ , then the values  $\lambda_k, \varphi_k$  and  $t_k$  for  $k = 1, 2, 3, \dots, N$  are called knot-locations of the components  $x_\lambda, x_\varphi$

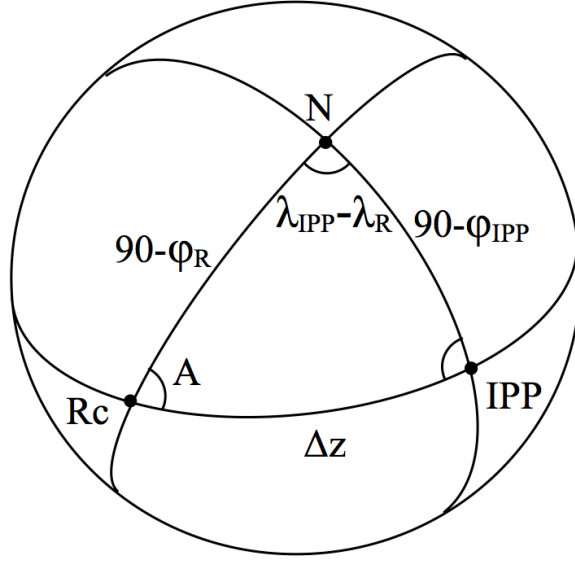


Figure 4.3: The astronomical triangle formed by the North Pole (N), IPP and receiver (Rc) (Nohutcu, 2009)

and  $x_t$  of multivariate variable  $\mathbf{x}$  respectively. The components of  $\mathbf{x}_k$  will be written as  $x_{k,j}$  in the next subsections, where  $j$  represents  $\lambda$ ,  $\varphi$  or  $t$ .

The unknown constants  $dcb_r$  and spatio-temporal function of  $VTEC(\lambda, \varphi, t)$  are then estimated from the observations  $\mathbf{y}$  and knot-locations  $x_{k,j}$ . The next subsections describe parametric, non-parametric and semi-parametric modeling of VTEC and receiver DCBs respectively.

### 4.3 Parametric Modeling of VTEC

Parametric modeling of VTEC is established by introducing a parametrized mathematical model for VTEC. A general parameterized form can be written in terms of a series expansion as:

$$VTEC(\lambda, \varphi, t) = VTEC(\mathbf{x}) = \sum_{i=1}^M a_m h_m(\mathbf{x}), \quad (4.8)$$

where,  $\mathbf{x}$  is the multivariate variable defined in previous sections. It is clear that this kind of model is linear in terms of parameters  $a_m, m = 1, 2, 3, \dots, M$ . The following observation equation can be obtained by substituting this parametric form in Eq. (4.6).

$$\mathbf{y} + \mathbf{e} = \mathbf{Gd} + \mathbf{Ha}, \quad (4.9)$$

where,  $\mathbf{d} = [dcb_1, dcb_2, dcb_3, \dots, dcb_R]^T$  is the parameter vector for the unknown DCBs of receivers, the unknown parameters of VTEC are collected inside the parameter vector  $\mathbf{a} = [a_1, a_2, \dots, a_M]^T$ ,  $\mathbf{G}$  is the coefficient matrix of DCBs,  $\mathbf{H}$  are the coefficients of VTEC parameters and  $\mathbf{e}$  is the measurement error vector. The contents of the  $\mathbf{G}$  matrix can be written as:

$$\mathbf{G} = \begin{bmatrix} \delta_1(\mathbf{x}_1) & \delta_2(\mathbf{x}_1) & \dots & \delta_R(\mathbf{x}_1) \\ \delta_1(\mathbf{x}_2) & \delta_2(\mathbf{x}_2) & \dots & \delta_R(\mathbf{x}_2) \\ \vdots & \vdots & \ddots & \vdots \\ \delta_1(\mathbf{x}_N) & \delta_2(\mathbf{x}_N) & \dots & \delta_R(\mathbf{x}_N) \end{bmatrix}, \quad (4.10)$$

with  $\delta_r(\mathbf{x}_i)$  defined as:

$$\delta_r(\mathbf{x}_i) = \begin{cases} \frac{1}{\alpha F_r(z'_{\mathbf{x}_i})}, & \text{if } \mathbf{x}_i \in \{x_{r,1}, x_{r,2}, \dots, x_{r,N_r}\} \\ 0 & \text{otherwise} \end{cases}, \quad (4.11)$$

where,  $F_r(z'_{\mathbf{x}_i})$  is the mapping function for IPP  $\mathbf{x}_i$ ,  $\alpha$  is the ionospheric constant defined in Chapter 3. As can be observed from the definition, the function  $\delta_r(\mathbf{x}_i)$  is an indicator function that has the value of one over the mapping function multiplied by the  $\alpha$  for IPPs, which are obtained from receiver  $r$ . The coefficient matrix  $\mathbf{H}$  of the VTEC parameters, on the other hand, can be written as:

$$\mathbf{H} = \begin{bmatrix} h_1(\mathbf{x}_1) & h_2(\mathbf{x}_1) & \dots & h_m(\mathbf{x}_1) & \dots & h_M(\mathbf{x}_1) \\ h_1(\mathbf{x}_2) & h_2(\mathbf{x}_2) & \dots & h_m(\mathbf{x}_2) & \dots & h_M(\mathbf{x}_2) \\ \vdots & \vdots & \dots & \vdots & \ddots & \vdots \\ h_1(\mathbf{x}_N) & h_2(\mathbf{x}_N) & \dots & h_m(\mathbf{x}_N) & \dots & h_M(\mathbf{x}_N) \end{bmatrix}, \quad (4.12)$$

where, the function  $h_m(\mathbf{x})$  is a function defined over  $\mathbf{x}$  for the spatio-temporal representation of VTEC. The linear observation equation defined in Eq. 4.9 can be represented in its simple form as:

$$\mathbf{y} + \mathbf{e} = \mathbf{X}\boldsymbol{\beta}, \quad (4.13)$$

where,  $\mathbf{X} = [\mathbf{G} \ \mathbf{H}]$  is the combined designed matrix,  $\boldsymbol{\beta} = \begin{bmatrix} \mathbf{d} \\ \mathbf{a} \end{bmatrix}$  is the stacked parameter vector containing DCBs and VTEC model coefficients. An estimate for the parameters vector  $\boldsymbol{\beta}$  can be obtained using Gauss-Markoff model on the basis of least squares estimation defined below.

## Gauss-Markoff Model

Assume that the expected value of a random vector of measurements  $\mathbf{y}$  and the associated covariance matrix  $D(\mathbf{y})$  be given as:

$$E\{\mathbf{y}\} = \mathbf{X}\boldsymbol{\beta}, \text{ with, } D(\mathbf{y}) = \sigma^2\mathbf{P}^{-1}, \quad (4.14)$$

where,  $u \times 1$  vector  $\boldsymbol{\beta}$  consist of the unknown fixed parameters,  $N \times u$  matrix  $\mathbf{X}$  is the coefficient or design matrix,  $\mathbf{y}$  is  $N \times 1$  random vector of observations,  $\mathbf{P}$  is the positive definite weight matrix and  $\sigma^2$  is the variance of unit weight. Then, for  $N > u$  the consistent system of equations can be defined by introducing an  $N \times 1$  random vector of observation errors  $\mathbf{e}$  as:

$$\mathbf{y} + \mathbf{e} = \mathbf{X}\boldsymbol{\beta}, \text{ with, } E\{\mathbf{e}\} = 0 \text{ and } D(\mathbf{e}) = D(\mathbf{y}) = \sigma^2\mathbf{P}^{-1}, \quad (4.15)$$

where the expected value of observation errors is zero. Gauss-Markoff theorem states that under these assumptions, the least squares estimate  $\hat{\boldsymbol{\beta}}$  of the unknown fixed parameters  $\boldsymbol{\beta}$  is the Best Linear Unbiased Estimator which can be defined with associated covariance matrix as (Koch, 1999):

$$\hat{\boldsymbol{\beta}} = (\mathbf{X}^T\mathbf{P}\mathbf{X})^{-1}\mathbf{X}^T\mathbf{P}\mathbf{y}, \text{ with, } D(\hat{\boldsymbol{\beta}}) = \sigma^2(\mathbf{X}^T\mathbf{P}\mathbf{X})^{-1}. \quad (4.16)$$

For the problems where the observations are uncorrelated and of equal quality the covariance matrix of observations can be written as  $D(\mathbf{y}) = \sigma^2\mathbf{I}$  where  $\sigma^2$  is called the variance factor. The Gauss-Markoff model then simplifies to:

$$\mathbf{y} + \mathbf{e} = \mathbf{X}\boldsymbol{\beta}, \text{ with, } E\{\mathbf{e}\} = 0 \text{ and } D(\mathbf{e}) = D(\mathbf{y}) = \sigma^2\mathbf{I}, \quad (4.17)$$

for which an estimate can be found on the basis of least squares method by:

$$\hat{\boldsymbol{\beta}} = (\mathbf{X}^T\mathbf{X})^{-1}\mathbf{X}^T\mathbf{y}, \text{ with, } D(\hat{\boldsymbol{\beta}}) = \sigma^2(\mathbf{X}^T\mathbf{X})^{-1}. \quad (4.18)$$

In fact, the model given in Eq. (4.15) can be transformed into the simplified model given in Eq. (4.17) by applying a Cholesky factorisation on the positive definite weight matrix  $\mathbf{P}$  and transforming the equation accordingly (Koch, 1999). Generally, apriori knowledge of the variance factor  $\sigma^2$  is not available. An unbiased estimate  $\hat{\sigma}^2$  for the unknown variance factor  $\sigma^2$  can be written as:

$$\hat{\sigma}^2 = \frac{\hat{\mathbf{e}}^T\hat{\mathbf{e}}}{N - u}, \quad (4.19)$$

where,  $N$  is the number of observations,  $u$  is the number of parameters and  $\hat{\mathbf{e}}$  is the residual vector defined as:

$$\hat{\mathbf{e}} = \mathbf{X}\hat{\boldsymbol{\beta}} - \mathbf{y}, \quad (4.20)$$

In this case, the variance-covariance matrix of the estimated parameters  $\hat{\boldsymbol{\beta}}$  can be found by:

$$D(\hat{\boldsymbol{\beta}}) = \hat{\sigma}^2(\mathbf{X}^T \mathbf{X})^{-1}, \quad (4.21)$$

### 4.3.1 VTEC Modeling with Spherical Harmonics

A parametric VTEC model can be obtained by a series expansion in terms of spherical harmonics in a Sun-fixed reference frame by (Schaer, 1999):

$$VTEC(\lambda_{SF}, \varphi_{SF}) = \sum_{n=0}^{n_{max}} \sum_{m=0}^n \bar{P}_{nm}(\sin(\varphi_{SF})) (C_{nm} \cos(m\lambda_{SF}) + S_{nm} \sin(m\lambda_{SF})), \quad (4.22)$$

where,  $\bar{P}_{nm}$  are the normalized Legendre functions of degree  $n$  and order  $m$ ,  $\lambda_{SF}$  and  $\varphi_{SF}$  are the longitude and latitude in sun-fixed reference system,  $n$ ,  $m$  is the degree and order of SH,  $C_{nm}$  and  $S_{nm}$  are the unknown fixed parameters of the ionosphere model. The unknown constants  $dcb_r$  and ionosphere coefficients  $C_{nm}$  and  $S_{nm}$  can be estimated by a Gauss-Markoff model (Dach et al., 2007; Schaer, 1999). The parameter vector  $\mathbf{a}$  for SH modeling is defined as:

$$\mathbf{a}_{SH} = \begin{bmatrix} C_{00} \\ S_{00} \\ C_{01} \\ S_{01} \\ \vdots \\ C_{n_{max}n_{max}} \\ S_{n_{max}n_{max}} \end{bmatrix}. \quad (4.23)$$

The coefficient vector  $\mathbf{H}_{SH}$  which corresponds to  $\mathbf{H}$  in Eq. (4.12) can be obtained by evaluating the spherical harmonic functions at every IPP. Then, the design matrix  $\mathbf{X}$  can be constructed as specified in the previous section by combining coefficient matrices related to DCBs and spherical harmonics and replacing the VTEC parameters  $\mathbf{a}$  in  $\boldsymbol{\beta}$  with SH parameters  $\mathbf{a}_{SH}$  defined above.

### 4.3.2 Regional VTEC Modeling with B-splines

Another frequently used function for regional VTEC is the tensor product of univariate B-splines (Nohutcu, 2009; Schmidt et al., 007b):

$$\begin{aligned}
 VTEC(\lambda, \varphi, t) &= VTEC_{ref}(\lambda, \varphi, t) \\
 &+ \sum_{k_1=1}^{m_{j_1}} \sum_{k_2=1}^{m_{j_2}} \sum_{k_3=1}^{m_{j_3}} a_{k_1, k_2, k_3} \psi_{k_1}^{J_1}(\lambda) \psi_{k_2}^{J_2}(\varphi) \psi_{k_3}^{J_3}(t),
 \end{aligned} \tag{4.24}$$

where,  $VTEC_{ref}(\lambda, \varphi, t)$  is the reference ionosphere model (International Reference Ionosphere-IRI for example),  $a_{k_1, k_2, k_3}$  are the fixed parameters of regional ionosphere,  $\psi_{k_1}^{J_1}$ ,  $\psi_{k_2}^{J_2}$  and  $\psi_{k_3}^{J_3}$  are the univariate normalized quadratic B-spline functions with levels  $J_1$ ,  $J_2$  and  $J_3$  respectively.  $m_{J_1}$ ,  $m_{J_2}$  and  $m_{J_3}$  are the number of univariate B-spline basis functions in corresponding levels. The number of univariate B-spline basis functions is defined as  $m_J = 2^J + 2$ . Thus, for a regional B-spline model of level 3 for latitude, longitude and height a total of 1000 parameters will be required. The unknown parameters and receiver DCBs can be estimated again using Eq. (4.16) by substituting the Eq. (4.24) to Eq. (4.6) and forming the design matrix  $\mathbf{X}$  and  $\boldsymbol{\beta}$  with appropriate values. However, data gaps and the chosen levels for B-spline expansion can result in rank-deficient system of equations. To overcome this problem truncated singular value decomposition or other regularization techniques are used (Nohutcu, 2009; Zeilhofer, 2008).

## 4.4 Non-parametric Modeling of VTEC

Unlike the parametric models defined above, non-parametric modeling does not assume a fixed mathematical form for the spatio-temporal variation of the ionospheric total electron content. Multivariate Adaptive Regression Splines (MARS) and B-splines (BMARS) are adaptive and flexible non-parametric methods for the spatio-temporal representation of VTEC (Durmaz et al., 2010; Durmaz and Karslioglu, 2011).

If the receiver DCBs are also eliminated from  $y_{r,k}$  in Eq. (4.6), then we can obtain observations  $\mathbf{y}^{VTEC}$  containing only VTEC observations.

In the non-parametric modeling,  $VTEC(\lambda, \varphi, t)$  is represented by a function  $f(\mathbf{x})$  defined as:

$$VTEC(\lambda, \varphi, t) = f(\mathbf{x}) = \sum_{m=0}^{M-1} a_m h_m(\mathbf{x}), \tag{4.25}$$

where,  $M$  is the number of basis functions in the model,  $\mathbf{x}$  is the multivariate variable

defined before,  $a_m$  are the coefficients of the associated basis functions  $h_m(\mathbf{x})$ . Then, the observation equation can be written as (Durmaz et al., 2010):

$$\mathbf{y}^{VTEC} = \begin{bmatrix} y_1^{VTEC} \\ y_2^{VTEC} \\ \vdots \\ y_k^{VTEC} \\ \vdots \\ y_N^{VTEC} \end{bmatrix} = \begin{bmatrix} f(\mathbf{x}_1) \\ f(\mathbf{x}_2) \\ \vdots \\ f(\mathbf{x}_k) \\ \vdots \\ f(\mathbf{x}_N) \end{bmatrix} + \begin{bmatrix} e_1 \\ e_2 \\ \vdots \\ e_k \\ \vdots \\ e_N \end{bmatrix}, \quad (4.26)$$

where,  $e_k$  are the observation errors with zero mean and finite variance. The following sections describe how to obtain non-parametric VTEC models with Multivariate Adaptive Regression Splines (MARS) and Multivariate Adaptive Regression B-splines (BMARS).

#### 4.4.1 Non-parametric Modeling with MARS

Multivariate Adaptive Regression Splines (MARS) is an efficient algorithm developed by Friedman (1991). It is also an alternative method for the solution of approximation problems with respect to the multivariate functions. MARS algorithm builds a regression function by automatically generating and fitting basis functions that are directly obtained from the observations.

##### 4.4.1.1 MARS Basis Functions

The MARS basis functions are constructed from truncated power basis functions of the form  $(\pm(x_j - u))_+^q$  where  $x_j$  is the  $j^{th}$  component of a  $p$  dimensional variable  $\mathbf{x}$ ,  $u$  is an observation location associated with variable  $x_j$ ,  $q$  is the order of spline approximation and the “+” sign indicates the positive part of the function (Friedman, 1991). For the case of VTEC models in an Earth-Fixed reference frame,  $p = 3$  and  $\mathbf{x} = [\lambda, \varphi, t]^T$  as defined in previous sections. The reader is referred to Friedman (1991) for more detailed information related to MARS algorithm. The general form of  $i^{th}$  MARS basis function can be represented by

$$h_i(\mathbf{x}) = \prod_{d=1}^{D_i} [s_{di}(x_{v(d,i)} - u_{di})]^q, \quad (4.27)$$

where,  $D_i$  is the degree of the  $i^{th}$  basis function,  $v(d, i)$  represents the associated component of the multidimensional variable  $\mathbf{x}$  with corresponding knot location  $u_{di}$ ,

$q$  is the order of the splines. If  $q = 1$  the basis functions are called reflected pairs and take the following simple form:

$$\begin{aligned}
L_u^j(\mathbf{x})_+ &= (x_j - u)_+ = \begin{cases} x_j - u & \text{if } x_j > u \\ 0 & \text{otherwise} \end{cases} \\
L_u^j(\mathbf{x})_- &= (u - x_j)_+ = \begin{cases} u - x_j & \text{if } x_j \leq u \\ 0 & \text{otherwise} \end{cases}
\end{aligned} \tag{4.28}$$

with  $u \in \{x_{1,j}, x_{2,j}, \dots, x_{N,j}\}$   
and  $j = \lambda, \varphi, t$ ,

where,  $x_j$  is the  $j^{\text{th}}$  component of the input space,  $N$  is the number of observations. The  $k^{\text{th}}$  observation  $y_k$  is observed at location  $\mathbf{x}_k = [\lambda_k, \varphi_k, t_k]^T$  with  $k = 1, 2, 3, \dots, N$  and  $u$  is a univariate knot location from the set  $\{x_{k,j}\}$ . Since the basis functions are directly obtained from the observation locations and the knots are not predetermined the resulting model becomes adaptive. This property makes it useful for regional applications.

The basis functions in Eq. (4.28) are piecewise linear splines, which do not have continuous derivatives. In order to create basis functions that possess continuous derivatives truncated cubic functions defined in Eq. (4.29) are introduced (Friedman, 1991).

$$\begin{aligned}
C_u^j(\mathbf{x})_+ &= \begin{cases} 0 & x_j \leq u_-, \\ c_{s_+, r_+, u_-}(x_j) & u_- < x_j < u_+, \\ (x_j - u) & x_j \geq u_+ \end{cases} \\
C_u^j(\mathbf{x})_- &= \begin{cases} (u - x_j) & x_j \leq u_- \\ c_{s_-, r_-, u_+}(x_j) & u_- < x_j < u_+, \\ 0 & x_j \geq u_+ \end{cases}
\end{aligned} \tag{4.29}$$

with  $u, u_-, u_+ \in \{x_{1,j}, x_{2,j}, \dots, x_{N,j}\}$ ,

$u_- < u < u_+$

and  $j = \lambda, \varphi, t$ ,

where,  $c_{s_+, r_+, u_-}(x_j)$  and  $c_{s_-, r_-, u_+}(x_j)$  are defined as

$$\begin{aligned}
c_{s_+, r_+, u_-}(x_j) &= s_+(x_j - u_-)^2 + r_+(x_j - u_-)^3 \\
c_{s_-, r_-, u_+}(x_j) &= s_-(x_j - u_+)^2 + r_-(x_j - u_+)^3
\end{aligned} \tag{4.30}$$

with

$$\begin{aligned}
s_+ &= (2u_+ + u_- - 3u)/(u_+ - u_-)^2 \\
r_+ &= (2u - u_+ - u_-)/(u_+ - u_-)^3 \\
s_- &= (3u - 2u_- - u_+)/(u_- - u_+)^2 \\
r_- &= (u_- + u_+ - 2u)/(u_- - u_+)^3.
\end{aligned} \tag{4.31}$$

The cubic reflected pairs are defined with three consecutive observation locations  $(u_-, u, u_+)$  where  $u$  is the location. The reflected cubic pairs are cubic inside open

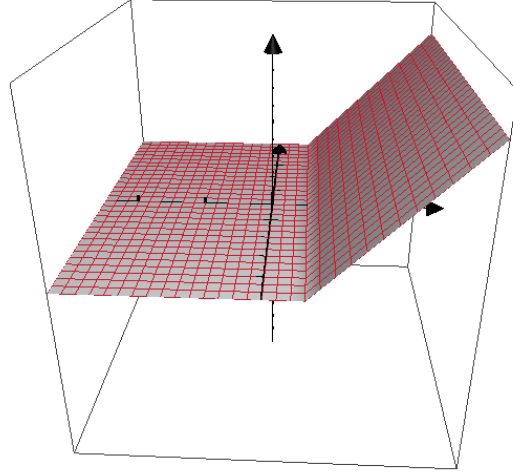


Figure 4.4: The basis function  $L_1^\lambda(\mathbf{x})_+$  obtained by the observation locations  $u = 1$  on the  $\lambda$  axis.

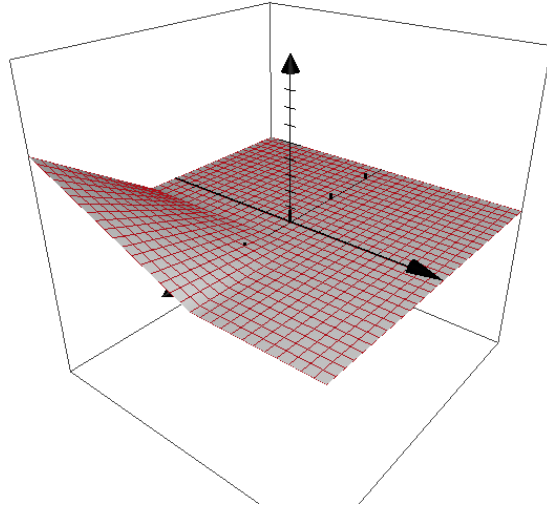
interval  $(u_-, u_+)$ . The definitions in Eq. (4.30) and (4.31) ensure that both  $C_t^j(\mathbf{x})_+$  and  $C_t^j(\mathbf{x})_-$  have continuous first derivatives. Both piecewise-linear and cubic reflected pairs are defined over the entire multidimensional space. For example,  $\mathbf{x}$  can be given as  $\mathbf{x} = [\lambda, \varphi]^T$  and Figure 4.4 shows the basis function  $L_1^\lambda(\mathbf{x})_+$  assuming that one has observation at  $[1, \varphi_k]^T$ . Figure 4.5 on the other hand shows how the interaction (product) of basis functions takes the form of tensor product splines by using another reflected pair  $L_1^\varphi(\mathbf{x})_-$  and  $L_1^\varphi(\mathbf{x})_+$  obtained from set of observation location  $[\lambda_k, 1]^T$ . Fig. 4.6, on the other hand, shows the typical reflected cubic pairs.

#### 4.4.1.2 MARS Algorithm

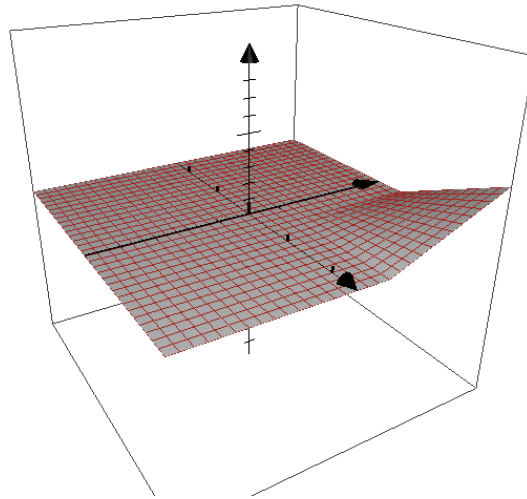
MARS algorithm constitutes a regression function (model) of the form

$$f(\mathbf{x}) = \sum_{m=0}^{M-1} a_m h_m(\mathbf{x}), \quad (4.32)$$

where,  $\mathbf{x} = [\lambda, \varphi, t]^T$  is vector of predictor variables,  $a_m h_m(\mathbf{x})$  are the terms in the model, which are automatically selected by the algorithm, with  $h_m(\mathbf{x})$  being the MARS

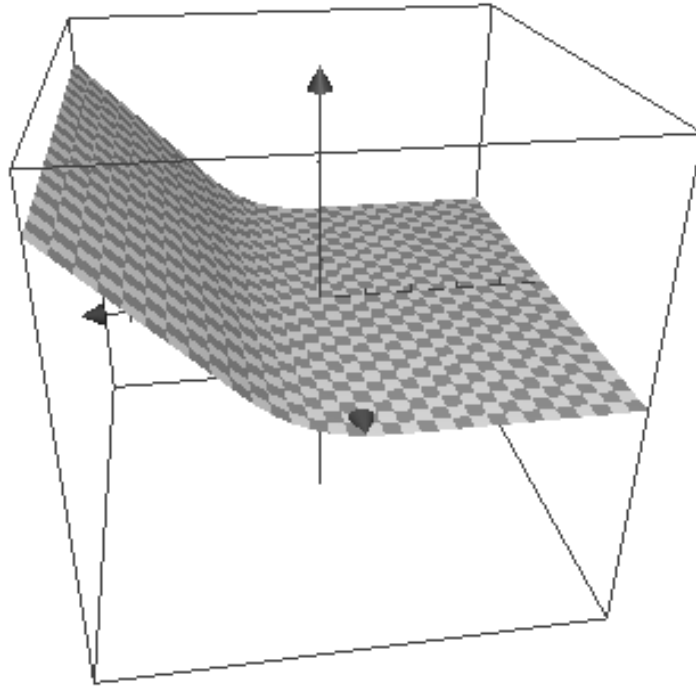


(a) The tensor product spline  $L_1^\lambda(\mathbf{x})_+ L_1^\varphi(\mathbf{x})_-$

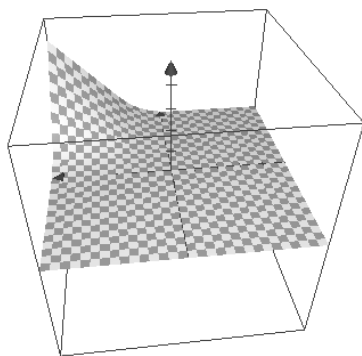


(b) The tensor product spline  $L_1^\lambda(\mathbf{x})_+ L_1^\varphi(\mathbf{x})_+$

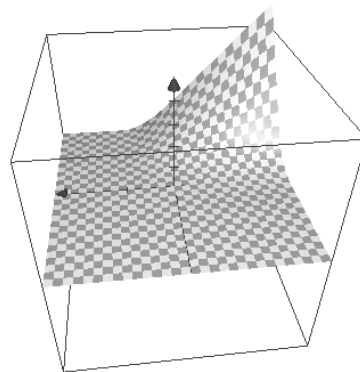
Figure 4.5: The product of basis function  $L_1^\lambda(\mathbf{x})_+$  by the reflected pair  $(L_1^\varphi(\mathbf{x})_-, L_1^\varphi(\mathbf{x})_+)$  defined by the observation location  $u = 1$  on the  $\varphi$  axis forming higher order basis functions.



(a)



(b)



(c)

Figure 4.6: The product of basis function  $C_1^\lambda(\mathbf{x})_+$  ( defined by knots  $(-1, 1, 2)$  on the  $\lambda$  axis (a) ), with the reflected cubic pair  $(C_1^\varphi(\mathbf{x})_-$  (b),  $C_1^\varphi(\mathbf{x})_+$  (c) defined by the observation locations  $(-1, 1, 2)$  on the  $\varphi$  axis forming higher order basis functions.

basis functions defined in Eq. (4.27). The observation equation is given by:

$$\mathbf{y}^{VTEC} = \begin{bmatrix} y_1^{VTEC} \\ y_2^{VTEC} \\ \vdots \\ y_k^{VTEC} \\ \vdots \\ y_N^{VTEC} \end{bmatrix} = \begin{bmatrix} f(\mathbf{x}_1) \\ f(\mathbf{x}_2) \\ \vdots \\ f(\mathbf{x}_k) \\ \vdots \\ f(\mathbf{x}_N) \end{bmatrix} + \begin{bmatrix} e_1 \\ e_2 \\ \vdots \\ e_k \\ \vdots \\ e_N \end{bmatrix}, \quad (4.33)$$

where,  $\mathbf{y}$  is the vector of VTEC observations with the corresponding observation locations  $\mathbf{x}_k = [\lambda_k, \varphi_k, t_k]^T$ ,  $k = 1, 2, \dots, N$ ,  $\mathbf{e} = [e_1, e_2, \dots, e_N]^T$  is the vector of observation error with zero mean and finite variance. In Eq. (4.32),  $h_0(\mathbf{x}) = 1$ ,  $a_0$  is the intercept and  $h_m(\mathbf{x})$ ,  $i > 0$  are the basis functions generated by the products of functions (explained in detail in the forward stage below) from the set

$$C = \{L_u^j(\mathbf{x})_+, L_u^j(\mathbf{x})_-\}, \quad (4.34)$$

$$u \in \{x_{1,j}, x_{2,j}, \dots, x_{N,j}\}, j = 1, 2, \dots, p,$$

including the constant function  $h_0(\mathbf{x}) = 1$ . In the case of cubic modeling, the functions in the set are replaced by cubic reflected pairs  $(C_u^j(\mathbf{x})_+, C_u^j(\mathbf{x})_-)$ . The pair of functions  $\{L_u^j(\mathbf{x})_+, L_u^j(\mathbf{x})_-\}$  is formed by knot locations  $u = x_{k,j}$  as shown in Eq. (4.29). The reflected pairs are defined over the entire space and the fitting procedure estimates their coefficients one by one in pairs. Such an approach avoids the necessity of gridding the input space. The purpose of the algorithm as a non-parametric regression procedure is to estimate a regression function  $\hat{f}(\mathbf{x})$  in Eq. (4.33), unlike the linear regression where the model parameters with their covariance are estimated. MARS works by selecting best parameters associated to the best basis functions built from the set  $C$  in Eq. (4.34) in the forward stage and remove the least significant ones in the backward stage utilizing the GCV to control model complexity and overfitting. The definition of GCV is given in Eq. (4.35).

## MARS Forward Stage

The Algorithm 1 outlines the steps of forward stepwise fitting of a MARS model.

The forward stage starts by adding the basis function  $h_0(\mathbf{x}) = 1$  to the model as given in Line 2 of Algorithm 1. Then, until model contains  $M$  basis functions or a stopping condition is reached, a new pair of basis functions are searched and added to the model. The stopping condition in Line 4 can be a user defined threshold on the improvement of residual sum of squares. In Line 13, a new pair of basis functions  $h_{i+1}(\mathbf{x}) = h_m(\mathbf{x})L_u^j(\mathbf{x})_+$  and  $h_{i+1}(\mathbf{x}) = h_m(\mathbf{x})L_u^j(\mathbf{x})_-$  are iteratively added to the model, where  $\{L_u^j(\mathbf{x})_-, L_u^j(\mathbf{x})_+\}$  is a reflected pair from the set  $C$  in Eq. (4.34) and

---

**Algorithm 1** MARS Forward Stage

---

```
1: ▷ Initialize with the intercept term
2:  $i = 1, h_0(\mathbf{x}) \leftarrow 1, f(\mathbf{x}) \leftarrow a_0 h_0(\mathbf{x})$ 
3: ▷ Loop until maximum number of basis functions has been reached or other
   stopping criteria has been observed
4: while  $i < M$  or  $stopConditionReached(i)$  do
5:    $lof^* \leftarrow \text{inf}$ 
6:   ▷ For all basis functions already in model
7:   for  $m = 0$  to  $i - 1$  do
8:     ▷ For all variables that are not shared by the  $m^{th}$  basis function
9:     for all  $j \notin \{v(d, m) \mid 1 < d < D_m\}$  do
10:      ▷ For all knot locations  $u$  defined for variable  $x_j$ 
11:      for all  $u \in \{x_{k,j} \mid h_m(\mathbf{x}_k) > 0\}$  do
12:        ▷ Form reflected pairs
13:
14:         
$$f(\mathbf{x}) \leftarrow \sum_{i=0}^i a_i h_i(\mathbf{x}) + a_{i+1} h_m(\mathbf{x}) [(x_j - u)]_+$$

15:
16:         
$$+ a_{i+2} h_m(\mathbf{x}) [-(x_j - u)]_+$$

17:
18:        ▷ Test for the improvement on the lack of fit
19:         $lof \leftarrow LOF(f)$ 
20:        if  $lof < lof^*$  then
21:          ▷ Select the current lack of fit, variable, basis function
22:          and knot location as the best fit.
23:
24:           $lof^* \leftarrow lof, m^* \leftarrow m, j^* \leftarrow j, u^* \leftarrow u$ 
25:        end if
26:      end for
27:    end for
28:  end for
29:  ▷ Add the selected reflected pairs to the model in increase model size
30:   $h_i(\mathbf{x}) \leftarrow h_m(\mathbf{x}) [(x_{j^*} - u^*)]_+$ 
31:   $h_{i+1}(\mathbf{x}) \leftarrow h_m(\mathbf{x}) [-(x_{j^*} - u^*)]_+$ 
32:   $i = i + 2$ 
33: end while
```

---

$h_m(\mathbf{x})$  is a basis function already in the model ( $0 \leq m < i$ ) including the constant function  $h_0(\mathbf{x})$ . The selection of the pair  $\{h_i(\mathbf{x}), h_{i+1}(\mathbf{x})\}$  is performed by searching the products of basis functions  $h_m(\mathbf{x})$  from the model and the reflected pairs from the set  $C$  such that,  $h_m(\mathbf{x})$  and the reflected pairs do not share the same variable  $x_j$  and when added to the model, they give maximum decrease on the residual sum of squares (LOF) in Lines 12 to 18 (Friedman, 1991). The products of basis functions tend to form higher degree terms as defined in Eq. (4.27) and the algorithm allows only the products with degree less than or equal to the user defined degree of the final model. Figure 4.5 is also an example of second degree terms, which are built by multiplying different basis functions. The figure can be interpreted in the context of model building as assuming  $\mathbf{x} = [\lambda, \varphi]^T$  and  $h_m(\mathbf{x}) = L_1^\lambda(\mathbf{x})_+$  then  $h_i(\mathbf{x}) = h_m(\mathbf{x})L_1^\varphi(\mathbf{x})_-$  is on the left of the figure and  $h_{i+1}(\mathbf{x}) = h_m(\mathbf{x})L_1^\varphi(\mathbf{x})_+$  is on the right of the figure. The nested loops in Algorithm 1 requires least squares solution to be obtained for each candidate reflected pair during the search for a best fitting pair. However, Friedman (1991) provides an updating formula for consecutive knot locations  $u$ , which makes the innermost loop executed very rapidly.

### MARS Backward Stage

The Algorithm 2 outlines the MARS backward elimination stage. The model searches for subsets of the basis functions  $\{h_0(\mathbf{x}), h_1(\mathbf{x}), \dots, h_{M-1}(\mathbf{x})\}$  that gives the minimum Lack Of Fit criterion based on Generalized Cross Validation (GCV). In order to obtain the GCV value, the coefficients  $a_m, m = 0, 1, \dots, M - 1$  are estimated by the least squares method described in previous sections. In Line 2 to 5 the LOF of the full model is obtained by estimating the coefficients by least squares. The loop in Line 7 ensures that at every iteration one basis function is removed while the inner loop at line 10 finds the optimum one to be removed. The if statement at line 19 keeps track of the best subset that gives the minimum GCV score. The output is the optimal model  $\hat{f}^*(\mathbf{x})$  that has the best GCV score.

The backward stage prunes the large model produced in the forward stage by removing the terms, which make least contributions to the residuals, such that the final model is not an over-fit model and has a good prediction performance. This iterative procedure is continued until an optimal effective number of terms are present in the final model leading to a regularization like procedure by utilizing GCV. GCV defines a trade-off between the goodness of fit and the model complexity. It is used to optimally estimate the effective terms  $\hat{a}_i h_i(\mathbf{x})$  to be present in the final estimated regression function  $\hat{f}(\mathbf{x})$  (Friedman, 1991). The GCV is defined as:

$$LOF(f) = GCV(f) = \frac{\sum_{k=1}^N \left[ y_k - \sum_{m=0}^{M-1} \hat{\beta}_m h_m(\mathbf{x}_k) \right]^2}{(1 - K(f)/N)^2}, \quad (4.35)$$

---

**Algorithm 2** MARS Backward Stage

---

```
1: ▷ Begin with all the basis functions obtained by the forward stage
2:  $F^* \leftarrow \{h_0(\mathbf{x}), h_1(\mathbf{x}), \dots, h_{M-1}(\mathbf{x})\}, K^* \leftarrow F^*$ 
3:  $g^* \leftarrow \sum_{h_n \in F^*} a_n h_n(\mathbf{x})$ 
4: ▷ Obtain the GCV for the whole model
5:  $lof^* \leftarrow LOF(g)$ 
6: ▷ For all basis functions
7: for  $i = M - 1$  to 1 do
8:   ▷ Obtain a new subset by removing the basis function that gives
     a decrease on GCV
9:    $lof_i \leftarrow \infty, G \leftarrow K^*$ 
10:  for  $m = 1$  to  $i$  do
11:    ▷ Remove the basis function  $h_m(\mathbf{x})$  from the current subset
12:     $K \leftarrow L - \{h_m(\mathbf{x})\}$ 
13:     $g^* \leftarrow \sum_{h_n \in K} a_n h_n(\mathbf{x})$ 
14:     $lof^* \leftarrow LOF(g)$ 
15:    if  $lof < lof_i$  then
16:       $lof \leftarrow lof_i, K^* \leftarrow K$ 
17:    end if
18:    ▷ If the GCV improves select this subset as best subset
19:    if  $lof < lof^*$  then
20:       $lof^* \leftarrow lof, F^* \leftarrow K$ 
21:    end if
22:  end for
23: end for
24: ▷ Obtain the best model  $f^*(\mathbf{x})$  by estimating the coefficients  $a_m$ 
25:  $\hat{f}^*(\mathbf{x}) = LOF(\sum_{h_m \in F^*} a_m h_m(\mathbf{x}))$ 
```

---

where,  $K(f)$  is a measure of effective number of terms in the model defined as  $K(f) = r + cL$ , where  $r$  is linearly independent basis functions in the model,  $L$  is the number of knot locations which are selected when building the model in forward stage and  $c$  is a constant value indicating a cost for selecting knots. Less knots will be selected for larger values of  $c$ . Thus, the resulting model will be smoother. In this study  $c$  is taken to be equal to 3 as recommended in (Hastie et al., 2001). The model which gives the minimum GCV value is selected as the best model from the algorithm. MARS can handle a very large data set of observations even though the regression in each step of the forward stage seems to have a big computation cost, since the regression at each step is simplified by an updating formula (Hastie et al., 2001). Another advantage of MARS is that it gives an adaptive and flexible model since the basis functions are automatically selected from the observations and the model complexity can be controlled by the user via adjustment of the maximal number of the terms and the maximal degree of the final model (Hastie et al., 2001).

#### 4.4.2 Non-Parametric Modeling with BMARS

MARS algorithm described in the previous section uses truncated power series as the building blocks for its basis functions. BMARS, on the other hand, uses compactly supported univariate B-splines for forming basis functions. BMARS algorithm differs not only from MARS in terms of the choice of basis functions, but also in terms of forming them. It differs especially in the forward stage by the scale by scale forming and selection of basis functions. B-splines are defined over a non-decreasing knot-sequence which also defines the support of the B-splines. BMARS algorithm starts with the largest scale in which it constructs basis functions that have large support and can represent large scale features in the observations. The scale is then decreased when necessary to decrease the support of basis functions in order to also represent small scale features. In this regard, BMARS algorithm uses a scale by scale approach to model building producing a best model in terms of GCV score. The following subsections describe the basis functions, forward and backward stages of the algorithm.

##### 4.4.2.1 BMARS Basis Functions

Given a list of non-decreasing knot-locations  $[\dots, u_{n-1}, u_n, u_{n+1}, u_{n+2}, \dots]$  corresponding to the variable  $x_j$ , where  $j$  is the component of the multivariate variable  $\mathbf{x}$  introduced before, univariate B-splines of order  $d = 0$  are given as

$$B_{0,u_n}(x_j) = \begin{cases} 1 & \text{if } x_j \text{ in } [u_n, u_{n+1}) \\ 0 & \text{otherwise.} \end{cases} \quad (4.36)$$

For  $d \geq 1$ , B-splines can be defined recursively as

$$B_{d,u_n}(x_j) = \frac{x_j - u_n}{u_{n+d} - u_n} B_{d-1,u_n}(x_j) + \frac{u_{n+d+1} - x_j}{u_{n+d+1} - u_{n+1}} B_{d-1,u_{n+1}}(x_j) \quad (4.37)$$

having support of  $[u_n, u_{n+d+1})$  and  $B_{d,n}(x_j) > 0$  for  $x_j \in (u_n, u_{n+d+1})$  (Iske et al., 2002). To obtain endpoint interpolating B-splines one can repeat the endpoints  $u_1$  and  $u_N$   $d + 1$  times having  $u_{-d+1}, \dots, u_0 = u_1$ ,  $u_N = u_{N+1}, u_{N+2}, \dots, u_{N+d}$  with  $n = -d + 1, -d + 2, \dots, 1, \dots, N - 1$ .

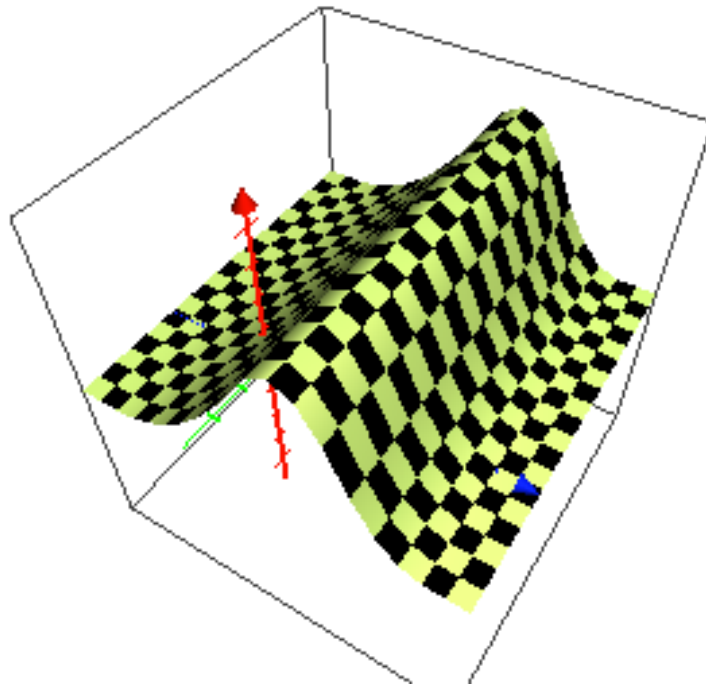
Fig. 4.7 presents cubic B-splines defined over known locations  $[-1, 1, 2, 3]$  on  $\lambda$  and  $[-1, 1, 2, 3]$  on  $\varphi$ . Observe that B-spline functions are compactly supported and smoother than the MARS basis functions given before. Fig. 4.8 on the other hand shows uniform B-splines for different levels.

BMARS algorithm generates the B-splines defined above from special sets of sorted knot locations  $C_l^j$  where  $l$  is the B-spline level and  $j$  is the component index of multivariate variable  $\mathbf{x}$ . For every variable  $x_j$  the knot locations are sorted in ascending order,  $x_{k,j} < x_{k+1,j}$ ,  $n = 1, 2, \dots, N-1$  where  $N$  is the number of observations. Then, set  $C_l^j$  is defined as

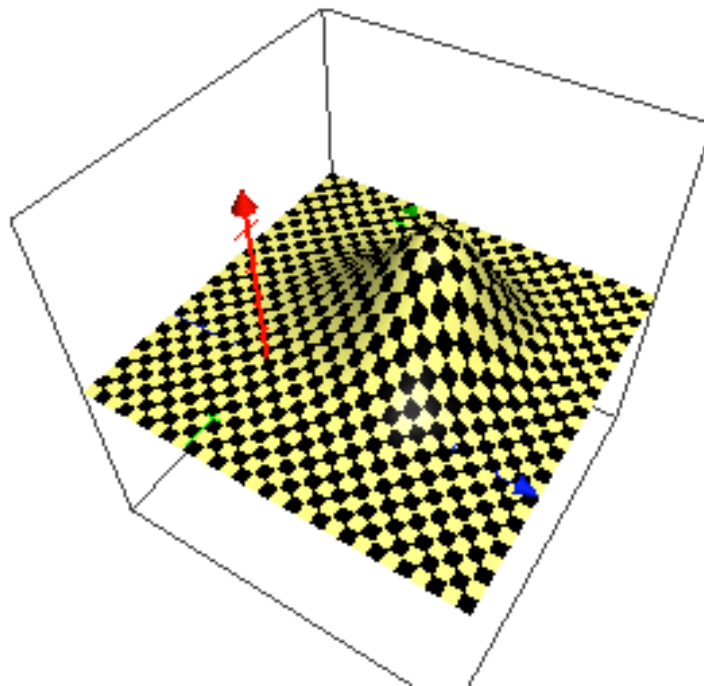
$$C_l^j = \{x_{1,j}, u_{l,s,j}, x_{N,j}\}, \quad s = 1, 2, \dots, 2^l - 1, \quad (4.38)$$

$$u_{l,s,j} = x_{[s2^{-l}N+0.5],j},$$

where, the rounded integers  $[s2^{-l}N + 0.5]$ , correspond to the rank of  $s \times 2^{-l} \times 100$  percentile of the sorted knot locations  $x_{k,j}$  (Bakin et al., 1997). For example, for level  $l = 1$  the set  $C_1^j$  can be defined as  $\{x_{1,j}, x_{[N/2+0.5],j}, x_{N,j}\}$ . Similarly, for  $l = 2$ ,  $C_2^j = \{x_{1,j}, x_{[N/4+0.5],j}, x_{[2N/4+0.5],j}, x_{[3N/4+0.5],j}, x_{N,j}\}$ . The support of B-splines decreases as the level  $l$  increases, which results in more localized functions. A set of B-splines can be generated for every set  $C_l^j$  for constructing the basis functions of BMARS. One important consequence of this procedure is that each support interval of individual B-splines will contain equal number of observations to support the estimation of their coefficients. The B-splines in Fig. 4.8 presents the quadratic B-splines with increased level. Note that the support of each function decreases as the level is increased leading to more compact supports. However, the B-splines given in Fig. 4.8 are generated by equally spaced knots. For most practical problems the data distribution is not even, especially for IPPs. Thus, if such a uniform grid is constructed (which is the case for parametric regional B-spline based modeling given in previous chapters) then, some of the B-spline basis functions will not have any observations located on their support interval leading to a rank deficient system of equations. However, this is not the case for BMARS since the percentile based approach adapts to the data distribution. The adaptation of the BMARS basis functions are presented in Fig. 4.9 and Fig. 4.10. The data given in the figures are generated randomly with a uniform distribution function on  $y$  axis, whereas a Chi Square distribution on the  $x$  axis. Note that the univariate B-spline basis generated for the  $y$  axis is similar to the B-spline



(a) BMARS basis function formed by knots  $(-1,1,2,3)$  over  $\lambda$



(b) BMARS basis function formed by product of basis function defined over  $\lambda$  and B-Spline formed by knot locations  $(-1,1,2,3)$  over  $\varphi$

Figure 4.7: Sample BMARS basis functions

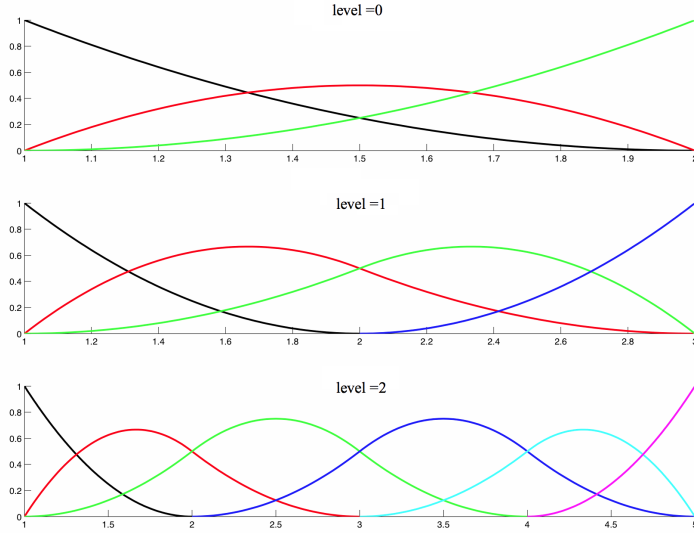


Figure 4.8: Uniform B-splines with different levels

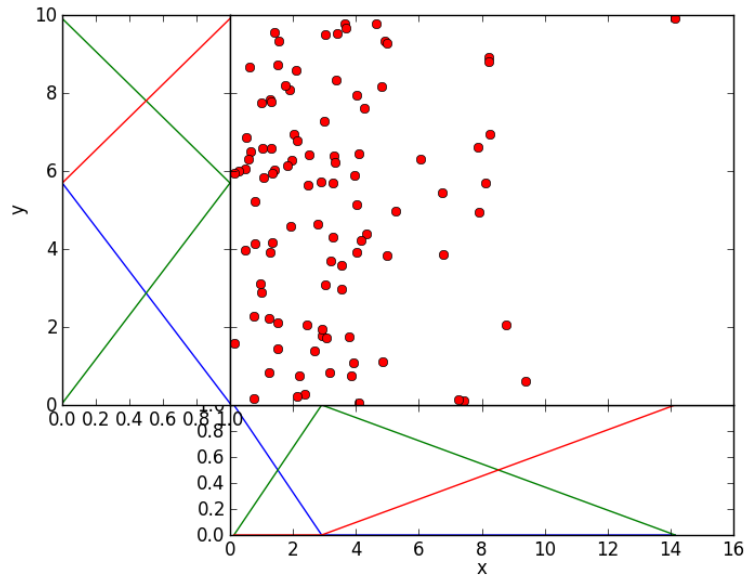
basis functions defined over uniform knot-locations. The B-splines defined over  $x$  axis are stretched to the right of the figure since the percentiles are concentrated on the left of the  $x$  axis where data is dense. Another consequence which can be observed from the figures is that the supports of the B-splines at the same level can be varying, although they are equal in terms of percentiles. Fig. 4.11, on the other hand, presents the behaviour of the BMARS algorithm for evenly spaced data.

#### 4.4.2.2 BMARS Algorithm

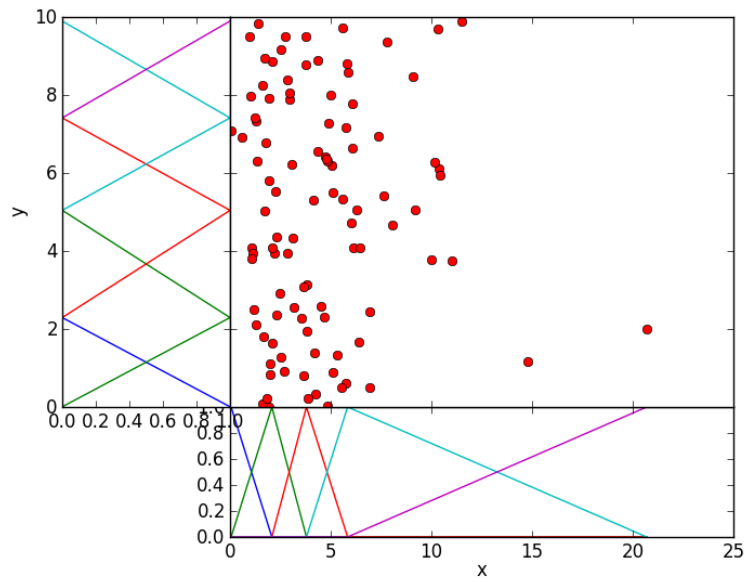
The general form of a BMARS basis function  $h_m(\mathbf{x})$  can be defined as (Bakin et al., 2000):

$$\begin{aligned}
 h_m(\mathbf{x}) &= h_i(\mathbf{x})B_{d,u_{l,m}}(x_{v(m)}) & m &= 1, 2, 3, \dots, M-1 \\
 & & i &= 0, 1, 2, \dots, m-1,
 \end{aligned} \tag{4.39}$$

where,  $h_m(\mathbf{x})$  is the  $m^{\text{th}}$  basis function,  $h_i(\mathbf{x})$  is the  $i^{\text{th}}$  basis function already in the model, and  $B_{d,u_{l,m}}(x_{v(m)})$  is the univariate B-spline with degree  $d$ . The  $u_{l,m}$  represent the knots that define the B-spline, which are chosen from the sorted knot sets  $C_v^l$ . The basis function  $h_m(\mathbf{x})$  are the products of univariate B-splines with different scales and variables. The variable  $v(m)$  is chosen such that it is not used before in  $h_i(\mathbf{x})$ . BMARS builds the function in Eq. (4.25) in forward and backward stages applying Gram-Schmidt orthonormalization described in the following subsections.

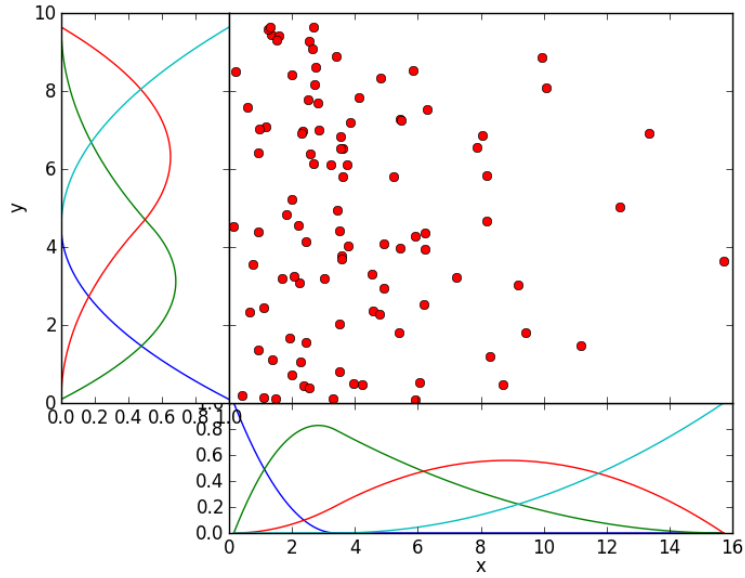


(a) Order 1 B-splines for level 1

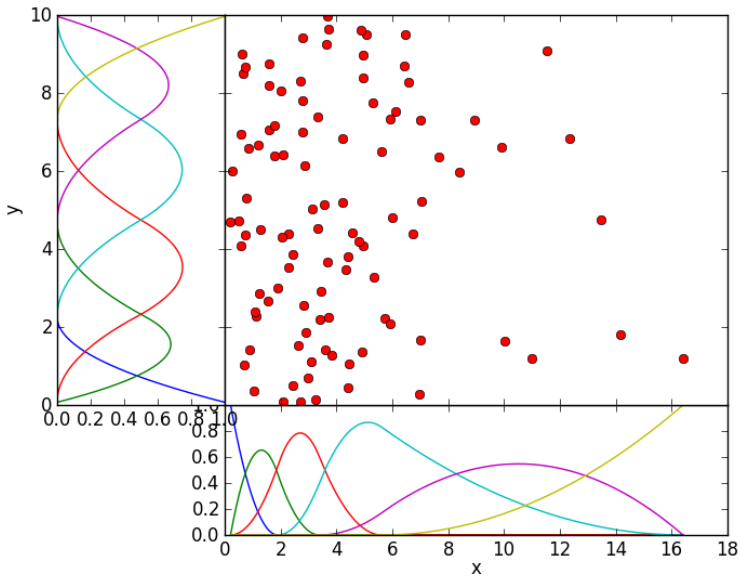


(b) Order 1 B-splines for level 2

Figure 4.9: BMARS basis functions with B-splines of order 1 for levels 1 and 2 defined over non-uniform data sampling

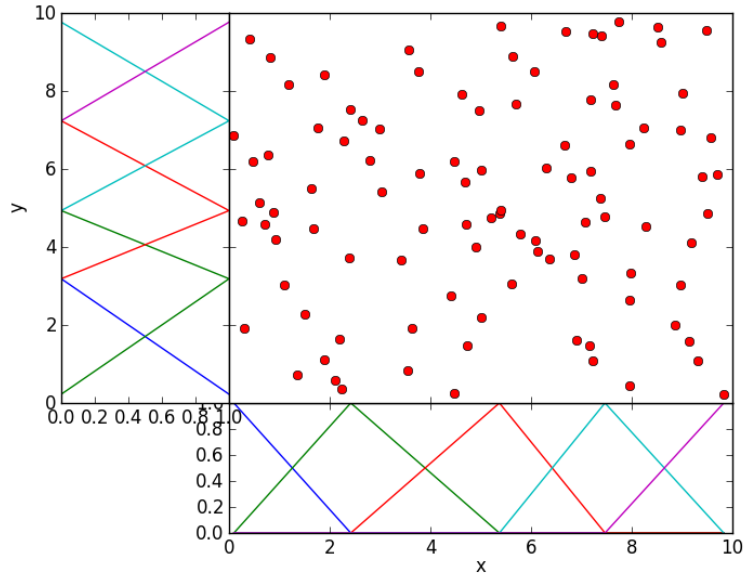


(a) Order 2 B-splines for level 1

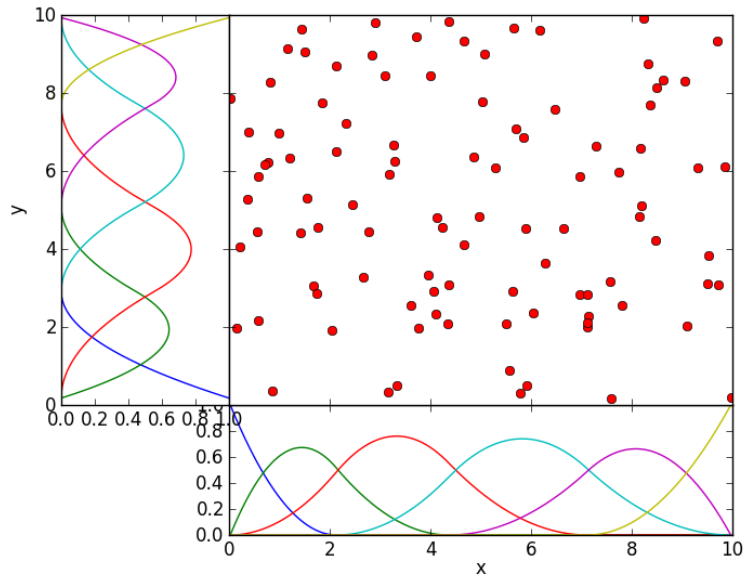


(b) Order 2 B-splines for level 2

Figure 4.10: BMARS basis functions with B-splines of order 2 for levels 1 and 2 defined over non-uniform data sampling



(a) Order 1 B-splines for level 2



(b) Order 2 B-splines for level 2

Figure 4.11: BMARS basis functions with B-splines of order 1 and 2 for levels 2 over uniform data sampling

## BMARS Forward Stage

The forward stage adds new basis functions  $h_m(\mathbf{x})$  into the model starting with  $m = 0$ . At each step  $m$ , the basis function that reduces the Residual Sum of Squares (RSS) is added to the model. Thus, the following systems of equations should be solved for each candidate basis function  $h_m(\mathbf{x})$  with least squares at each step.

$$\mathbf{y}^{VTEC} = [\mathbf{h}_0, \mathbf{h}_1, \dots, \mathbf{h}_i, \dots, \mathbf{h}_{m-1}, \mathbf{h}_m] \begin{bmatrix} a_0 \\ a_1 \\ \vdots \\ a_{m-1} \\ a_m \end{bmatrix} + \mathbf{e}_m, \quad (4.40)$$

where, the column vectors  $\mathbf{h}_i = [h_i(\mathbf{x}_1), h_i(\mathbf{x}_2), \dots, h_i(\mathbf{x}_N)]^T$  are related to coefficient  $a_i$ ,  $i = 0, 1, 2, \dots, m$ ,  $\mathbf{e}_m$  is the error vector at step  $m$ .

The Algorithm 3 gives an outline for the BMARS algorithm. The general structure of the algorithm is similar to the MARS forward stage given in Algorithm 1. However, It differs in Line 11 for basis function forming and knot selection, in Line 13 obtaining the residual sum of squares for the new basis function, and in line 24-31 for increasing the scale when enough large scale components are added to the model. This kind of model building leads to a scale by scale model building strategy. Moreover, since the sets  $C_l^j$  contain much less knot locations for small levels, less candidate basis functions are searched with respect to the MARS algorithm. However, note that there is an updating algorithm for MARS for piecewise reflected pairs. Another important difference is that, BMARS uses a modified Gram-Schmidt orthonormalization process to find the best fitting  $h_m^*(\mathbf{x})$  by orthonormalizing the candidate with the basis functions already orthonormalized in the model. In this case, the  $RSS_m$  of the model at  $m^{th}$  step for each candidate basis function  $h_m(\mathbf{x})$  (Line 15) can be written as (Bakin et al., 2000):

$$RSS_m = RSS_{m-1} - \frac{\left[ \mathbf{h}_m^T \mathbf{y}^{VTEC} - \sum_{i=0}^{m-1} \mathbf{h}_m^T \hat{\mathbf{h}}_i \hat{\mathbf{h}}_i^T \mathbf{y}^{VTEC} \right]^2}{\mathbf{h}_m^T \mathbf{h}_m - \sum_{i=0}^{m-1} \left[ \mathbf{h}_m^T \hat{\mathbf{h}}_i \right]^2}, \quad (4.41)$$

where,  $\hat{\mathbf{h}}_i$  are the orthonormalized column vectors of Eq. (4.40). Eq. (4.41) can be interpreted as a compact form for the contribution of basis function  $h_m(\mathbf{x})$  to the RSS. The best fitting basis function  $h_m^*(\mathbf{x})$  is selected by minimizing the function  $h_m^*(\mathbf{x}) = \operatorname{argmin}_{h_m(\mathbf{x})} RSS_m$ . It is then orthonormalized with the existing ones and added to the model as  $h_m(\mathbf{x})$ . The iteration continues until all the  $M$  basis functions are included into the model, or a predefined threshold for the decrease in RSS is reached. At each step, the Generalized Cross Validation of the current model is monitored. If it tends to increase then, the level of the B-splines is increased. This results in a decrease in

---

**Algorithm 3** BMARS Forward Stage

---

```
1: ▷ Initialize with the intercept term and level to 1
2:  $i = 1, l \leftarrow 1, h_0(\mathbf{x}) \leftarrow 1, f(\mathbf{x}) \leftarrow a_0 h_0(\mathbf{x})$ 
3: ▷ Loop until maximum number of basis functions has been reached or other
   stopping criteria has been observed
4: while  $i < M$  or  $stopConditionReached(i)$  do
5:    $lof^* \leftarrow \inf$ 
6:   ▷ For all basis functions already in model
7:   for  $m = 0$  to  $i - 1$  do
8:     ▷ For all variables that are not shared by the  $m^{th}$  basis function
9:     for all  $j \notin \{v(m)\}$  do
10:      ▷ For all knot locations  $u$  defined for variable  $x_j$ 
11:      for all  $u \in C_l^j \mid h_m(\mathbf{x}_k) > 0$  do
12:        ▷ Form candidate term
13:         $f(\mathbf{x}) \leftarrow \sum_{i=0}^i a_i h_i(\mathbf{x}) + a_{i+1} h_m(\mathbf{x}) B_{o,u}(\mathbf{x})$ 
14:        ▷ Test for the improvement on the lack of fit
15:         $lof \leftarrow RSS(f)$ 
16:        if  $lof < lof^*$  then
17:          ▷ Select the current lack of fit, variable, basis function and knot
            location as the best fit.
18:           $lof^* \leftarrow lof, m^* \leftarrow m, j^* \leftarrow j, u^* \leftarrow u$ 
19:        end if
20:      end for
21:    end for
22:  end for
23:  ▷ Add the selected reflected pairs to the model in increase model size
24:   $gcv_i \leftarrow GCV(f)$ 
25:   $h_i(\mathbf{x}) \leftarrow h_m(\mathbf{x}) B_{o,u^*}(\mathbf{x})$ 
26:   $i = i + 1$ 
27:   $gcv_{i+1} \leftarrow GCV(f)$ 
28:  if  $gcv_{i+1} > gcv_i$  then
29:    ▷ Increase the level since adding more basis function in this scale
      will not contribute to the prediction error
30:     $l \leftarrow l + 1$ 
31:  end if
32: end while
```

---

the support of B-spline basis function to be searched leading to an enlargement of the search space. The next step then searches for smaller scale features to be included into the model.

### BMARS Backward Stage

The backward stage of BMARS is identical to the MARS backward stage where less significant basis functions are iteratively removed from the model and a best model in terms of GCV score is generated. The orthonormalized column-vectors and associated RSS values can be reused to optimize the backward stage. The GCV is defined as (Friedman, 1991).

$$GCV(f) = \frac{\frac{1}{N} \sum_{k=1}^N \left[ y_k - \sum_{i=0}^{M-1} \hat{a}_i h_i(\mathbf{x}_k) \right]^2}{(1 - K(f)/N)^2}, \quad (4.42)$$

where,  $f$  is the tuning variable,  $K(f)$  is related to the effective number of terms in the model. The GCV score is an analytic approximation to the prediction error (Hastie et al., 2001). Thus, the model with minimum GCV score is considered as the one with best prediction performance.

## 4.5 Semi-Parametric Modeling of VTEC

The non-parametric models introduced in the preceding sections assume that apriori estimates of receiver DCBs are available. They are assumed to be provided or estimated by other means. This section describes a semi-parametric approach based on BMARS where receiver DCBs and VTEC can be estimated together. The semi-parametric model is defined as:

$$f(\mathbf{x}) = \sum_{r=1}^R dcb_r g_r(\mathbf{x}) + \sum_{m=0}^{M-1} a_m h_m(\mathbf{x})$$

with

$$g_r(\mathbf{x}) = \begin{cases} \frac{1}{\alpha F_r(z'_\mathbf{x})}, & \text{if } \mathbf{x} \text{ is related to receiver } r \\ 0 & \text{otherwise} \end{cases}, \quad (4.43)$$

where,  $\alpha$  and  $F_r(z'_\mathbf{x})$  are the constant and mapping function given in Section 4.2,  $dcb_r$  is the unknown DCB of receiver  $r$ ,  $R$  is the number of receivers in the network. The semi-parametric model has the advantage of estimating the receiver DCBs as well as the advantage of building an adaptive and flexible spatio-temporal VTEC representation. The model can be built by utilizing the forward and backward stages given in the

previous subsection. The observation equation (Eq. 4.40) can be re-written for semi-parametric model as:

$$\mathbf{y} = [\mathbf{g}_1, \dots, \mathbf{g}_R, \mathbf{h}_0, \mathbf{h}_1, \dots, \mathbf{h}_{m-1}, \mathbf{h}_m] \begin{bmatrix} dcb_1 \\ \vdots \\ dcb_R \\ a_0 \\ a_1 \\ \vdots \\ a_{m-1} \\ a_m \end{bmatrix} + \mathbf{e}_m, \quad (4.44)$$

where,  $\mathbf{g}_r = [g_r(\mathbf{x}_1), g_r(\mathbf{x}_2), \dots, g_r(\mathbf{x}_N)]^T$  are the column vectors for the parameters  $dcb_r$  in Eq. (4.43) with  $r = 1, 2, 3, \dots, R$ ,  $\mathbf{h}_i$ , which are defined in Eq. (4.40), are column vectors related to parameters  $a_i$  in Eq. (4.43) with  $i = 0, 1, 2, \dots, M - 1$ . The observation vector  $\mathbf{y}$  contains the observations given in Eq. (4.6). The forward stage starts by orthonormalizing the  $\mathbf{g}_r$  and updating the RSS with Gram-schmidt orthonormalization procedure described before. After adding all the column vectors for DCBs, the search for basis functions  $h_m(\mathbf{x})$  starts with minimizing the following equation:

$$RSS_m = RSS_{m-1} - \frac{\left[ \mathbf{h}_m^T \mathbf{y} - \sum_{i=0}^{m-1} \mathbf{h}_m^T \hat{\mathbf{h}}_i \hat{\mathbf{h}}_i^T \mathbf{y} - \sum_{r=1}^R \mathbf{h}_m^T \hat{\mathbf{g}}_r \hat{\mathbf{g}}_r^T \mathbf{y} \right]^2}{\mathbf{h}_m^T \mathbf{h}_m - \sum_{i=0}^{m-1} \left[ \mathbf{h}_m^T \hat{\mathbf{h}}_i \right]^2 - \sum_{r=1}^R \left[ \mathbf{h}_m^T \hat{\mathbf{g}}_r \right]^2}, \quad (4.45)$$

where,  $\hat{\mathbf{g}}_r$  are the orthonormalized column vectors  $\mathbf{g}_r$ . Note that the column vectors  $\mathbf{h}_m$  related to the VTEC are also orthonormalized with the column vectors  $\hat{\mathbf{g}}_r$ . The backward stage is the same except that the column vectors related to DCBs are not allowed to be removed from the model. The resulting model with estimates of DCBs, basis functions  $h_i(\mathbf{x})$  and their associated coefficients  $\hat{a}_i$  are selected according to the GCV criteria.

The final VTEC model in Eq. (4.25) with B-splines of order  $d$  can be written in the following open form which is decomposed into different interaction terms (Durmaz and Karslioglu, 2011):

$$\begin{aligned}
VTEC(\lambda, \varphi, t) = & a_0 + \sum_{m_1=1}^{M_1} a_{m_1} B_{d, \lambda_{n_\lambda(m_1)}^{l_\lambda(m_1)}}(\lambda) + \sum_{m_2=1}^{M_2} a_{m_2} B_{d, \varphi_{n_\varphi(m_2)}^{l_\varphi(m_2)}}(\varphi) \\
& + \sum_{m_3=1}^{M_3} a_{m_3} B_{d, t_{n_t(m_3)}^{l_t(m_3)}}(t) + \sum_{m_4=1}^{M_4} a_{m_4} B_{d, \lambda_{n_\lambda(m_4)}^{l_\lambda(m_4)}}(\lambda) B_{d, \varphi_{n_\varphi(m_4)}^{l_\varphi(m_4)}}(\varphi) \\
& + \sum_{m_5=1}^{M_5} a_{m_5} B_{d, \lambda_{n_\lambda(m_5)}^{l_\lambda(m_5)}}(\lambda) B_{d, t_{n_t(m_5)}^{l_t(m_5)}}(t) + \\
& \sum_{m_6=0}^{M_6} a_{m_6} B_{d, t_{n_t(m_6)}^{l_t(m_6)}}(t) B_{d, \varphi_{n_\varphi(m_6)}^{l_\varphi(m_6)}}(\varphi) \\
& + \sum_{m_7=1}^{M_7} a_{m_7} B_{d, \lambda_{n_\lambda(m_7)}^{l_\lambda(m_7)}}(\lambda) B_{d, \varphi_{n_\varphi(m_7)}^{l_\varphi(m_7)}}(\varphi) B_{d, t_{n_t(m_7)}^{l_t(m_7)}}(t),
\end{aligned} \tag{4.46}$$

where, the total number of terms,  $M$  is defined as  $M = 1 + \sum_{i=1}^7 M_i$ . All univariate order  $d$  B-splines  $B_{d, \lambda_{n_\lambda(m_i)}^{l_\lambda(m_i)}}(\lambda)$ ,  $B_{d, \varphi_{n_\varphi(m_i)}^{l_\varphi(m_i)}}(\varphi)$  and  $B_{d, t_{n_t(m_i)}^{l_t(m_i)}}(t)$  are generated from the sets  $C_{l_\lambda(m_i)}^\lambda$ ,  $C_{l_\varphi(m_i)}^\varphi$  and  $C_{l_t(m_i)}^t$  respectively as described in previous section, where  $l_\lambda(m_i)$ ,  $l_\varphi(m_i)$  and  $l_t(m_i)$  define the levels of order  $d$  B-splines for variables  $\lambda$ ,  $\varphi$  and  $t$  at the  $m_i^{th}$  term.  $a_0$  is the coefficient of the constant function while  $a_{m_i}$  are the coefficients of the corresponding tensor product B-splines. As can be seen from the equation, the final VTEC model built by mars can include interaction terms from different scales and variables. This indicates that, BMARS can combine B-splines with lower level for a variable with a higher level for another variable if it fits the observations better. The open form of VTEC models can deliver interesting information regarding to scales and interactions of different variables, which can be used to optimize the model building.

#### 4.5.1 Extensions and Limitations

The semi-parametric modeling described in this section is based on BMARS algorithm which constructs the basis functions from knot-locations. Since BMARS basis functions (B-splines) are compactly supported functions, the resulting VTEC maps will have a compact support also. Moreover, the support of the resulting VTEC map will be based on the available knot-locations. In order to fix the support of the modeling region, the bounding coordinates for the desired region can be injected into the knot locations. These new coordinates will be used by the algorithm to construct B-spline basis resulting in a VTEC model with a support of desired boundary.

Another extension of the algorithm can be caching the basis function evaluations computed at each search step of the forward stage if enough memory is available. This will speed up the search steps leading to improved performance. The cache can be

cleared at every increase of the level to align with the new basis functions. Moreover, sparse algorithms can be developed for the inner products utilizing the compact support property of the B-splines.

Additionally, different orders can be forced for different variables inside the algorithm. For example, order 1 B-splines may be forced for the time variable whereas order 2 B-splines can be used for latitude and longitude. This method may deliver better results if the underlying relationship is known.

Knot optimization is not considered in the description of the algorithm. Knot optimization is related to selecting knot-locations carefully so that the resulting basis functions will have enough measurements in their support to account for measurement noise. If there is not enough measurements than the estimated coefficients are highly affected by the noise in the measurements which may deliver high variance. The problem can be faced especially at the edges of the modeling region since the support of B-splines are smaller on those regions. Especially the basis functions formed of tensor products of B-splines will have smaller support. However, careful selection of scales and number of terms allowed may result in BMARS models that do not have these kind of problems.



## CHAPTER 5

### APPLICATIONS

Previous chapters provide the background information and the theory behind non-parametric and semi-parametric modeling of VTEC. The application of the developed technique to the real world data to estimate the VTEC model parameters as well as receiver DCBs are described in this chapter. Additionally, the validation of the resulting VTEC model via cross-validation and point positioning are listed. Finally, the application of the developed technique for different real world scenarios are discussed.

#### 5.1 Regional Non-Parametric VTEC Modeling

Non-parametric modeling with MARS and BMARS have been applied to regional VTEC modeling over different regions throughout the study. Some of the results related to regions over Turkey, Europe and North America have been presented as posters in European Geodesy Union (EGU) conferences on 2010, 2011 and 2012. The application of MARS algorithm for VTEC modeling over Europe is published as an article (Durmaz et al., 2010). Durmaz and Karslıoğlu (2011), on the other hand, present the results of applying BMARS algorithm for non-parametric VTEC modeling over North America. Application of BMARS for non-parametric modeling over Europe for both quiet and active ionospheric conditions are also published (Karslıoğlu and Durmaz, 2012). The summary of the publications are listed in the following subsections. The reader is referred to the publications for more details.

##### 5.1.1 Regional VTEC Modeling with MARS

Durmaz et al. (2010) applied non-parametric MARS algorithm to model VTEC on 30 January 2009 over Europe. The ground-based GPS observations are collected from EUREF and IGS network as compressed RINEX files. The receiver DCBs are estimated with Bernese GPS Software v5.0, whereas the satellite DCBs are downloaded from CODE. The VTEC observations are obtained by eliminating both satellite and receiver DCBs as described in Chapter 4. The observations and associated IPP loca-

tions in sun-fixed reference frame are then fed to the MARS algorithm implementation available in R (mda package - <http://www.r-project.org>) through a script developed in R language.

In order to display the performance of non-parametric modeling, nine different test scenarios for varying interaction degrees from 1 to 3 and maximum number of basis functions from 100 to 300 are considered. These scenarios are further tested on different temporal resolutions ranging from 15 minutes to 120 minutes. According to the results, the MARS algorithm have successfully adapted to various data sizes and interaction degrees by increasing or decreasing the number of basis functions selected. The resulting VTEC maps are validated by visual comparison to the VTEC maps estimated by the Bernese software using spherical harmonics expansion with degree 12 and order 8.

According to the results, the interaction degree is recommended as 3 (the model can contain tensor products of basis function depending on latitude, longitude and time). It is stated that the proposed method does not need a background VTEC model or gridding the region and provides solutions over regions with rare observations. The MARS algorithm is also applied to different regions which gave similar results, which are published as a poster at European Geosciences Union (EGU) General Assembly 2010 or presentations in national conferences.

### 5.1.2 Regional VTEC Modeling with BMARS

Non-parametric modeling with BMARS is applied to regional VTEC modeling over North America on 15 August 2008. The ground-based GPS observations from 32 reference stations are downloaded from UNAVCO Data Archive Interface (<http://facility.unavco.org/data/dai2/app/dai2.html>) over Internet. The DCB values for the satellites are obtained from CODE through Internet. The receiver DCBs are estimated by TecMapper (Nohutcu, 2009). The VTEC observations are obtained by eliminating both satellite and receiver DCBs as described in Chapter 4. Two test scenarios are established with 1 hour data interval centered around 19:00 UT and 20:00 UT respectively. The observations and IPP locations are then processed with MARS (R-Earth package, Milborrow et al. (2007)) and BMARS (implemented as a MATLAB routine by authors) and TecMapper in an Earth-Fixed reference frame.

The two test scenarios are executed with varying Maximum Number of Basis Functions Allowed (MBFA) from 100 to 300 in order to display how the BMARS algorithm establishes scale-by scale model building. The results showed that as the MBFA is increased, the BMARS algorithm adaptively decreases the scale of the basis functions. The resulting Root Mean Squared Error (RMSE) values indicate that BMARS can deliver similar or even smaller RMSE values with respect to both MARS and regional 3D B-splines based models. The visual comparison of the resulting VTEC maps indicate

that BMARS delivers VTEC maps with more localized features due to decreased scale. Another important result of both numerical and visual comparison is that BMARS can deliver VTEC maps with smaller number of terms than both MARS and regional 3D B-splines (Durmaz and Karslioglu, 2011). They conclude that BMARS can be a viable alternative method for regional VTEC modeling applications.

Karshoğlu and Durmaz (2012), on the other hand, applied the BMARS algorithm to demonstrate the performance on both normal and geomagnetic storm conditions. They applied the algorithm to regional VTEC modeling over Europe on 17 and 18 February 2011 with a geomagnetic storm on 18 February 2011. According to the results, BMARS algorithm delivered VTEC models with smaller RMSE values than both spherical harmonics and regional 3D B-splines via increasing the scale as necessary on days with high variance. The application of BMARS with different regions showed similar results, which are presented as posters at EGU General Assembly 2011 and 2012.

Although the algorithms have shown notable results in regional applications, the major drawback related to non-parametric modeling is that it relies on prior estimates of receiver DCBs. Kao et al. (2013) states that estimation of receiver DCBs strongly depends on the estimation of VTEC. Thus, the following section focuses on the use of regional semi-parametric modeling to overcome this issue.

## 5.2 Regional Semi-Parametric VTEC Modeling

The general strategy followed in this study for the application of semi-parametric modeling consist of three steps listed below.

- At the first step a spatial and temporal region is selected that can reveal the performance and characteristics of the method on different ionospheric conditions. Ground-based GPS observations should be available for the selected region and days. In order to assess the performance of modeling a well known and trusted products of satellite orbits, satellite and receiver DCBs and VTEC maps should be available for the selected region and days. These products are also needed for the validation test related to positioning. The details related to the spatio-temporal region, ground-stations used and modeling are listed in the following subsections.
- The second step consists of comparing the results obtained in the first step with both global ionospheric products downloaded through internet and well established regional methods of 3D B-splines. The Visual comparison for different hours reveal the response of the methods to the real world data. Both VTEC maps from different modeling techniques and difference VTEC maps are listed. And the resulting differences are discussed. The numerical comparison gives the

degree of fitting for various methods as well as comparison of estimated receiver DCBs are shown.

- In the third step, validation of the results are presented with two validation methods. The first one is the widely used statistical technique called 10-fold cross-validation for estimating the prediction error. The second validation method is based on the comparison of the resulting VTEC maps with that of GIM provided by CODE. For this, single frequency station point positioning has been carried out containing ionospheric corrections which have been calculated from these different VTEC maps. The positioning results are compared to the precise positions of the selected reference stations which have not been included in the model building.

### 5.2.1 Experiment Setup and Modeling

The semi-parametric model introduced in Section 4.5 is applied to regional VTEC modeling over Europe for days 8th, 9th and 10th of March of year 2012. The given days are selected to test the method on both quiet and active ionospheric conditions since there is a geomagnetic storm on the 9th of March. The region is selected since ground-based GPS observations from numerous ground stations are freely available through the Internet from both EUREF and IGS networks. Moreover, some of those ground stations are also used in IGS and CODE ionospheric products. Thus, estimates of receiver DCBs, which will be compared with semi-parametric modeling results, can also be obtained. Establishing the region for modeling, selection of ground-based stations, data preparation and modeling is described in the following subsections.

#### 5.2.1.1 Experiment Region

The spatial region is established to have a good compromise between being small enough to have an even data distribution and large enough to include enough satellite ray-paths for positioning. The main reason for selecting small regions above Europe is related to station density and IPP coverage. Enlarging the region may result in spatial regions where there is no or rare ionospheric observables. The station density in Europe is one of the reasons why the GIMs have good prediction accuracy over Europe. However, having a small region for VTEC modeling results in a new problem since for some receivers, there will be many satellite receiver ray-paths that have IPPs outside the model region. Unfortunately, no reliable ionospheric corrections will be available for those ray-paths leading to a poor positioning performance. This limitation can be handled to some degree by using a reference ionosphere model outside the modeling region. However, we do not use any reference ionosphere model in this study. Therefore, a region is established by a network of 32 EUREF stations which are selected to have an even data coverage of observations over a large part of Europe

as well as being large enough to include ray-paths with elevation angle larger than 10 degrees for ground based receivers which are located in the center of the region. The latter is necessary for the validation tests based on point positioning.

The distribution of stations are given in Fig. 5.1. The blue labeled stations are also used by CODE to build GIMs. Thus, the DCB estimates of those are available through IONEX formatted GIMs which can also be downloaded through Internet.

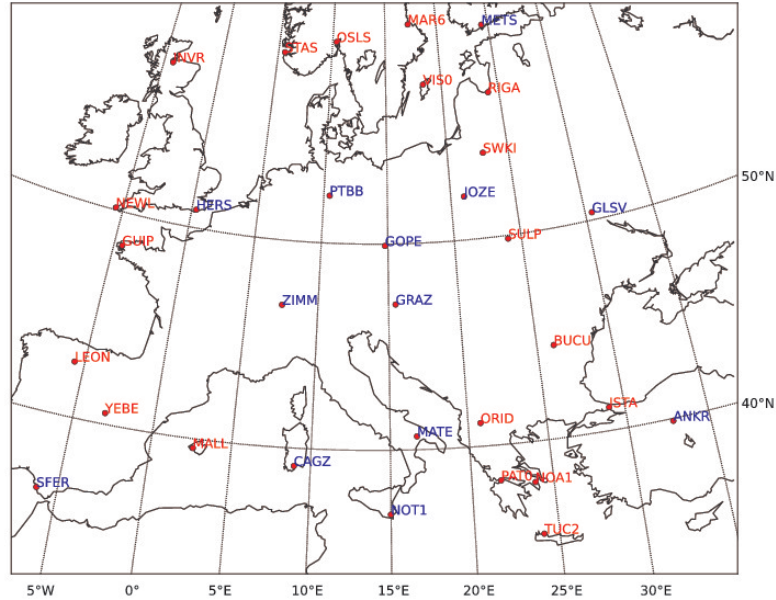
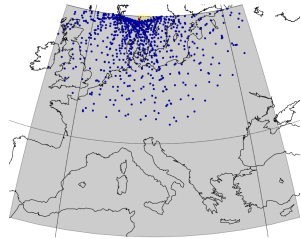


Figure 5.1: The distributions of EUREF stations used in this study. Blue labeled stations are also used for CODE Global Ionosphere Models

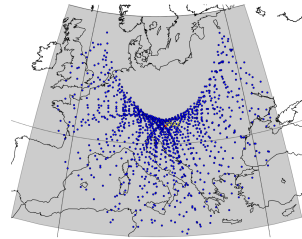
The selection of the ground-based reference stations are done by investigating the spatial distribution of the ionospheric observables they provide. A utility is developed in Python programming language to display the spatial distribution of ionospheric observables for each individual receiver. Fig. 5.2 presents the IPP coverage of individual receivers as well as the combined IPP coverage from all selected receivers on 8 March 2012. Since the GPS stations repeat their ground tracks in one sidereal day, the same pattern is expected for consecutive days. Note that, the gray region shown in the figure is the established modeling region between 34 and 60 degrees in latitudes and -7 to 35 degrees for longitudes. Table 5.1 lists the reference stations used in this study. Table also provides basic information regarding to the positions of the stations, the network which the stations belong to (TOS :TIGA Observing Stations, ECGN: European Combined Geodetic Network). More detailed information for all stations can be obtained through the EUREF web site <http://www.epncb.oma.be/>. Note that thirteen of the thirty two ground stations are also used by CODE in their ionospheric products.

Table 5.1: The ground stations used in the study for VTEC modeling

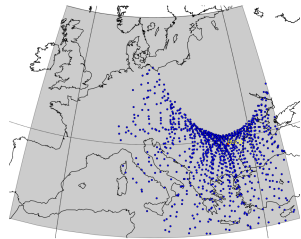
Station	Latitude	Longitude	Height	Network	CODE GIM
ANKR	39.89	32.76	974.8	IGS/EUREF	YES
BUCU	44.46	26.13	143.2	IGS/EUREF	NO
CAGZ	39.14	8.97	238.0	IGS/EUREF	YES
GLSV	50.36	30.50	226.8	IGS/EUREF	YES
GOPE	49.91	14.79	592.6	IGS/EUREF ECGN	YES
GRAZ	47.07	15.49	538.3	IGS/EUREF ECGN	YES
GUIP	48.44	-4.41	154.7	EUREF	NO
HERS	50.87	0.34	76.5	IGS/EUREF ECGN	YES
INVR	57.49	-4.22	66.2	EUREF	NO
ISTA	41.10	29.02	147.2	IGS/EUREF ECGN	NO
JOZE	52.10	21.03	141.4	IGS/EUREF ECGN	YES
LEON	42.59	-5.65	970.3	EUREF	NO
MALL	39.55	2.62	62.0	EUREF ECGN	NO
MAR6	60.60	17.26	75.4	IGS/EUREF ECGN	NO
MATE	40.65	16.70	535.6	IGS/EUREF TOS	YES
METS	60.22	24.40	94.6	IGS/EUREF TOS ECGN	YES
NEWL	50.10	-5.54	64.5	EUREF ECGN	NO
NOA1	38.05	23.86	537.8	EUREF	NO
NOT1	36.88	14.99	126.2	IGS/EUREF	YES
ORID	41.13	20.79	773.0	IGS/EUREF	NO
OSLS	59.74	10.37	221.0	EUREF	NO
PAT0	38.28	21.79	121.0	EUREF	NO
PTBB	52.30	10.46	130.2	IGS/EUREF	YES
RIGA	56.95	24.06	34.7	IGS/EUREF	NO
SFER	36.46	-6.21	85.8	IGS/EUREF	YES
STAS	59.02	5.60	105.0	EUREF ECGN	NO
SULP	49.84	24.01	370.5	IGS/EUREF	NO
SWKI	54.10	22.93	216.4	EUREF	NO
TUC2	35.53	24.07	161.0	EUREF	NO
VIS0	57.65	18.37	79.8	IGS/EUREF ECGN	NO
YEBE	40.52	-3.09	973.0	IGS/EUREF ECGN	NO
ZIMM	46.88	7.47	956.7	IGS/EUREF ECGN	YES



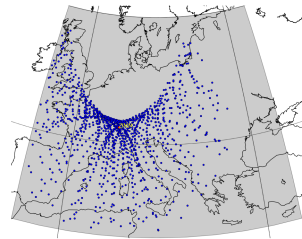
(a) OSLS ground station IPP coverage



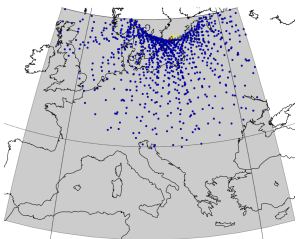
(b) GRAZ ground station IPP coverage



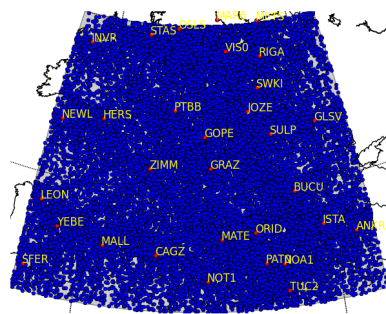
(c) BUCU ground station IPP coverage



(d) ZIMM ground station IPP coverage



(e) VISO ground station IPP coverage



(f) IPP coverage from all stations

Figure 5.2: IPP coverages from some ground stations, as well as full day coverage from all selected stations on day 8 March 2012 with a decimation of 10 min.

### 5.2.1.2 Data Preparation

Data preparation is an important part of any scientific study. In this study, the key data is ground based GPS observations of code pseudo-ranges and carrier phases. Thanks to national and international ground based GPS networks which provide their raw measurements as well as derived products, the GPS related data can be easily obtained. The process of data preparation is described in the following paragraphs.

#### Observation and Navigation Files

GPS receivers generally use their own propriety format to store the GPS related measurements as well as receiver status. However, the exchange of this information independent of the receiver type is crucial for combined use of the measurements by independent groups. There are two widely adopted exchange standards exist: The National Marine Electronics Association (NMEA) and Receiver Independent Exchange Format (RINEX). Although it is developed as an interface between different kind of marine equipment, NMEA is widely used for reading GPS measurements from a GPS receiver via serial communication. The RINEX format on the other hand is an ASCII text file, that contains metadata of the contents of the file as well as receiver specific information in the header. And lists the measurements from individual satellites from different GNSS systems for each epoch. The RINEX format can also represent the decoded navigation message by individual receivers. In order to reduce the size of the RINEX files, a compressed version of the RINEX format has been developed by Y. Hatanaka. A utility for the compression and decompression of the Hatanaka compressed RINEX files is available from <http://terras.gsi.go.jp/ja/crx2rnx.html>

Ground-based raw GPS observations with navigation messages are downloaded from the EUREF Internet archive site <ftp://ftp.epncb.oma.be/pub/>. The observation files are located at `obs/{year}/{day of year}` sub directory. The RINEX observation file names are coded as `ssssddd.f.yyt`, where `ssss` is the four character ground station designator, `ddd` is the day of year padded with zeros, `f` is the file sequence number when the data during day is fragmented, `yy` is year, `t` is the file type. This study uses observation files (O) and navigation files (N). The days 8,9 and 10 March 2012 corresponds to days of year 68, 69 and 70 respectively. Both the navigation files and compressed raw measurements of ground based stations listed in previous subsection and reference stations for positioning are downloaded from the EUREF FTP site. They are further decompressed by the Hatanaka decompression utility mentioned above.

#### IGS Orbit Products

The final orbit products from IGS site are used in this study for both TEC extraction and positioning. The final IGS orbit products have an accuracy around 2.5 cm compared to 2 m for navigation files. The IGS satellite ephemerides and clock products can be downloaded from FTP sites listed in <http://igs.cb.jpl.nasa.gov/components/prods.html>. The file name convention is *igswwwwd.sp3*, where *www* is the GPS week number and *d* is the day of week. The IGS orbit and clock product is distributed in the SP3 file format for which a detailed description is available from <ftp://igs.cb.jpl.nasa.gov/pub/data/format/sp3c.txt>. The GPS week number for the three days used in this study is 1678 where the days 8,9 and 10 March corresponds to the days 4,5 and 6 of the week respectively.

### Code DCB Estimates

As described in Chapter 4 the DCB estimates of both satellites and receivers are important parameters in ionosphere modeling with GNSS. This study uses satellite DCB eliminated observations to estimate the spatio-temporal distribution of VTEC as well as receiver DCBs. Fortunately, Center for Orbit Determination in Europe provides daily and monthly averages of both satellite and receiver DCBs. Since some of the receivers provide only C1 observable instead of P1, both P1-C1 and P1-P2 satellite DCBs must be taken into account. The monthly averages of DCBs for satellites and receivers (receivers that are used by CODE in estimating GIMs) can be downloaded from the FTP site <ftp://ftp.unibe.ch/aiub/CODE/>. More information related to CODE GIMs and estimates can be found from <http://aiuws.unibe.ch/ionosphere/>. The file name convention used by CODE is *P1P2yyymm\_ALL.DCB.Z*, where *yy* represents the year, *mm* represents the month. The files are compressed with UNIX compress utility.

### Code GIMs

This study uses Global Ionosphere Maps (GIMs) published by CODE for comparison of estimated VTEC distribution and receiver DCBs and for validation purposes. CODE provides Global Ionosphere Maps (GIMs) since January 1, 1995 which can be downloaded from <ftp://ftp.unibe.ch/aiub/CODE/>. GIMs are based on ground-based GPS and GLONAS observations from 150 sites distributed around the world. Most of the sites also belong to the IGS network. Spatial distribution of VTEC generated by GIMs is represented by spherical harmonics expansions up to degree and order of 15. The temporal representation is piece-wise linear functions. There are 13 VTEC maps, with a spacing of 2 hours in a single GIM. The reference frame used in estimation of the coefficients is the sun-fixed geomagnetic reference frame, whereas the resulting VTEC maps are in the Earth-Fixed reference frame. They are published in

both IONEX and Bernese ION formats. IONEX format provides gridded VTEC map snapshots with a grid interval of 5 degrees to 2.5 degrees in longitude and latitude respectively. Moreover, IONEX format also can optionally contain the estimated DCBs for both satellites and receivers.

The file name convention of IONEX files adopted by CODE for GIMs is *CODGddd0.yyI*, where *yy* is the year, *ddd* is the day of year. The Bernese ION files, on the other hand, have the file name convention depending on the GPS week number : *CODwwwd.ION*, where *www* is the GPS week number and *d* is the day of week. The week and day numbers used in this study are given in previous paragraphs.

## Extracting STEC

The satellite DCB eliminated STEC values are calculated from geometry free linear combination described in Chapter 3 and 4 by TecMapper software (Nohutcu, 2009). RINEX observation files originated from receivers are used to form carrier smoothed geometry-free linear combinations after cycle-slips are detected and fixed. The satellite DCBs (both P1-P2 and P1-C1 depending on the receiver characteristics) are eliminated from the combination as described in Chapter 4. The satellite positions are obtained through the interpolation of satellite positions given in precise IGS orbit products mentioned above. The approximate station coordinates available in RINEX files are used with satellite coordinates to form ray-paths from receiver to satellites. The calculated satellite DCB eliminated STEC values with corresponding satellite number, elevation and azimuth are stored for each epoch on a MATLAB .mat file. These files corresponding to each receiver for each day are used to obtain VTEC and DCB estimates as described in the following subsection.

### 5.2.1.3 Modeling

The satellite DCB eliminated STEC values calculated by TecMapper are used to construct the observation vector given in Eq. (4.6). For every receiver, the TecMapper generated files are reprocessed by establishing a Single Layer Model with a mean Earth radius of 6371 km. The ionospheric shell height of 450 km and an elevation cut-off angle of 10 degrees is selected. The STEC values are then converted to VTEC related values (including the unknown receiver DCBs also) by applying the mapping function as shown in Eq. (4.6). The coordinates for Ionospheric Pierce Points (IPPs) are calculated using the receiver coordinates and estimated satellite zenith and azimuth angles as given in Eq. (4.7). Stacking all the measurements coming from all receivers and the associated IPP coordinates (knot locations), we obtain the observation equation given in Eq. (4.44). The semi-parametric modeling defined in Section 4.5 are applied to solve the observation equation.

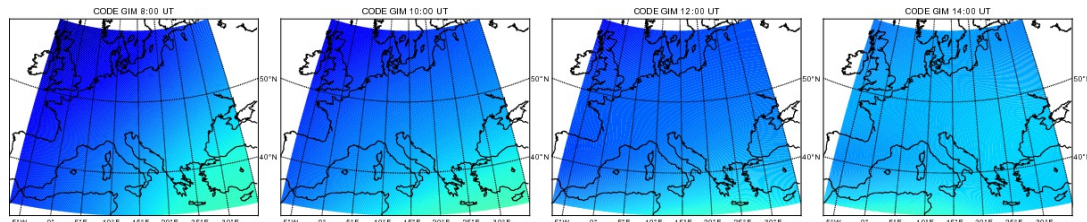
Durmaz et al. (2010) analysed the behaviour of non-parametric modeling with varying interaction degrees and basis functions. They also analysed the response of the MARS method for different temporal resolutions. Durmaz and Karslioglu (2011) on the other hand presented the behaviour of BMARS algorithm for varying basis functions and selection of scales. In this part of the study, we focus on the use of semi-parametric modeling with BMARS with Bsplines of different order. Thus, the semi-parametric VTEC models used in this part of the thesis is based on BMARS with B-splines of order 1, 2 and 3 in an Earth-Fixed reference frame. Since the ionospheric activity is mainly related to the Sun position, we choose 08:00 UT, 10:00 UT, 12:00 UT and 14:00 UT hours for VTEC modeling depending on daylight over Europe. The semi-parametric VTEC models are estimated from observations using a time window of 2 hours centered at given hours for each day. Moreover, the observations are spatially clipped to the modeling region. The observations are further decimated with 3 minutes to suit the computational resources available. The VTEC maps, numerical results related to comparisons and validation are all referred to these hours. Another reason for choosing even hours is to compare the resulting VTEC maps of CODE since GIMs provide snapshots of VTEC for even hours.

For each hour in each day, a new semi-parametric VTEC model is established. The maximum number of terms allowed is chosen as 150 for all maps. In order to compare the results, another regional VTEC modeling method based on 3D B-splines introduced in Chapter 4 is used in an Earth-Fixed reference frame. Instead of using a reference VTEC model such as IRI, level 0 3D B-splines estimation is used as a reference. The B-spline levels are chosen as 3 for latitude, longitude and time. The maximum level allowed in semi-parametric models is limited to 3 to comply with the 3D B-spline modeling. Exactly the same measurements are used to estimate the VTEC model coefficients and receiver DCBs in semi-parametric modeling and 3D B-splines modeling. The following section provides the VTEC maps obtained for every hour in each day and compares the results.

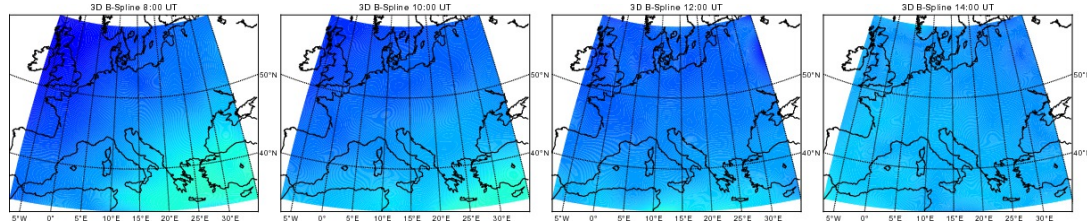
### 5.2.2 Visual Comparison of Results

The VTEC maps generated from CODE GIMs, regional 3D B-splines and regional semi-parametric BMARS with order 1,2 and 3 B-splines are given in Fig. 5.3, 5.4 and 5.5 for 8th, 9th and 10th of March 2012 respectively. A general consistency can be observed on each day for different models. However, local variations can be observed on both regional 3D B-spline and BMARS models. This is an expected result since CODE GIMs are based on spherical harmonics expansion which are smooth global functions.

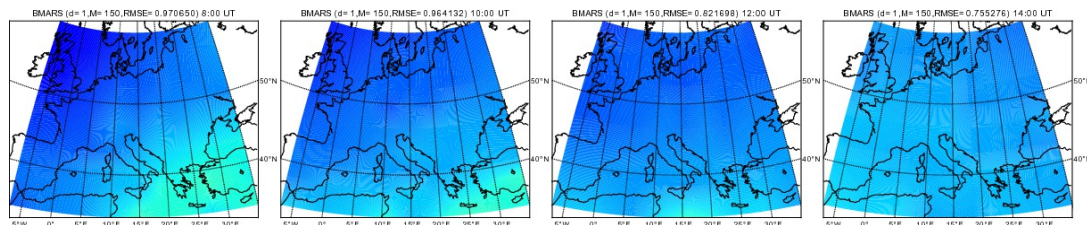
In order to observe the variations of BMARS models with respect to both CODE GIMs and regional 3D B-splines, the difference VTEC maps are generated. Fig. 5.6, 5.7 and 5.8 display the difference VTEC maps between the BMARS and CODE GIMs for each



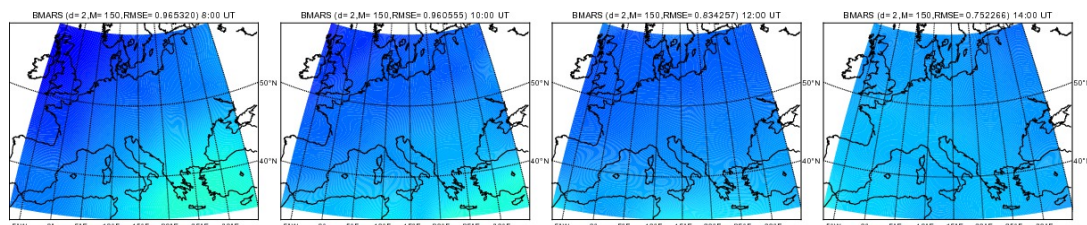
(a) CODE GIM VTEC Maps for 8:00,10:00,12:00,14:00 UT on 8th of March 2012



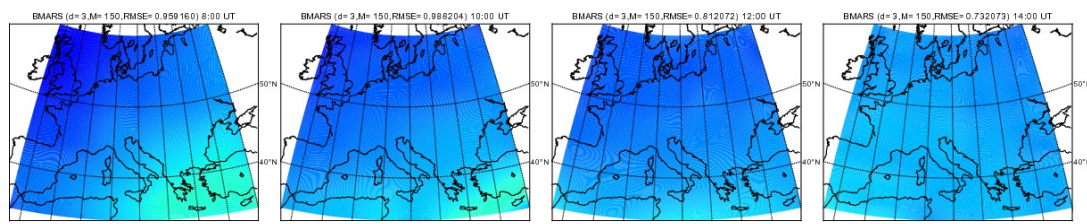
(b) 3D B-Spline VTEC Maps for 8:00,10:00,12:00,14:00 UT on 8th of March 2012



(c) BMARS  $d=1$   $M=150$  VTEC Maps for 8:00,10:00,12:00,14:00 UT on 8th of March 2012



(d) BMARS  $d=2$   $M=150$  VTEC Maps for 8:00,10:00,12:00,14:00 UT on 8th of March 2012



(e) BMARS  $d=3$   $M=150$  VTEC Maps for 8:00,10:00,12:00,14:00 UT on 8th of March 2012

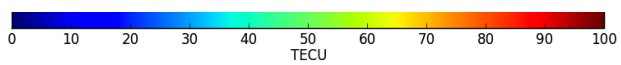
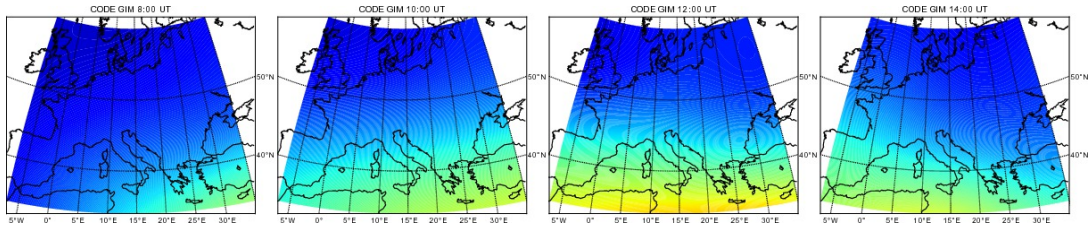
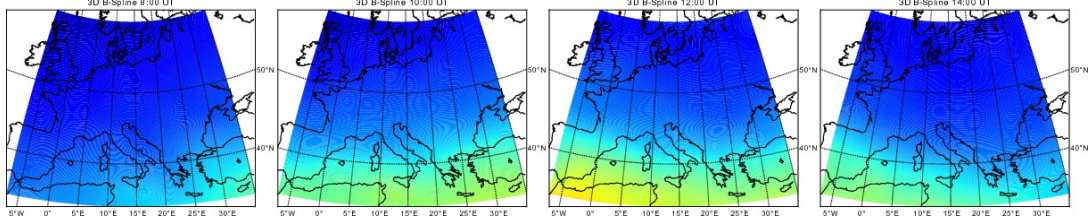


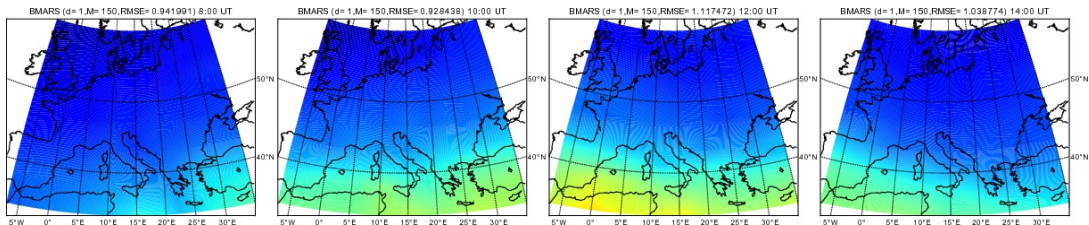
Figure 5.3: Global and Regional VTEC maps for day 8th of March 2012



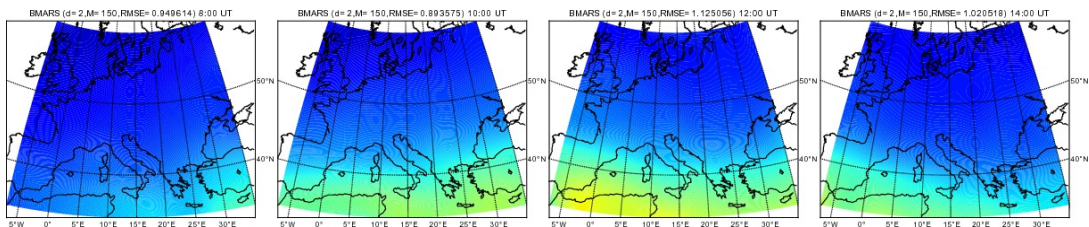
(a) CODE GIM VTEC Maps for 8:00,10:00,12:00,14:00 UT on 9th of March 2012



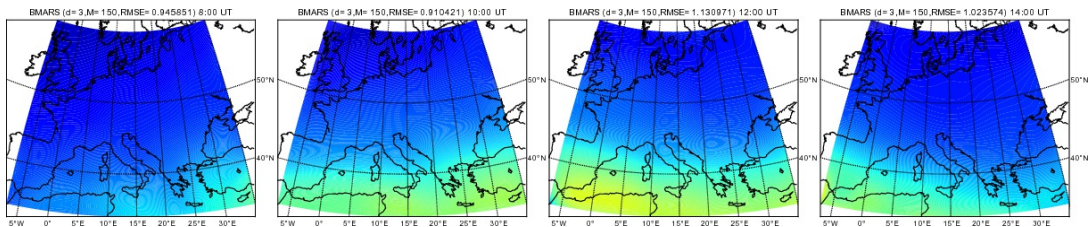
(b) 3D B-Spline VTEC Maps for 8:00,10:00,12:00,14:00 UT on 9th of March 2012



(c) BMARS d=1 M=150 VTEC Maps for 8:00,10:00,12:00,14:00 UT on 9th of March 2012



(d) BMARS d=2 M=150 VTEC Maps for 8:00,10:00,12:00,14:00 UT on 9th of March 2012



(e) BMARS d=3 M=150 VTEC Maps for 8:00,10:00,12:00,14:00 UT on 9th of March 2012

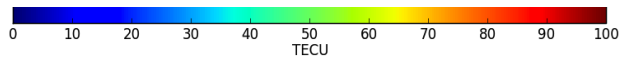
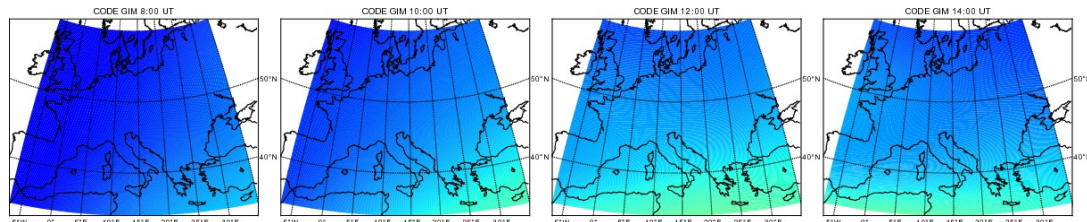
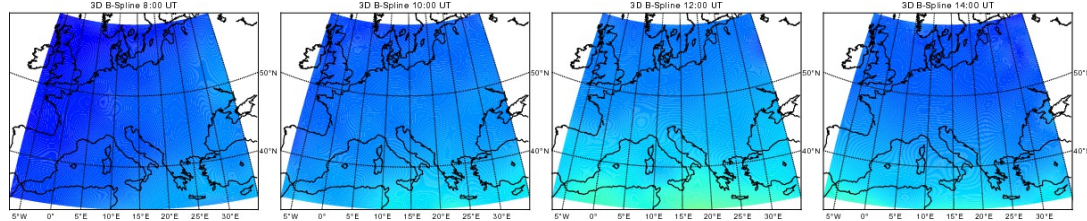


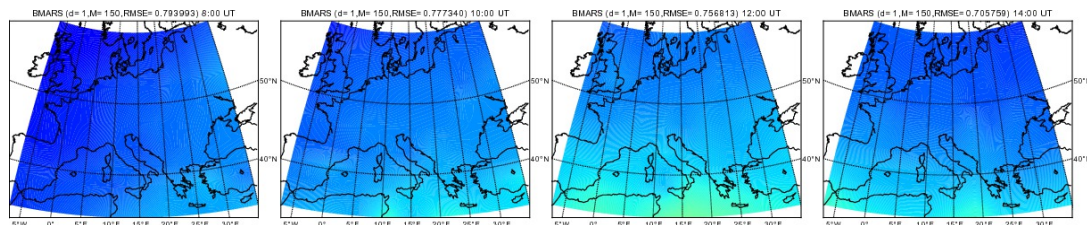
Figure 5.4: Global and Regional VTEC maps for day 9th of March 2012



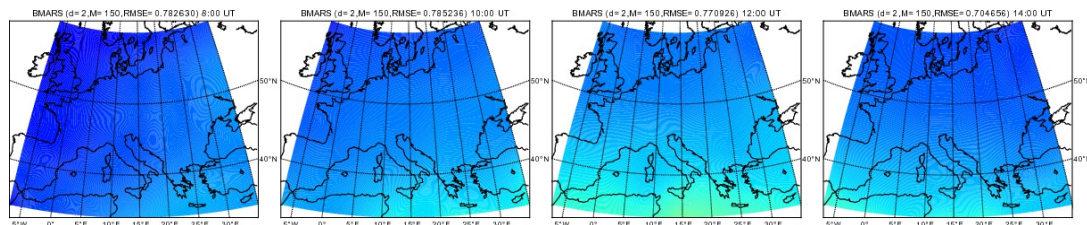
(a) CODE GIM VTEC Maps for 8:00,10:00,12:00,14:00 UT on 10th of March 2012



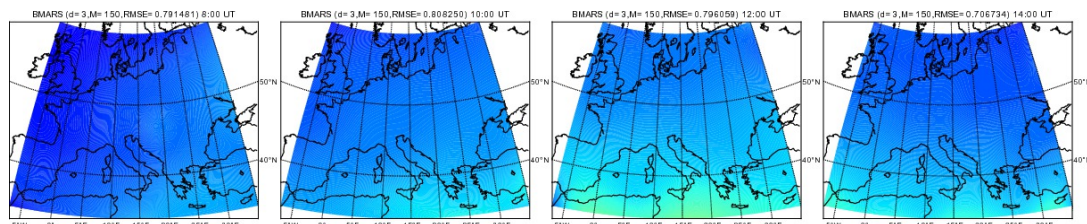
(b) 3D B-Spline VTEC Maps for 8:00,10:00,12:00,14:00 UT on 10th of March 2012



(c) BMARS  $d=1$   $M=150$  VTEC Maps for 8:00,10:00,12:00,14:00 UT on 10th of March 2012



(d) BMARS  $d=2$   $M=150$  VTEC Maps for 8:00,10:00,12:00,14:00 UT on 10th of March 2012



(e) BMARS  $d=3$   $M=150$  VTEC Maps for 8:00,10:00,12:00,14:00 UT on 10th of March 2012

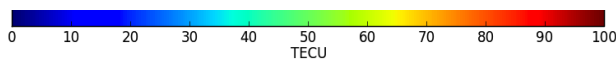


Figure 5.5: Global and Regional VTEC maps for day 10th of March 2012

day. According to the figures, variations ranging from -10 to 10 TECU are observed on each day. On 9 March 2012, where there is a geomagnetic storm, variations are even higher than the other days especially for 12:00 UT to 14:00 UT. These are the hours when the ionospheric electron content over Europe attains its maximum. Observe that BMARS models provide lower VTEC values especially at the lower right corner of the figures. Same kind of variation exists also on the other days with relatively smaller variations. On the other hand, higher VTEC values are delivered by BMARS models with respect to the CODE GIMs on the left of the figures. These variations are attributed to the local support of basis functions used in BMARS and observation clipping due to regional modeling. The coefficients of CODE GIMs may be affected by the higher VTEC observations especially near the Equator. Another cause for these kind of variations can be attributed to the data distribution.

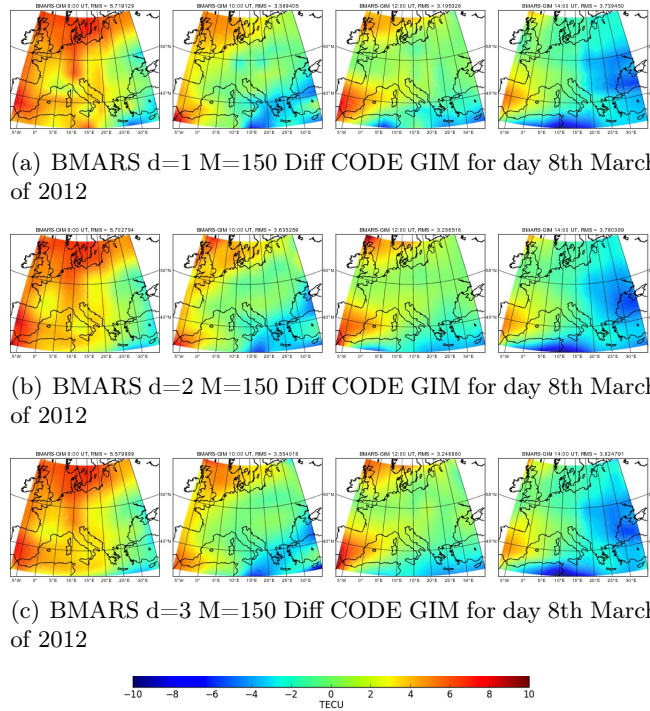
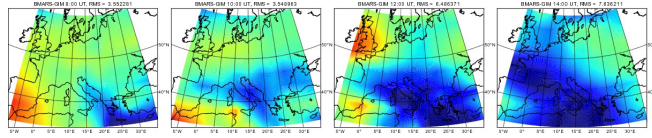
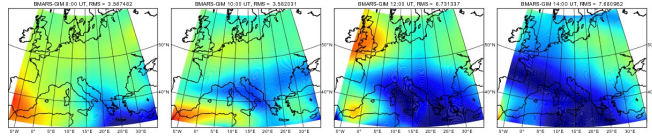


Figure 5.6: VTEC Difference Maps between different BMARS Models and CODE GIM on the 8th of March 2012

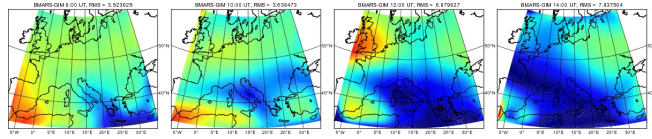
The difference maps between BMARS models and 3D B-splines for the selected days are given in Fig. 5.9, 5.10 and 5.11. The difference VTEC maps show a clear decrease in the variations compared to the difference maps of CODE GIMs. This indicates that BMARS delivers similar VTEC maps with 3D B-splines. The obvious reason for the similarity is the use of similar kind of basis functions on the same data set. However, variations in 1-3 TECU on the average can also be observed between BMARS and 3D B-splines. The variations are especially obvious at the edges of the modeling region. The main cause of this kind of variation is attributed to the fact that knot-optimization mentioned in Chapter 4 is not implemented in the BMARS algorithm. 3D B-splines,



(a) BMARS d=1 M=150 Diff CODE GIM for day 9th March of 2012



(b) BMARS d=2 M=150 Diff CODE GIM for day 9th March of 2012



(c) BMARS d=3 M=150 Diff CODE GIM for day 9th March of 2012

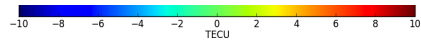
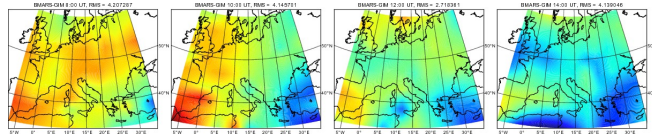
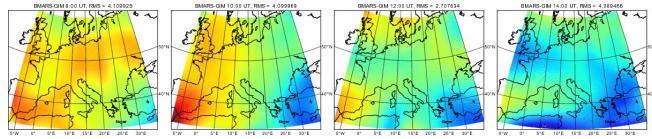


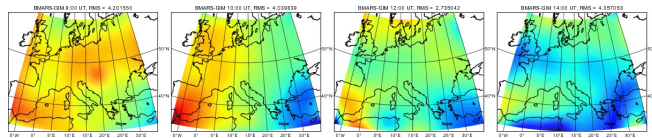
Figure 5.7: VTEC Difference Maps between different BMARS Models and CODE GIM on the 9th of March 2012



(a) BMARS d=1 M=150 Diff CODE GIM for day 10th March of 2012



(b) BMARS d=2 M=150 Diff CODE GIM for day 10th March of 2012



(c) BMARS d=3 M=150 Diff CODE GIM for day 10th March of 2012

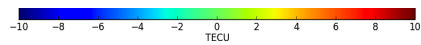
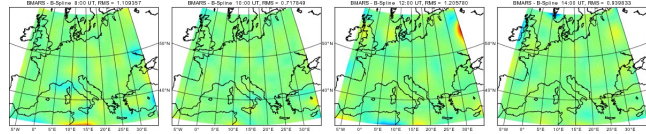
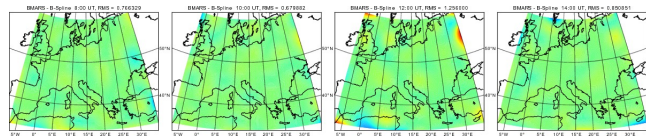


Figure 5.8: VTEC Difference Maps between different BMARS Models and CODE GIM on the 10th of March 2012

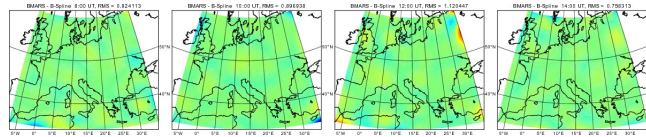
on the other hand, use Tikhonov regularization to overcome this kind of situations. Another interesting result is that BMARS models with different orders of B-Splines deliver VTEC maps very close to each other. The main reason for this is the adaptive model building applied by the BMARS algorithm. Note that, the smoothness of the resulting VTEC maps depend on the order of B-splines used. A numerical comparison of the results are given in the following section.



(a) BMARS  $d=1$   $M=150$  Diff 3D B-splines for day 8th March of 2012



(b) BMARS  $d=2$   $M=150$  Diff 3D B-splines for day 8th March of 2012



(c) BMARS  $d=3$   $M=150$  Diff 3D B-splines for day 8th March of 2012

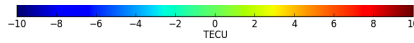
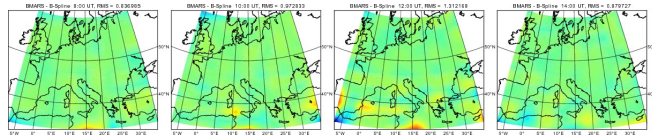


Figure 5.9: VTEC Difference Maps between different BMARS Models and 3D B-splines on the 8th of March 2012

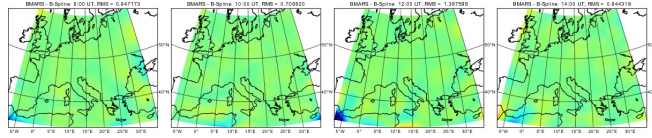
### 5.2.3 Numerical Comparison of Results

The Root Mean Square (RMS) differences for each difference VTEC map are given in Table 5.2, 5.3 and 5.4. Although the RMS values of difference maps between BMARS (with orders 1,2 and 3) and 3D B-splines are close to each other, the RMS value for order 2 BMARS is generally smaller. This is an expected result as mentioned in the previous section. The RMS values of differences between BMARS and 3D B-splines for 12:00 UT are higher especially on 9th of March 2012 for order 3 B-splines. This is mainly related to the artifacts especially at the edges of the modeling region. These artifacts are attributed to the lack of knot-optimization as mentioned in the previous section.

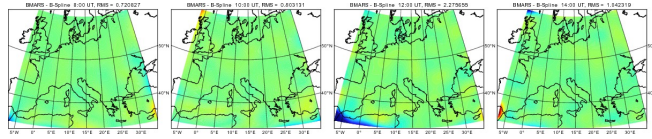
As expected, the RMS values for the differences between BMARS and CODE GIMs are higher reaching up to 7.6 TECU at 14:00 UT on the 9th of March.



(a) BMARS d=1 M=150 Diff 3D B-splines for day 9th March of 2012



(b) BMARS d=2 M=150 Diff 3D B-splines for day 9th March of 2012



(c) BMARS d=3 M=150 Diff 3D B-splines for day 9th March of 2012

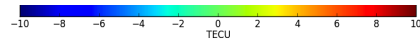
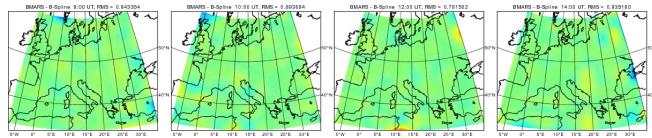
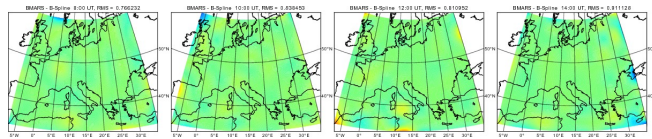


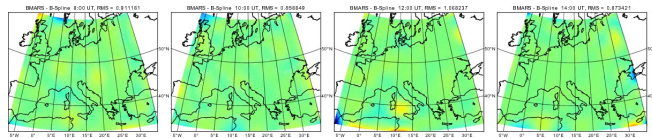
Figure 5.10: VTEC Difference Maps between different BMARS Models and 3D B-splines on the 9th of March 2012



(a) BMARS d=1 M=150 Diff 3D B-splines for day 10th March of 2012



(b) BMARS d=2 M=150 Diff 3D B-splines for day 10th March of 2012



(c) BMARS d=3 M=150 Diff 3D B-splines for day 10th March of 2012



Figure 5.11: VTEC Difference Maps between different BMARS Models and 3D B-splines on the 10th of March 2012

Table 5.2: The RMS of differences between BMARS and both CODE GIMs and 3D-Bsplines for 8 March 2012

order	Diff. to 3D-Bspline				Diff. to CODE GIM			
	08:00	10:00	12:00	14:00	08:00	10:00	12:00	14:00
1	1.1093	0.7179	1.2058	0.9398	5.7191	3.5994	3.1953	3.7394
2	0.7663	0.6798	1.2560	0.8509	5.7028	3.6353	3.2565	3.7904
3	0.8241	0.8969	1.1204	0.7583	5.5799	3.5540	3.2469	3.8248

Table 5.3: The RMS of differences between BMARS and both CODE GIMs and 3D-Bsplines for 9 March 2012

order	Diff. to 3D-Bspline				Diff. to CODE GIM			
	08:00	10:00	12:00	14:00	08:00	10:00	12:00	14:00
1	0.8369	0.9728	1.3121	0.8797	3.5523	3.5490	6.4864	7.6372
2	0.8471	0.7098	1.3976	0.8443	3.5875	3.5820	6.7313	7.6809
3	0.7208	0.8031	2.2756	1.0423	3.5236	3.6385	6.8796	7.8375

Table 5.4: The RMS of differences between BMARS and both CODE GIMs and 3D-Bsplines for 10 March 2012

order	Diff. to 3D-Bspline				Diff. to CODE GIM			
	08:00	10:00	12:00	14:00	08:00	10:00	12:00	14:00
1	0.8434	0.8937	0.7815	0.9352	4.2073	4.1457	2.7184	4.1390
2	0.7662	0.8385	0.8109	0.9111	4.1099	4.0999	2.7076	4.0894
3	0.9112	0.8588	1.0682	0.8734	4.2015	4.0398	2.7350	4.0571

Fig. 5.12 shows the Root Mean Squared Error (RMSE) of the BMARS and 3D B-spline models for each day. Table 5.5, on the other hand, lists the number of selected terms inside the models. According to the figure, the RMSE of 3D B-spline models are lower than the BMARS models although the difference is small (about 0.1 TECU). As for the VTEC maps, the RMSE of the BMARS models with different orders are close to each other. However, the number of selected terms differ as shown in Table 5.5. For example, on the 8th of March, the number of selected terms for order 2 BMARS model at 08:00 UT is 138. On the other hand, order 1 and 3 BMARS models contain 132 and 149 terms to represent similar VTEC maps. As shown in the Fig. 5.12, the resulting RMSE values are very close to each other. From the figure and the table, it can be said that the BMARS model with order 2 B-splines tends to consume less number of terms than the order 1 and 3 BMARS. Moreover, note that the BMARS models on 9th and 10th of March nearly reach to the limit of maximum number of terms allowed, which is 150. This indicates that for those days, BMARS found more significant terms describing the spatio-temporal variations of VTEC.

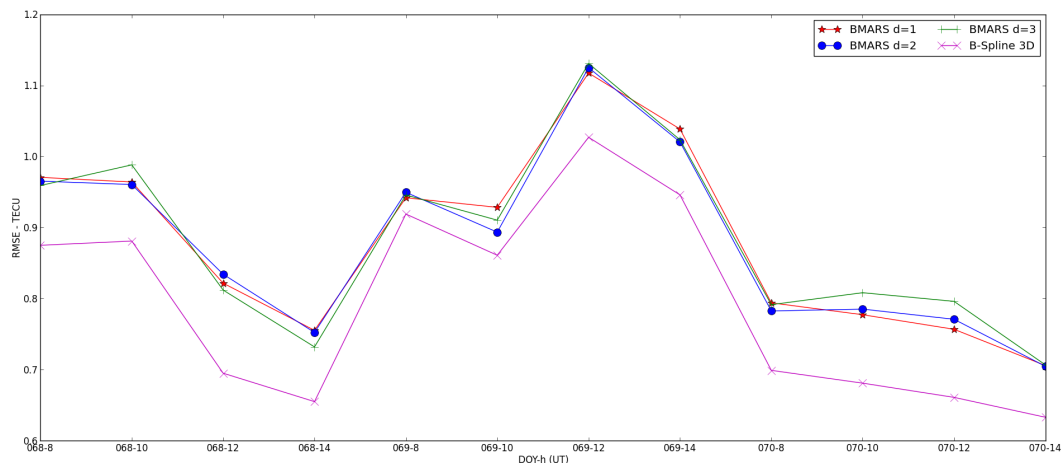


Figure 5.12: RMSE of BMARS and 3D B-spline models for three days

Another obvious result of Fig. 5.12 is that the RMSE values of BMARS and 3D B-spline models are strongly correlated. This is also an indicator of the fact that BMARS can deliver similar VTEC Maps, with similar RMSE values with respect to 3D B-spline based methods. Moreover, due to its adaptive model building strategy, the number of terms required are less compared to 3D B-spline models. The number of parameters used by 3D B-spline models is  $(2^3 + 2)^3 = 1000$ . Note that, Tikhonov regularization applied in the estimation process can set some of the B-spline coefficients close to zero which is similar to the subset selection procedure applied in the backward elimination procedure of BMARS.

The numerical results and figures given above are all related to the spatio-temporal variations of the VTEC. Fig. 5.13, on the other hand, displays the estimated DCB

Table 5.5: The number of selected terms for BMARS models with different orders on 8, 9 and 10 March 2012

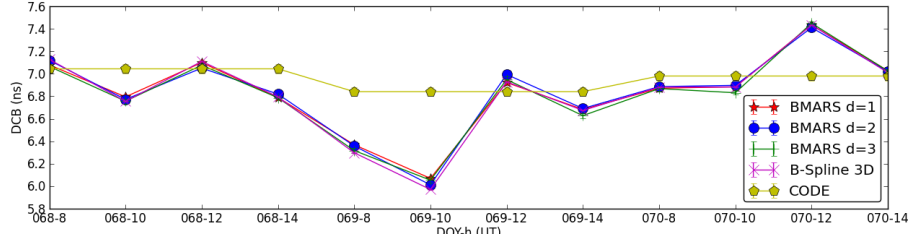
Hour	8 March			9 March			10 March		
	1	2	3	1	2	3	1	2	3
08:00 UT	132	128	149	140	138	149	148	149	148
10:00 UT	148	148	149	140	149	149	149	147	149
12:00 UT	115	103	137	148	148	149	148	148	149
14:00 UT	104	106	130	148	149	149	148	148	149

values for selected receivers. The figures for all receivers can be found at the Appendix. The selected receivers are among the ones used by CODE in estimating GIMs. Thus, the IONEX files obtained from CODE contain the daily estimates of the receivers. The receiver DCBs are assumed to be constant during the day, the variations at the day boundaries can be seen inside the figure. The receiver DCBs estimated by BMARS and 3D B-splines methods are assumed to be constant during two hours of modeling intervals. Thus, the estimates vary within the day as clearly visible inside the figure. The variations with respect to CODE DCB estimations are within the range of 1-3 ns.

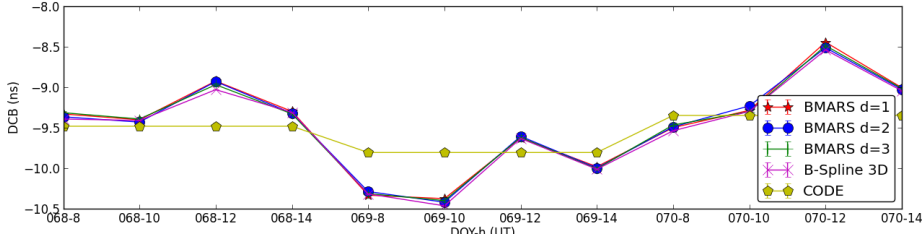
As in the case of RMSE values, the receiver DCB estimates of 3D B-splines and BMARS models deliver approximately the same results, Note that the figure also displays the  $1\sigma$  error bound for individual estimates. However, they are hardly be seen since they are very small (in the range of 0.01-0.05 ns for BMARS and 3D B-splines and 0.04 to 0.09 ns for CODE GIMs). This is related to the strong functional relationship between the receiver DCBs and the ionospheric observable.

The numerical results presented in this section combined with the visual comparison reveal that semi-parametric BMARS models with different order B-splines deliver similar VTEC maps with close RMSE values. The estimated receiver DCBs are also closer to each other. Semi-parametric BMARS algorithm selects the required number of terms to represent spatio-temporal representation of VTEC as well as delivers receiver DCBs. Note that, since selection of terms depend on their descriptive power (the contribution to the RMSE), the number of selected terms may change for different regions and ionospheric conditions. Although, the number of terms differ, the resulting RMSE values and DCB estimates are close to each other thanks to the backward elimination stage which is powered by Generalized Cross Validation (GCV) .

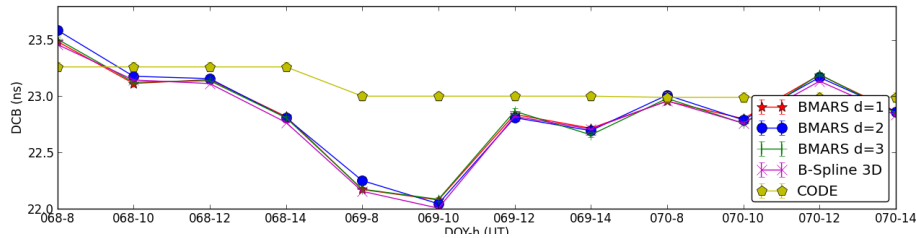
The results also showed that BMARS can deliver similar values with the 3D B-spline based method with less number of terms. And are also in parallel with the results of Durmaz et al. (2010) and Durmaz and Karslioglu (2011). The following section performs the validation tests based on 10-fold cross validation and single-frequency point positioning.



(a) DCB estimates on different hours for GOPE station



(b) DCB estimates on different hours for JOZE station



(c) DCB estimates on different hours for ZIMM station

Figure 5.13: DCB estimates of selected ground stations for each days

## 5.2.4 Validation Results

The previous section compared the semi-parametric BMARS models with well known regional 3D B-spline and global CODE GIMs. In this section, the prediction performance of BMARS models with different orders are validated. Firstly, the BMARS models are compared according to their 10-fold cross validation scores. Then, in the next subsection, The estimated VTEC maps are used in their intended environment to correct for ionospheric delays in single frequency point positioning.

### 5.2.4.1 Cross-Validation Results

The Mean Squared Error (MSE) is a widely used metric for selecting the best fitting model to the measurements. For a measurement data set  $(y_i, \mathbf{x}_i), i = 1, 2, \dots, N$ , the MSE can be written as:

$$MSE(\hat{f}) = \frac{1}{N} \sum_{i=1}^N (y_i - \hat{f}(\mathbf{x}_i))^2, \quad (5.1)$$

where,  $\hat{f}(\mathbf{x})$  is the estimated approximate function for the unknown true function  $f(\mathbf{x})$ . Usually the estimation methods such as least squares find the function that minimize the MSE. However, the MSE is not a good estimate for the prediction error which is defined as the error between independent measurements and the predicted values or estimated observations. The Expected Prediction Error (EPE) can be written as:

$$EPE(\hat{f}) = E\{(y - \hat{f}(\mathbf{x}))^2\}, \quad (5.2)$$

where,  $y \notin \{y_1, y_2, \dots, y_N\}$ . In our case, the estimated function  $\hat{f}(\mathbf{x})$  includes both the receiver DCBs and spatio-temporal variation of VTEC as given in Eq. (4.43). Thus, we cannot use ionospheric measurements from independent receiver to get an estimate for prediction error since their DCBs are not estimated. The next section uses measurements from independent receivers to validate the prediction accuracy of ionospheric delays predicted by the non-parametric part of the function related to VTEC.

Cross-Validation is a simple and widely used tool to estimate the EPE. If the data set to be used in the estimation process is large enough, it can be randomly divided into  $k$  equally sized subsets. In this study,  $k = 10$  leading to 10-fold cross validation. For each subset  $y^k$  from 1 to 10, the function  $\hat{f}(\mathbf{x})$  is estimated by the combination of remaining subsets  $y^i, i \neq k$ . Then, the squared errors  $(y_i^k - \hat{f}^{-k}(\mathbf{x}))^2$  are summed up for each subset to obtain the cross-validation score defined as (Hastie et al., 2001):

$$CV(\hat{f}) = \frac{1}{N} \sum_{i=1}^N (y_i - \hat{f}^{-k}(\mathbf{x}_i))^2, \quad (5.3)$$

where,  $\hat{f}^{-k}(\mathbf{x})$  is the function estimate obtained from combined subsets excluding subset  $y^k$ . In this study, we use randomized splits at each iteration instead of fixed splitting. This results in a Monte-Carlo like estimation for the cross-validation score. The randomization is also necessary since the measurement data contains stacked measurements from each receiver. If its is not applied then some folds may not contain any measurements related to some receivers. Another cross-validation strategy is to separate only one measurement from the data set at each iteration leading to  $N$  iterations. This strategy is widely known as the leave-one-out cross-validation. The Generalized Cross Validation (GCV), which is an analytical approximation for leave-one-out cross-validation, has already been introduced in Chapter 4. GCV is used in the backward stage of MARS and BMARS algorithms to select the best model.

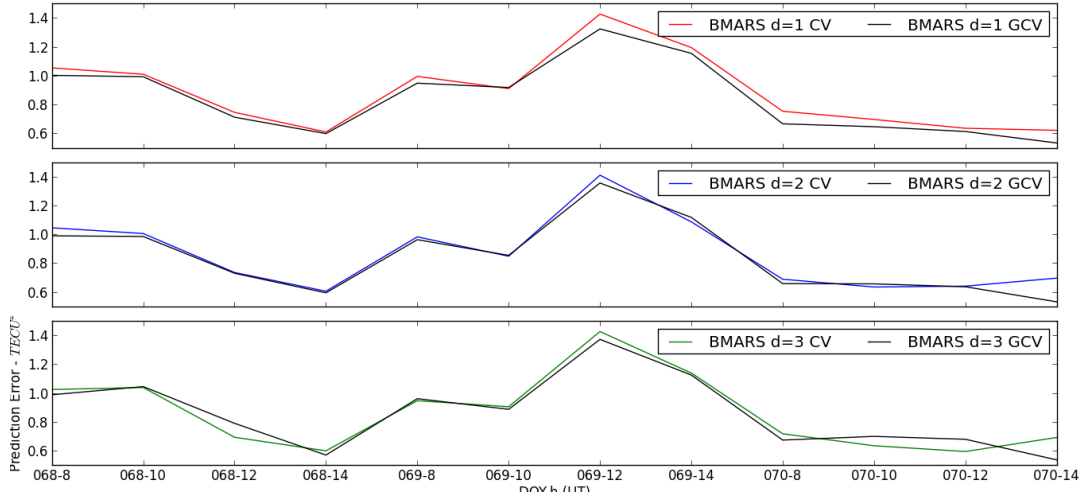


Figure 5.14: 10-Fold Cross Validation Results of BMARS models with B-splines of different orders

In order to compare EPEs of BMARS models with different orders, 10-fold Cross-Validation (CV) is applied on each hour for each day. Fig. 5.14 displays the results of the 10-fold cross validation scores (in  $TECU^2$ ) and the GCV scores (also in  $TECU^2$ ) in the same figure. As can be observed from the figure, the GCV scores and CV scores are close to each other. Thus, the models with minimum GCV score are generally have good prediction accuracy. The squared prediction errors are around 0.5 - 1.4  $TECU^2$ . When Fig 5.14 is compared to Fig. 5.12, it can be observed that both CV and GCV curves are correlated. This is an expected result since the GCV and CV are dependent on the squared error loss.

As in the case of numerical comparison, no clear judgement can be made on the choice of best B-spline order to use in BMARS algorithm. The order 2 B-spline results (middle sub-figure with blue lines) seems to follow the GCV curve best, which may be an indicator of better modeling. A large variance is observed at 14:00 UT on the 10th of March, which is caused by errors slightly higher than 1 TECU. These results indicate that Semi-parametric VTEC models estimated by BMARS have an EPE close to the GCV scores of the models. In the case of three days, the EPE is around 1  $TECU^2$ .

#### 5.2.4.2 Point Positioning Results

Probably the best method to validate a VTEC model is to use the VTEC maps to predict the ionospheric delays for receivers that are not used in model building. Although, it seems to be a simple procedure, it becomes complicated to find a reference ground truth for the ionospheric delays. For this reason, this study uses the estimated VTEC maps to obtain static positions of reference ground stations that are not used in model

building. And compare the position estimates to the true positions of the reference stations. The position estimates are further compared to the estimates based on the ionospheric corrections calculated by CODE GIMs for ionospheric corrections. The reference stations with their precise positions are listed in Table 5.6. The approximate positions for the receivers can be found in the header of the corresponding RINEX file. The precise positions listed here are calculated through the Automatic Precise Point Positioning Service of JPL (<http://apps.gdgps.net/>). The RINEX observation files are uploaded to the website and the corresponding precise positioning estimates are delivered by the APPS. These are then assumed to be the true positions for each station. Note that, the stations GRAS, MEDI, ONSA, POTS and ZIM2 are also used by CODE in the estimation process of GIMs, while none of the stations are included in the semi-parametric modeling with BMARS.

Table 5.6: Reference stations for point positioning with ECEF positions obtained through JPL APPS service

Station	X (m)	Y (m)	Z (m)
CPAR	3949918.6489 ± 0.0015	1116467.3866 ± 0.0012	4865832.8034 ± 0.0015
GRAS	4581690.7964 ± 0.0016	556114.9706 ± 0.0012	4389360.8705 ± 0.0013
MEDI	4461400.6046 ± 0.0021	919593.7102 ± 0.0015	4449504.8388 ± 0.0018
ONSA	3370658.4456 ± 0.0013	711877.2425 ± 0.0012	5349787.0239 ± 0.0017
POTS	3800689.5067 ± 0.0016	882077.5016 ± 0.0013	5028791.3718 ± 0.0016
SMID	3557911.1120 ± 0.0013	599176.7887 ± 0.0012	5242066.5022 ± 0.0016
UNTR	4590764.3439 ± 0.0021	1032366.9910 ± 0.0016	4291666.5717 ± 0.0018
ZADA	4425736.7277 ± 0.0015	1204734.8920 ± 0.0012	4417173.7701 ± 0.0013
ZIM2	4331299.7754 ± 0.0016	567537.4508 ± 0.0012	4633133.8058 ± 0.0014

High accuracy point positioning is a complicated process where many systematic biases must be corrected by appropriate methods to obtain a good estimate. Regarding to the comparison of two different ionosphere model, one must consider that all these bias corrections and the estimation method must be the same for both models. The positioning results shown here are obtained by combining the observation equations related to code pseudo-ranges and carrier phases defined in Eq. 3.12 and 3.15 at each epoch for the selected hours described in the previous sections. The same ambiguity parameter is used for continuous arcs which may span several epochs. The wet zenith delay is also assumed to be an unknown parameter at each epoch. The combined observation equation can be written as :

$$\Delta \mathbf{y} = \mathbf{X}|_{r=r_0} \Delta \boldsymbol{\beta} + \mathbf{e}, \quad (5.4)$$

where, the first three columns of  $\mathbf{X}|_{r=r_0}$  contains the partial derivatives of the geometric range evaluated at the approximate receiver position  $r_0$ , which is taken as the approximate position in RINEX file. The upper part of the stacked measurement vector  $\Delta \mathbf{y}$  consists of the observed minus modeled carrier phase measurements on L1

frequency. The lower part includes the observed minus modeled code pseudo-range measurements C1. Assuming a Gauss-Markoff model, the measurements have the following statistical properties:

$$\begin{aligned} D(\Delta\mathbf{y}) &= D(\mathbf{e}) = \sigma_0^2 \mathbf{P}^{-1}, \\ E\{\mathbf{e}\} &= 0, \end{aligned} \tag{5.5}$$

where the  $\sigma_0^2$  is the variance of unit weight and  $\mathbf{P}$  is the positive definite weight matrix of observations. Since we combine carrier phase and code measurements appropriate weighting must be established. A simple weighting strategy can be to apply a weighting factor of  $10^4$  to the carrier phases assuming  $\frac{\sigma_c^2}{\sigma_p^2} = 10^4$ , where  $\sigma_p$  is the noise level of carrier phases,  $\sigma_c$  is the noise level of code pseudo-ranges (Dach et al., 2007). Assuming that the observations are statistically independent of each other (uncorrelated), the contents of the weight matrix can be written as a block matrix of the form:

$$\mathbf{P} = \begin{bmatrix} \mathbf{P}_{L1} & 0 \\ 0 & \mathbf{P}_{C1} \end{bmatrix}, \tag{5.6}$$

where,  $\mathbf{P}_{L1} = 10^4 \mathbf{I}$  is the diagonal weight matrix of carrier phases and  $\mathbf{P}_{C1} = \mathbf{I}$  is the diagonal weight matrix of code pseudo-ranges. Then, the weighted least squares estimate can be obtained as described in Chapter 4 as :

$$\widehat{\Delta\boldsymbol{\beta}} = (\mathbf{X}^T \mathbf{P} \mathbf{X})^{-1} \mathbf{X}^T \mathbf{P} \Delta\mathbf{y}, \tag{5.7}$$

the first three components of the estimated parameters  $\widehat{\Delta\boldsymbol{\beta}}$  are corrections to be brought to the approximate position  $\mathbf{r}_0$ . Thus, the estimated position of the station can be calculated as:

$$\widehat{\mathbf{r}} = \mathbf{r}_0 + \begin{bmatrix} \widehat{\Delta\beta}_0 \\ \widehat{\Delta\beta}_1 \\ \widehat{\Delta\beta}_2 \end{bmatrix}, \tag{5.8}$$

where,  $\widehat{\mathbf{r}}$  is the estimated position of the ground station,  $\widehat{\Delta\beta}_0$  is the correction on the X axis,  $\widehat{\Delta\beta}_1$  is the correction on the Y axis and  $\widehat{\Delta\beta}_2$  is the correction on the Z axis in meters.

The following corrections are applied to the observations to account for systematic biases using the GPStk software.

- P1-P2 and P1-C1 DCB biases of satellites: The code pseudo-ranges are corrected by the Differential Code Biases (DCB) of satellites obtained from CODE. The

receiver DCB is not corrected since it is treated in the receiver clock parameter.

- Tropospheric delays: The troposphere model used is the Neil troposphere model which is initialized with standard weather parameters such as: 20 degrees Celsius temperature, 1013 mb pressure, 50 % of relative humidity and the day of year. The latitude and longitude of receiver obtained from approximate position is used.
- Ionospheric delays: The satellite to receiver ray paths are established with the approximate receiver position and satellite position calculated from precise ephemeris published by IGS. The Single Layer Model with an ionospheric height of 450 km. is used to obtain the ionospheric pierce point coordinates. For the case of CODE GIMs the IONEX files published by CODE are downloaded from Internet as described in the previous section related to data preparation. For the BMARS models, IONEX files are generated by applying a grid of 0.5x0.5 degrees in longitude and latitude. This finer grid is established to account for the local variations delivered by BMARS models. The VTEC values related to the IPP location at each epoch are calculated. Then, the VTEC values are converted to range delays by applying the mapping function as described in Chapter 3.
- Other corrections related to gravitational delay, phase windup, satellite antenna phase center variations, solid Earth tides and relativistic effects are also applied.

A filtering of observations has been applied to exclude the satellites with elevation angle less than 15. The satellites with IPPs that are outside the modeling region are also filtered in both models. Since the approximate position of the station is the same for both CODE GIM and BMARS models, the resulting corrections except the ionosphere related corrections are the same. Thus, the resulting position estimates are only depend on the ionospheric variations between the CODE GIMs and BMARS models. Table 5.7, 5.8 and 5.9 lists the differences of position estimates from CODE GIMs and BMARS models to the true positions given in Table 5.6. The differences are given for each component  $X, Y$  and  $Z$  as  $\Delta X, \Delta Y$  and  $\Delta Z$  respectively. The last column is the 3D Euclidean distance of the estimated position to the true position.

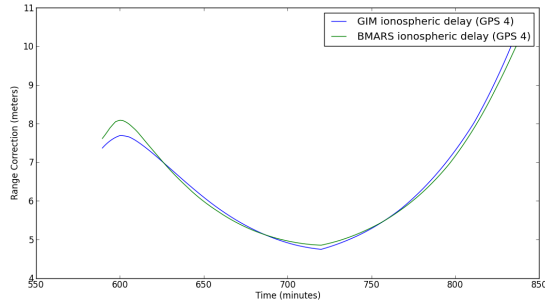
Table 5.7 lists the positioning results on the 8th of March 2012. According to the table, for all stations, the 3D distance values of BMARS based positions are lower than the CODE GIM based ones. The lower the value of 3D distance, the closer the position approximation is to the true position. Thus, the results indicate an improvement in terms of positioning over the CODE GIMs. The distance differences can reach up to 7 dm for some stations (see positioning results for ZADA station). According to the difference VTEC maps on the same day (see Fig. 5.6), the differences between GIM and BMARS models are visible especially on the upper left and lower right parts of the maps. The SMID and ONSA stations are located on the top of the modeling region whereas the ZADA station is located close to the lower right of the modeling

region. The positioning differences for SMID and ONSA stations are in the range of 1-3 dm whereas the differences in the ZADA station are about 7 dm. Note that, the actual results depend barely on the distribution of the IPPs which may be distributed as shown in Fig. 5.2. The low accuracy in GRAS station needs further investigation since it is higher in both BMARS and Code GIM models which may be a result of not choosing appropriate weighting of the observations or other unmodeled error sources.

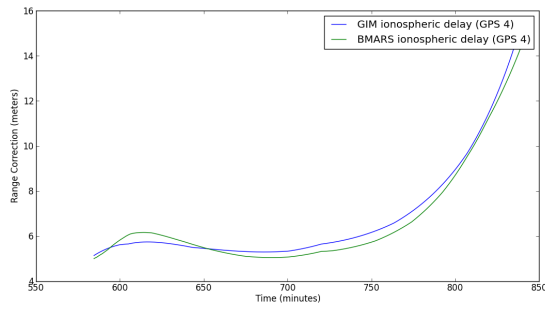
The positioning results on the 9th of March are listed in Table 5.8. These are of particular importance since there is a geomagnetic storm on that day giving rise to the VTEC levels as shown in Fig. 5.4. The difference VTEC maps given in Fig. 5.7 indicate large variations especially at the lower right part of the modeling region. The position estimates of the ZADA station based on BMARS models gives around 3 dm better results than GIMs. Even better results are achieved for MEDI and ZIM2 stations where the position estimates are close to the true positions around 2 dm level. The differences with CODE GIMs for these stations range from 3 to 6 dm. Another interesting result is that the maximum difference in positioning estimates is observed for the SMID station reaching up to 8 dm which may be caused by IPPs covering both positive deviations on the upper left part and negative deviations at the center of the difference maps. Note that, all the positioning estimates for BMARS give better or close results to CODE GIMs.

Table 5.9, on the other hand, lists the positioning results on day 10th of March (UNTR station is not listed, since observations are not available on this day). As can be seen from the 3D distances, both BMARS and CODE GIMs deliver sub-meter accuracies (except the CODE GIM for ZADA station which is very close to 1 meter), which may be attributed to the lower variations as can be seen from Table 5.4 particularly for 12:00 UT. Except for the SMID and POTS stations, the BMARS models again deliver better positioning accuracies. For these stations, CODE GIMs and BMARS models provide similar positioning estimates with differences in cm level. The maximum difference is achieved for the MEDI station which amounts to approximately 5 dm. The MEDI station is located at the lower central part of the modeling region, where the IPPS covers both positive and negative deviations in the difference VTEC maps. For example, Fig. 5.15 displays the range corrections calculated from CODE GIMs (blue) and BMARS with order 2 B-splines (green). The positive and negative variations can be observed in the corresponding figure.

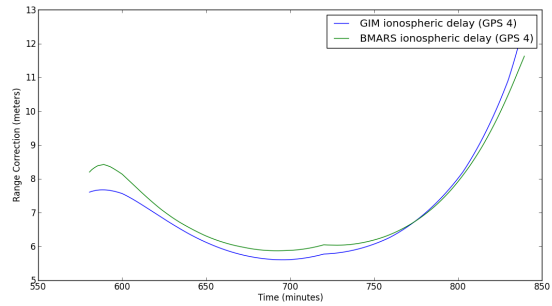
In view of the results shown in the tables, the semi-parametric modeling with BMARS provides effective and accurate models for regional applications that need ionospheric corrections. The positioning algorithm used in this study is only for validation and comparison of the VTEC models. More accurate position estimates can be achieved for both CODE GIMs and BMARS models if a Precise Point Positioning concept is applied in single frequency. Finer results can be obtained using appropriate methods for ambiguity resolution. The following section provides a brief discussion about the potential uses of the BMARS models. The limitations and extension points are also



(a) 8th of March 2012



(b) 9th of March 2012



(c) 10th of March 2012

Figure 5.15: Ionospheric range delays calculated by CODE GIMs and BMARS  $d=2$  on each day between the MEDI station and GPS satellite with PRN=4

listed.

### 5.2.5 Discussions

All the comparisons and validation tests given in previous chapters indicate that semi-parametric modeling with BMARS delivers effective and accurate regional VTEC models which can be used for ionospheric delay corrections. As a regional model, the main problem of the algorithm is the limited spatial coverage, which may result in exclusion of some satellites having IPPs out of the region. To overcome this problem, a reference background VTEC model can be used. In this case BMARS can be configured to model the VTEC deviations from the reference model inside the region. For the IPPs outside the region, one makes use of the reference VTEC model leading to better positioning accuracies. CODE GIMs can also be selected as the reference model where the BMARS will strengthen the accuracy of the global representation regionally. Another alternative is the IRI model, which is widely used as a background model in many studies mentioned before. A combination of regional BMARS models with CODE GIMs and IRI can also deliver promising results.

As stated before, knot-optimization is an important feature to make the BMARS results more robust. The knot-optimization is not currently implemented inside the algorithm. Without it one can consider limiting the level of B-splines of the BMARS models depending on the data distribution at hand. The regional 3D B-splines method is also affected by the misuse of the B-spline level. If the level is increased too much, then there will be less measurements to support individual B-spline coefficients. BMARS, on the other hand, starts with the lowest level corresponding to the largest scale. Thus, for small number of terms, and limited scale, BMARS can deliver usable results without the need for knot-optimization.

As a non-parametric method, BMARS searches for best basis functions that fit to the observations. Although, the search space is smaller than the MARS algorithm, as the level is increased it grows rapidly. Moreover, unlike MARS algorithm, there is no fast updating method to solve for consecutive knot locations. The forward stage is based on the Gram-Schmidt orthonormalization which requires many inner products to be computed. A strategy is developed by (Bakin et al., 2000) which computes the inner products in parallel. However, another time-consuming operation is the evaluation of B-splines at each IPP. As the order of the B-splines increased the time required to evaluate the B-splines increases too. Thus, for rapid applications, BMARS with order 1 B-splines is recommended. Additionally, the parallelization strategy mentioned above and the evaluation of B-splines can all be implemented in OpenCL (Open Computing Language) to improve the model building speed.

A possible use of the developed technique is to apply the algorithm to produce rapid ionospheric products from a Continuously Operating Reference Station (CORS). These

Table 5.7: Single-Frequency static point positioning results for day 8 March 2012

Station	Method	$\Delta X$ (m)	$\Delta Y$ (m)	$\Delta Z$ (m)	$\Delta$ 3D
CPAR	CODE GIM	-0.573276	-0.471509	-0.162864	0.759928
	BMARS d=1	0.031913	-0.164113	0.069577	0.181087
	BMARS d=2	-0.097827	-0.232911	-0.053363	0.258196
	BMARS d=3	-0.124829	-0.245214	-0.168301	0.322548
GRAS	CODE GIM	1.045212	-0.344914	0.929666	1.440733
	BMARS d=1	1.015168	-0.287510	0.654286	1.241499
	BMARS d=2	0.941161	-0.268684	0.634176	1.166256
	BMARS d=3	0.992109	-0.218771	0.655351	1.208978
MEDI	CODE GIM	0.484743	-0.232509	0.913491	1.059954
	BMARS d=1	0.165380	-0.224577	0.167658	0.325414
	BMARS d=2	0.288539	-0.155610	0.240517	0.406592
	BMARS d=3	0.313224	-0.151944	0.275890	0.444198
ONSA	CODE GIM	-0.666072	-0.285435	-0.857149	1.122421
	BMARS d=1	-0.462542	-0.147781	-0.688425	0.842444
	BMARS d=2	-0.539456	-0.195883	-0.788457	0.975217
	BMARS d=3	-0.425774	-0.145593	-0.688225	0.822274
POTS	CODE GIM	-0.376179	-0.343129	-0.020164	0.509563
	BMARS d=1	0.233417	-0.080463	0.319913	0.404107
	BMARS d=2	0.178128	-0.112891	0.275220	0.346727
	BMARS d=3	0.198718	-0.103600	0.279533	0.358274
SMID	CODE GIM	-0.563551	-0.339752	-0.351952	0.746251
	BMARS d=1	-0.405192	-0.221197	-0.392598	0.606005
	BMARS d=2	-0.451710	-0.229476	-0.519638	0.725758
	BMARS d=3	-0.377285	-0.198112	-0.360665	0.558275
UNTR	CODE GIM	1.002606	-0.216878	0.971225	1.412633
	BMARS d=1	0.749148	-0.204400	0.289832	0.828858
	BMARS d=2	0.960442	-0.098507	0.486024	1.080912
	BMARS d=3	0.870977	-0.108297	0.391056	0.960861
ZADA	CODE GIM	0.744890	-0.184447	1.160563	1.391326
	BMARS d=1	0.485317	-0.178455	0.325169	0.610830
	BMARS d=2	0.622411	-0.127984	0.452526	0.780099
	BMARS d=3	0.574729	-0.145457	0.441198	0.739004
ZIM2	CODE GIM	0.309865	-0.316537	0.650771	0.787220
	BMARS d=1	0.441933	-0.249920	0.414365	0.655335
	BMARS d=2	0.520276	-0.212009	0.495447	0.749068
	BMARS d=3	0.443142	-0.220035	0.436144	0.659554

Table 5.8: Single-Frequency static point positioning results for day 9 March 2012

Station	Method	$\Delta X$ (m)	$\Delta Y$ (m)	$\Delta Z$ (m)	$\Delta$ 3D
CPAR	CODE GIM	-0.933485	-0.510649	-0.641223	1.242306
	BMARS d=1	-0.631605	-0.335319	-0.590915	0.927655
	BMARS d=2	-0.482416	-0.309018	-0.439626	0.722141
	BMARS d=3	-0.542688	-0.318422	-0.532490	0.824286
GRAS	CODE GIM	0.154701	-0.319710	-0.096076	0.367937
	BMARS d=1	0.270437	-0.279601	-0.028200	0.390010
	BMARS d=2	0.307875	-0.183568	0.006012	0.358497
	BMARS d=3	0.222258	-0.200852	-0.078574	0.309699
MEDI	CODE GIM	-0.303024	-0.258131	0.313432	0.506651
	BMARS d=1	-0.144068	-0.173233	-0.133993	0.262144
	BMARS d=2	0.026462	-0.163264	0.030920	0.168260
	BMARS d=3	0.066293	-0.148539	0.099228	0.190538
ONSA	CODE GIM	0.005202	0.010568	-1.359363	1.359414
	BMARS d=1	-0.442366	-0.096860	-0.824999	0.941113
	BMARS d=2	-0.429725	-0.053613	-0.691647	0.816035
	BMARS d=3	-0.410490	-0.056354	-0.704099	0.816966
POTS	CODE GIM	-0.382742	-0.351771	-0.786452	0.942731
	BMARS d=1	-0.226020	-0.283447	-0.365437	0.514753
	BMARS d=2	-0.230211	-0.270001	-0.442903	0.567504
	BMARS d=3	-0.192926	-0.268126	-0.394888	0.514828
SMID	CODE GIM	-0.099388	-0.156043	-1.368588	1.381036
	BMARS d=1	-0.222991	-0.184567	-0.479744	0.560307
	BMARS d=2	-0.218886	-0.153208	-0.487712	0.556100
	BMARS d=3	-0.221648	-0.157649	-0.481688	0.553177
UNTR	CODE GIM	0.621607	-0.114362	0.502285	0.807319
	BMARS d=1	0.577034	-0.090601	0.238505	0.630921
	BMARS d=2	0.572218	-0.118480	0.205999	0.619602
	BMARS d=3	0.585296	-0.123246	0.322227	0.679405
ZADA	CODE GIM	0.008585	-0.301303	0.682780	0.746355
	BMARS d=1	0.285702	-0.188818	0.281918	0.443572
	BMARS d=2	0.200794	-0.240312	0.197719	0.370352
	BMARS d=3	0.229135	-0.232729	0.271933	0.424986
ZIM2	CODE GIM	-0.743692	-0.350603	0.045114	0.823429
	BMARS d=1	-0.202908	-0.197740	-0.005519	0.283378
	BMARS d=2	-0.165892	-0.172958	-0.015150	0.240134
	BMARS d=3	-0.185685	-0.171256	-0.033408	0.254801

Table 5.9: Single-Frequency static point positioning results for day 10 March 2012

Station	Method	$\Delta X$ (m)	$\Delta Y$ (m)	$\Delta Z$ (m)	$\Delta$ 3D
CPAR	CODE GIM	-0.362436	-0.577582	-0.145893	0.697314
	BMARS d=1	-0.071758	-0.359488	-0.142592	0.393336
	BMARS d=2	-0.160903	-0.379775	-0.230312	0.472401
	BMARS d=3	-0.174663	-0.367752	-0.243615	0.474444
GRAS	CODE GIM	0.448406	-0.356952	0.520295	0.774073
	BMARS d=1	0.289591	-0.236600	0.188312	0.418693
	BMARS d=2	0.254859	-0.222465	0.155173	0.372186
	BMARS d=3	0.219637	-0.214622	0.119243	0.329426
MEDI	CODE GIM	0.283608	-0.404598	0.670547	0.832927
	BMARS d=1	0.065795	-0.257325	0.058216	0.271908
	BMARS d=2	0.168621	-0.241116	0.211403	0.362300
	BMARS d=3	0.186402	-0.232387	0.259248	0.394917
ONSA	CODE GIM	-0.249661	-0.334445	-0.565555	0.702877
	BMARS d=1	-0.014179	-0.129856	-0.232961	0.267085
	BMARS d=2	-0.011337	-0.098496	-0.232120	0.252408
	BMARS d=3	0.086941	-0.077338	-0.122459	0.168926
POTS	CODE GIM	-0.083675	-0.458613	0.182214	0.500529
	BMARS d=1	0.190342	-0.261577	0.302404	0.442833
	BMARS d=2	0.245200	-0.233712	0.377492	0.507193
	BMARS d=3	0.198380	-0.245135	0.336182	0.460938
SMID	CODE GIM	-0.020958	-0.433230	0.077756	0.440651
	BMARS d=1	0.248152	-0.230829	0.349386	0.486757
	BMARS d=2	0.157592	-0.216525	0.173476	0.319080
	BMARS d=3	0.243532	-0.218394	0.320402	0.457888
ZADA	CODE GIM	0.475726	-0.441111	0.767449	1.004924
	BMARS d=1	0.650506	-0.178256	0.490561	0.834016
	BMARS d=2	0.442244	-0.219164	0.365136	0.613951
	BMARS d=3	0.466597	-0.201529	0.373232	0.630578
ZIM2	CODE GIM	0.125450	-0.349619	0.168695	0.407957
	BMARS d=1	0.155287	-0.231826	-0.034619	0.281169
	BMARS d=2	0.170363	-0.212883	0.046076	0.276524
	BMARS d=3	0.165994	-0.228470	-0.006278	0.282475

products can be downloaded by single-frequency receivers to correct their measurements. The downloaded ionosphere model can be updated with a new one after a predefined period. The period must be established so that the VTEC model is accurate enough until the next update and the the ionospheric measurements are dense enough to support VTEC models with acceptable accuracy. The semi-parametric BMARS model can also be used for local applications to obtain receiver DCBs and local ionosphere models.

## CHAPTER 6

### THE SOFTWARE

During the course of this study various scripting and programming languages are used to develop software utilities and packages. Since the MARS algorithm implementations are already available from the R programming language, it is not developed from scratch but R scripting language is used to wrap the implementations to use the VTEC measurement. Unfortunately, a BMARS implementation was not available. Hence, BMARS is implemented in MATLAB by the author. Due to the limitations of the MATLAB language and its licensing issues, the semi-parametric modeling with BMARS is implemented in Python programming language. This Chapter provides a summary of the development environment, the tools used and the design of the software package.

#### 6.1 Software Development Environment

A software development environment is a crucial part of designing and coding of any piece of software. For this reason generally an integrated development environment is setup by prior to any development activity. Fortunately, there are many software tools freely available that can be easily setup and integrated. The development of the software package and utilities in this study and even the writing of the manuscript is performed on the Eclipse Integrated Development Environment (IDE). Although matured as a Java development environment, Eclipse provides many addons and plug-ins to support a wide variety of programming languages and use-cases. The Eclipse IDE and related plug-ins can be downloaded from <http://www.eclipse.org/>. All of the software development is performed on OSX Mountain Lion operating system with GNU compiler suite. The following Eclipse plug-ins are used during the study.

- EGit: Eclipse git plug-in provides an easy to use yet powerful Graphical User Interface (GUI) for the git version control utility.
- PyDev Plug-in: Provides code completion, syntax highlighting, unit testing and debugging of Python programs.

- Texclipse plug-in: The integrated environment for Latex editor with preview capabilities.
- CDT Plug-in: Provides an IDE for C and C++ code editing, syntax highlighting, code completion and debugging.
- Papyrus Plug-in: Provides UML based modeling of software packages. The diagrams in this chapter are drawn by Papyrus.

The following subsections provide additional information related to external software libraries used during the study.

### 6.1.1 Python Development Environment

The semi-parametric modeling described in Chapter 4 is implemented in Python programming language (<http://www.python.org/>). The Python programming language is open-source and freely available from the website for various operating systems including UNIX, LINUX and MS Windows. Most UNIX based operating systems are shipped with a version of Python. The Python version 2.7.3 is used throughout the thesis. Python is a flexible Object Oriented (OO) language where it can be used from writing small scripts for text processing to number-crunching scientific studies and even game programming.

Eclipse PyDEV IDE for Python which is used in this thesis can be downloaded from <http://pydev.org/>. In addition to the IDE, many Python packages are used in this study which can be listed as:

- Numpy: Numpy is, as its name suggests, a numerical computation package available for Python. It provides MATLAB like syntax for array manipulations. The FORTRAN codes and C or C++ codes can easily be integrated to Numpy to provide even faster execution speed. Many useful linear algebra routines and other frequently used tools such as Fourier Transform are readily available. Numpy can be downloaded from <http://www.numpy.org/>
- Scipy delivers additional scientific tools such as signal processing, optimization and statistics. Additionally, it provides loading of MATLAB .mat files which is used to load TECMapper converted observations into Python environment. Its is highly coupled with Numpy and can be downloaded from <http://www.scipy.org/>.
- Matplotlib adds 2D and 3D plotting features to the Python environment. The plots used in this study are generated with Matplotlib. Basemap is an addon module to Matplotlib, which provides mapping functionality. The VTEC maps

and IPP coverage figures in Chapter 5 are generated with Basemap and Matplotlib. Matplotlib can be downloaded from <http://matplotlib.org/>.

- PyEarth is a port of the MARS implementation in Earth package from R programming language. It is used as the MARS implementation in the software and the BMARS algorithm is implemented as an extension to the MARS implementation by rewriting the forward stage implementation. PyEarth is available from <https://github.com/jcrudy/py-earth>.
- Cython provides an easy to use interface for writing native code in C or C++ programming language by allowing a python like syntax. It is actually a python to C/C++ compiler which makes it possible to write python modules that need native speed for computational problems. The B-spline evaluations in this study are optimized with the use Cython.

### 6.1.2 Development with GPSTk

The GPSTk is an open-source library sponsored by the Applied Research Laboratories at the University of Texas Austin (Tolman et al., 2004). It provides a comprehensive suite of GNSS related methods and classes written in C++ programming language following a clear OO concept. It provides classes for file handling for various standard exchange formats including RINEX (v2-3), IONEX, SP3, RINEX Nav, DCB, ANTEX, among others. Calculation routines related to time, position interpolation and transformation and many others are included. It also provides positioning and atmospheric correction models as well as Cycle slip handling. A package inside GPSTk called proframe which provides classes to generate processing chains for easy GNSS data handling. Mainly the classes in the processing chain are used in the thesis to model the observation equations, calculate the corrections for systematic biases and generate simple position estimates. The software can be downloaded from <http://www.gpstk.org/> either in source form or in binary form for various operating systems.

### 6.1.3 TECMapper

TECMapper is a MATLAB based implementation of GPS data processing software to generate regional models based on 2D or 3D tensor product of univariate B-splines as well as 2D Spherical Harmonic expansions (Nohutcu, 2009). It reads RINEX files of individual ground stations and calculates the satellite DCB eliminated observations by utilizing the precise orbit files and DCB estimations downloaded from Internet as described in Chapter 5. The software is used to model ground-based GPS observations as described in Chapter 4. The output of the software is MATLAB .mat formatted files with tec extension. These files are then used by the developed software package

to build BMARS VTEC models.

## 6.2 Software Design

As stated in the objectives of the study, the software package should be developed in an extensible way. For this reason we apply OO concepts. The previous section gave a summary of software libraries reused in the software package. Fig 6.1, on the other hand, gives the arrangement of the modules with the software libraries. As can be seen from the figure, the Python Execution Environment and GPSTk provides the base for the modules. Cython with the Numpy, Scipy, Matplotlib stack provides a base for the implementation of both PyEARTH and BMARS. On the other hand, GPSTk library provides the building blocks for utilities and positioning module.

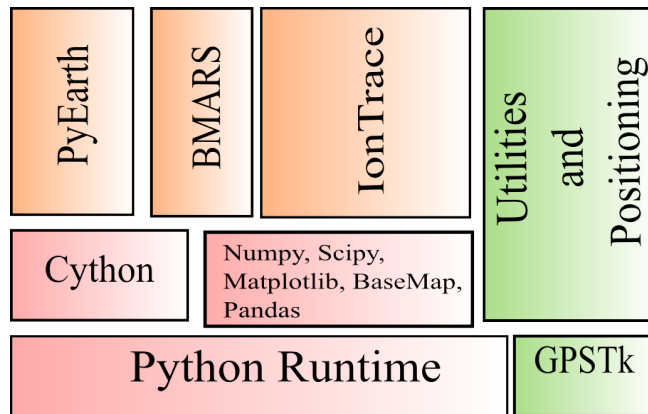


Figure 6.1: Software block diagram

BMARS module is mainly implemented in Cython language especially the B-spline evaluation class. The classes and interfaces in BMARS, IonTrace and Positioning are listed in the following subsections starting with the interfaces.

### 6.2.1 Interfaces

To meet the goals of extensibility, this study provides a set of interfaces for common ionosphere modeling implementations. The interfaces provided are simple and easy to be realized. Fig. 6.2 displays the UML class diagram of interfaces with the provided functionality and associations.

The interfaces and description of delivered functionality are summarized below:

- **ModelBounds:** defines a spatio-temporal box for regional VTEC models. And also provides a grid over the modeling region at a specified time.

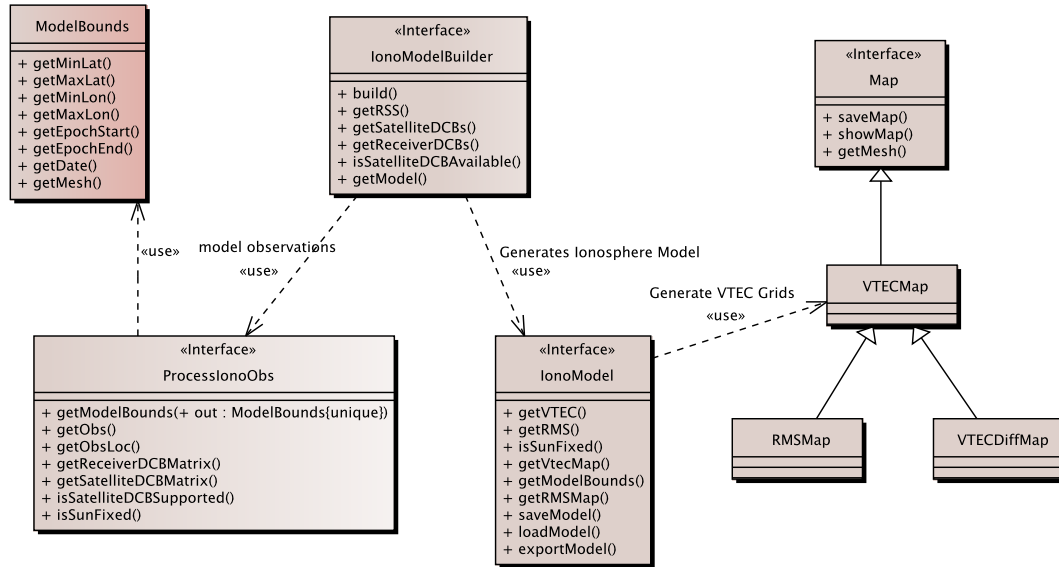


Figure 6.2: Basic interfaces for Ionosphere modeling

- **getMinLat()**: Returns the minimum latitude of the modeling region.
  - **getMaxLat()**: Returns the maximum latitude of the modeling region.
  - **getMinLon()**: Returns the minimum Longitude of the modeling region.
  - **getMaxLon()**: Return the maximum longitude of the modeling region.
  - **getEpochStart()**: The start time for VTEC model available over the modeling region.
  - **getEpochEnd()**: The end time for VTEC model available for modeling region.
  - **getDate()**: The date of the VTEC model.
  - **getMesh()**: The grid points over the modeling region with specified grid intervals on longitude and latitude. Mainly used for evaluating a VTEC Model over a grid to produce maps or export as IONEX.
- **ProcessIonoObs** defines an interface for various data processing schemes to obtain VTEC models. This interface encapsulates the details of data pre-processing to the model builders or users. It provides basic functionality related to getting observations, observation locations (knot-locations) and receiver DCB matrix which mainly contains the coefficient matrix for receiver DCBs (see Chapter 4; Eq. 4.9). The functionality is explained below:
    - **getModelBounds()**: Returns the spatial and temporal bounding box for the observations.
    - **getObs()**: returns the stacked observation vector given in Eq. (4.6).

- **getObsLoc()**: return the matrix whose columns are the knot-locations associated to observations (see the definition of knot-locations  $\mathbf{x}_k$  in 4.6).
  - **getReceiverDCBMatrix()**: Returns the matrix  $\mathbf{G}$  in Eq. (4.9).
  - **getSatelliteDCBMatrix()**: Returns the matrix associated to the satellite DCB coefficients. Currently not implemented.
  - **isSatelliteDCBSupported()**: Currently always return false.
  - **isSunFixed()**: Returns if the observation modeling especially the observation locations are in Sun-fixed reference frame or not.
- **IonoModelBuilder**: This interface provides an easy to implement and extend interface for all model builders for ionosphere. The class which extends this interface probably should also extend the IonoModel interface described below. The functionality provided by the interface is defined as:
    - **build()**: Given the modeled observations as defined by the interface ProcessIonoObs, build a functional model for the VTEC estimating the receiver DCBs at the same time.
    - **getRSS()**: Return the Residual Sum of Squares for the generated model.
    - **getSatelliteDCBs()**: Currently not implemented.
    - **getReceiverDCBs()**: Returns the map of receiver DCBs with the key of four character receiver marker.
    - **isSatelliteDCBAvailable()**: Currently returns false
    - **getModel()**: Returns the generated VTEC model.
  - **IonoModel**: provides an extensible interface for various VTEC models available. The model generally contains the estimated coefficients of the VTEC model as given in the parameter vector  $\mathbf{a}$  in Section 4.5. The estimated coefficients are then used to find VTEC values for given ionospheric pierce points at given time. Also the model can be exported to IONEX format.
    - **getVTEC()**: return VTEC value at a given geographic latitude, longitude and time.
    - **getRMS()**: return an estimation of error at given geographic latitude, longitude and time.
    - **isSunFixed()**: returns if the model support sun-fixed reference frame.
    - **getVTECMap()**: return the VTECMap instance for a given time and grid resolution.
    - **getModelBounds()**: returns the bounds for the VTEC model.
    - **getRMSMap()**: returns an error map (RMSMap instance) for a given time and grid resolution.
    - **saveModel()**: saves the model to a file

- **loadModel():** loads the model from a file
- **exportModel():** exports instances of VTEC maps to RINEX file, with given grid resolution and times.
- **Map:** Provides a base interface for various gridded maps. Also a basic functionality of setting up mapping window is provided. The functionality is listed below:
  - **saveMap():** saves the map in a file supported by Matplotlib.
  - **showMap():** shows the map in a new Matplotlib figure.
  - **getMesh():** returns the underlying grid mesh for this map.
- **VTECMap:** Extends the Map interface and provides a generic class for various gridded VTEC map instances.
- **RMSMap:** Extends the VTECMap class for providing estimated VTEC errors.
- **VTECDiffMap:** Extends the VTECMap class and delivers a difference map between two VTECMap instances. The difference figures in Chapter 5 are generated by this instance.

## 6.2.2 Software Modules

The interfaces described in the previous section are implemented by the classes in the modules described in this section. Although all the modules described below are implemented during the study, the BMARS algorithm and positioning are designed to be independent modules from the IonTrace module. The main reason for this separation is that the BMARS algorithm can be reused elsewhere, which is not relevant to ionosphere at all. Similarly, the positioning module can be reused in different settings also. Hence, for the sake of modularity, these modules are separated from IonTrace, which implements the interfaces defined above encapsulating the underlying algorithmic details related to BMARS and gives a clean interface for the developers.

### 6.2.2.1 BMARS

This module contains the implementation of BMARS algorithm which is described in detail in Chapter 4. The BMARS algorithm is implemented to be generic enough to be applied to different non-parametric modeling needs other than the VTEC modeling. The semi-parametric modeling is also implemented in a generic way to be applied to different scientific problems. The module does not have any dependency to the other modules which increases its reusability. Fig. 6.3 presents the classes inside the module with their relation to the PyEarth package mentioned above.

The classes and their functionality are described below:

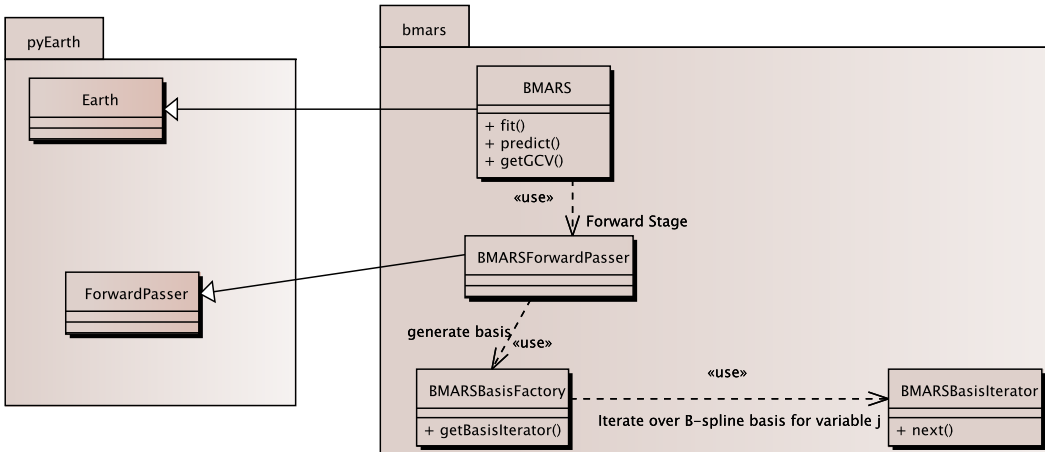


Figure 6.3: BMARS Module Class Diagram

- **pyEarth.ForwardPasser:** is responsible for the forward stage of MARS algorithm. The pyEarth package is a python port of the Earth package in R programming language. The class iteratively adds new piecewise-linear reflected pairs as describes in the Chapter 4 while monitoring a stopping condition. The pyEarth package is implemented by Jason Rudy and can be downloaded from the site provided in the previous sections.
- **pyEarth.Earth:** The Earth class provides a wrapper for the forward and backward stages in pyEarth which arranges the inputs for the fitting process and provides and interface for querying predictions from the estimated model.
- **bmars.BMARS:** The BMARS class extends from the Earth class in pyEarth and adds BMARS specific initialization code as well as semi-parametric modeling constructs. It adds a new prediction function for the non-parametric part to make it possible for VTEC function evaluations. Additionally, new parameters are added to BMARS class to support the extensions described in Chapter 4. For example a new parameter is added to support to fix the modeling region, a new stopping criteria is added (minimum MSE to be achieved in forward stage), a new flag for the use inner product cache, initial level to start and maximum level to stop the forward stage are added. The basic functionality provided by BMARS is given as:
  - **fit():** Fits the non-parametric or semi-parametric model to the observations given.
  - **predict():** use the estimated non-parametric or semi-parametric model to predict values for given location.
  - **getGCV():** return the GCV score.
  - **getNumberOfSelectedTerms():** returns the number of selected terms.

- **bmars.BMARSForwardPasser:** is an extension of pyEarth.ForwardPasser which is written from scratch. The algorithm utilizes the BMARSBasisFactory and BMARSBasisIterator to generate candidate BMARS basis functions and then use the Gram-Schmidt orthonormalization to choose the best fitting one. The simplified version of carried steps is given in Algorithm 3.
- **bmars.BMARSBasisFactory:** The BMARS basis factory BMARSBasisIterator instances for the given parent bases, level and scale in order to support BMARSForwardPasser to find the best fitting candidate. The forming of candidate basis functions are given in Line 13 of Algorithm 3.
- **bmars.BMARSBasisIterator:** As stated above, BMARSBasisIterator simplifies the inner loops in Line 9 and 11 of Algorithm 3. At each iteration it returns a new candidate basis function to the BMARSForwardPasser for the evaluation of Residual Sum of Squares. The BMARSBasisIterator and BMARSBasisFactory provide an additional extension point for BMARS where developers can introduce iterators for other basis function to be fit in BMARS fashion.

### 6.2.2.2 IonTrace

This section gives the classes that wrap the BMARS algorithm and implements the interfaces given in previous sections. Only semi-parametric VTEC modeling related classes are listed here. Other implementations of the interfaces for 3D B-splines, Spherical Harmonics are not listed since they are under development.

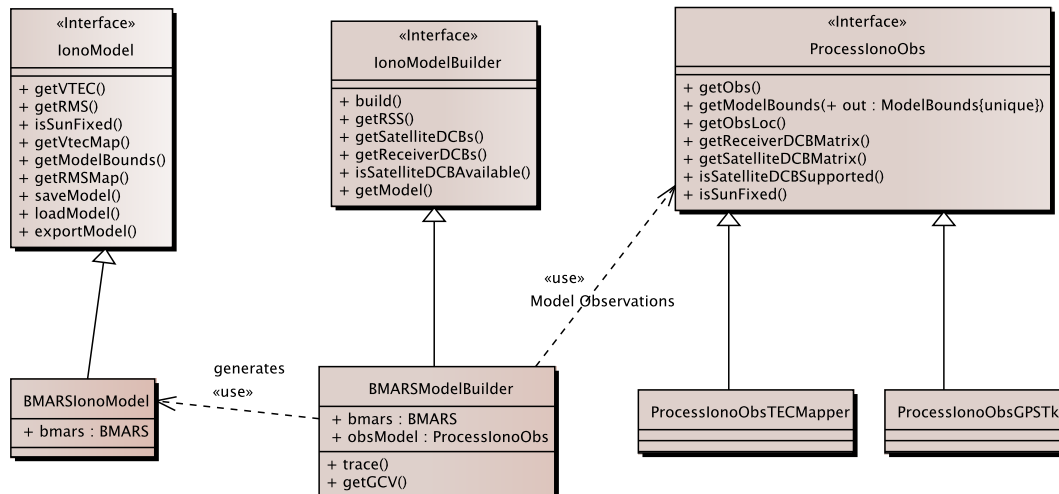


Figure 6.4: BMARS based Ionosphere Modeling class diagram

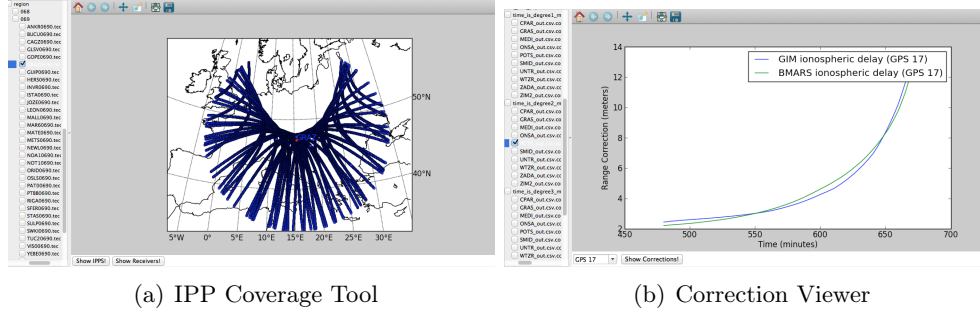
The classes provided by the module are listed below:

- **BMARSIonoModel:** implements the interface IonoModel by the underlying non-parametric or semi-parametric BMARS. The class is barely a wrapper for the BMARS model to predict VTEC values at the grid points and provide VTECMaps or export them to IONEX format.
- **BMARSModelBuilder:** implements the IonoModelBuilder interface given before. It uses the ProcessIonoObs interface to consume the properly modeled observations to either build a non-parametric or semi-parametric model. Actually, this class translates the observations and observation locations as well as DCB coefficient matrix into the interfaces required by BMARS to fit a non-parametric or semi-parametric model. Then returns a BMARSIonoModel around the estimated BMARS model.
- **ProcessIonoObsTecMapper:** This class, which implements the ProcessIonoObs interface, reads the TECMapper generated tec files and formats the values to be consumed by BMARSModelBuilder.
- **ProcessIonoObsGPSTk:** implements the ProcessIonoObs interface to provide a bridge between GPSTk processed RINEX observations and BMARSModelBuilder to use GPSTk provided ionospheric observables.

### 6.2.2.3 Utilities and Positioning

The utilities and positioning module consists of the static point positioning implementation in C++ with GPSTk software and the utilities that are used to either create the figures or analyse the results. Although there are other utility scripts developed for calling BMARSModelBuilder objects to create BMARS models, we will list the IPPCoverage utility and CorrectionViewer utility here. IppCoverage utility provides a GUI for displaying the IPPs generated by a specific receiver. It loads the TECMapper file and displays the IPPs with the reference station information. A screenshot of the program is given in Fig. 6.5(a). Also the coverage maps in Chapter 5 are generated by this utility. CorrectionViewer, on the other hand, gives a GUI for displaying the various corrections applied each epoch by the GPSTk software to code pseudo-ranges or carrier phases. The screen-shot given in Fig. 6.5(b) gives a screen-shot of the utility. Both utilities are developed in Python programming language with wxPython library.

The positioning software is developed for validation of VTEC maps in this study. It is a combination of a simple point positioning software implemented in C++ and a weighted least squares implementation of point positioning with code pseudo-ranges and carrier phases. The software mainly uses the IONEX formatted VTEC maps, RINEX formatted observation files and navigation files, SP3 formatted precise ephemeris files from IGS, P1P2 and P1-C1 DCB files from CODE and produces positioning estimates at each epoch as well as generates a corrections file. The correctionsfile contains the raw measurements plus the corrections applied by GPSTk software. These



(a) IPP Coverage Tool (b) Correction Viewer

Figure 6.5: IPP coverage and correction viewer utilities

data is then read by a Python routine which builds the observation equation in Chapter 5 to find a point positioning estimate and generates a report comparing the estimate to the true positions of the ground stations. The reports are converted to tables containing point positioning results in Chapter 5.

The important interfaces provided by GPSTk are given in Fig. 6.6. the `gpstk.proframe` package contains the GNSS data structures and various correction and modeling classes (Salazar, 2010). `ModelObs` class forms the approximate geometric ranges and generates basic observation equations. `IonoModelStore` handles the ionospheric models for the ionospheric delay calculation. `CorrectCodeBiases` class contains the routines related to correcting the code pseudo-ranges with respect to P1P2 and P1C1 DCBs.

The core library of GPSTk provides `IonexStore` which reads IONEX files, `TropModel` class which provides various troposphere models, `RinexObsStream` which can read and write RINEX streams and `SP3EphemerisStore` to read precise ephemerides from SP3 files. There are also many other utilities available in the package for which the reader is referred to the GPSTk website or Tolman et al. (2004).

The software package developed during the study will be a base for further development in ionosphere monitoring and mapping. Chapter 7 lists some further development directions for the software.

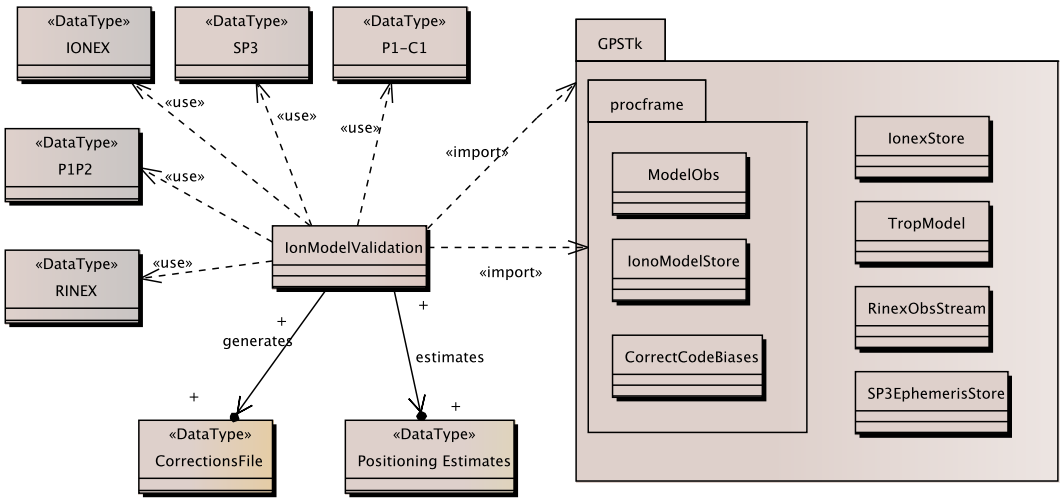


Figure 6.6: GPSTk based positioning module

## CHAPTER 7

### CONCLUSION

Global Navigation Satellite Systems (GNSS) especially the GPS are an invaluable source of information related to ionosphere. The geometry-free linear combination of the dual-frequency GPS observables depend only on the ionospheric range delay and Differential code biases of satellites and receivers. The ionospheric range delays, on the other hand, are related to the integral of electron density along the satellite-receiver ray-path. Thus, a Slant Total Electron Content (STEC) observations can be obtained which can be transformed into Vertical Total Electron Content by a mapping function assuming a Single Layer Model (SLM) (Hernández-Pajares et al., 2011). The main focus of the study was to find an adaptive and flexible regional spatio-temporal representation for the VTEC using ionospheric observations. In this study, a novel approach of non-parametric and semi-parametric VTEC modeling is proposed.

The objective of developing a non-parametric, flexible and adaptive VTEC modeling was achieved by adapting Multivariate Adaptive Regression Splines (MARS) algorithm for VTEC model estimation in 3D Sun-fixed reference frame. The method was successfully applied to regional modeling over Europe and the results have been published (Durmaz et al., 2010). Comparison of the results showed that the method can deliver VTEC models with less parameters. Moreover, the adaptivity of the algorithm with different data sizes and model sizes were also listed.

Another non-parametric method called Multivariate Adaptive Regression B-splines (BMARS) has been adapted to the regional non-parametric modeling of VTEC in an Earth-fixed reference frame. BMARS is an extension of the MARS algorithm that uses compactly supported B-splines. The developed technique was implemented in MATLAB and applied to regional VTEC modeling in North America as well as regional VTEC modeling over Europe. The results of VTEC modeling over North America have been published (Durmaz and Karslioglu, 2011). The BMARS VTEC models have been compared to both regional VTEC models based on tensor product of univariate B-splines and MARS. According to the results, BMARS delivered smoother models with less number of terms than MARS algorithm. The estimated VTEC maps and the resulting Root Mean Squared Error (RMSE) were similar to the other regional B-spline based method. The method was also tested for VTEC modeling over

Europe in an interval with a geomagnetic storm (Karslıođlu and Durmaz, 2012). The developed non-parametric VTEC modeling with BMARS successfully adapted to both quiet and active ionospheric conditions and delivered VTEC maps with less number of terms. Additionally, similar results have been observed with applications over different regions and the results were presented as posters in European Geosciences Union (EGU) General Assemblies in 2010, 2011 and 2012.

The main deficiency in non-parametric modeling is the requirement of the prior information on the receiver DCBs. To overcome this limitation, and to improve the spatio-temporal VTEC estimation process, a semi-parametric modeling approach was developed. The approach combines the parametric modeling and non-parametric modeling inside the same method. The parametric part of the model represents the receiver DCBs and the non-parametric part is related to the spatio-temporal VTEC representation. The developed technique was then implemented in Python programming language. The implementation have been further optimized by Cython static compiler interface and Numpy numerical computations package. Furthermore, the forward model building stage was enhanced by different stopping strategies, basis generation augmentation and scale based caching strategies. The further development options are listed in the future works section below.

The developed software package was then used to build regional 3D semi-parametric VTEC models on days 8th, 9th and 10th of March 2012 over Europe in an Earth-fixed reference frame. The days were selected to evaluate the performance of the method on both quiet and active ionospheric conditions, since there had been a geomagnetic storm on 9th of March. BMARS using B-splines of different order were used to generate VTEC maps in order to assess the selection of B-spline order. The resulting VTEC maps were compared to the VTEC maps generated by gridded tensor product of univariate B-splines. The VTEC maps were also compared to the Global Ionosphere Maps (GIM) published by CODE for the same days. Numerical and visual evaluation of the results indicated large local variations up to 10 TECU when compared to CODE GIMs. The RMS of variations between the semi-parametric BMARS maps and B-spline maps were less than 3 TECU. The results were also in parallel with the previously published ones. The BMARS algorithm delivers similar VTEC maps and RMSE values with less number of terms. This is due to the adaptive and flexible model building strategy applied in the forward stage. BMARS algorithm searches for best fitting basis functions to form the final VTEC model. Another interesting result of the comparison was that the RMSE values and VTEC maps generated with B-splines of different order were very close to each other. This result has been attributed to the success of the forward stage of the semi-parametric modeling.

The receiver DCB estimates of different BMARS models were also compared to the DCB estimates of regional B-spline based method and DCB estimations published by CODE. The resulting DCB estimates of BMARS and regional gridded B-splines were very close to each other. The maximum difference of DCB estimations with respect

to CODE were less than 3 ns. The main cause of this deviation is that the receiver DCBs are assumed to be daily constants in CODE GIMs whereas they are assumed to be constant during 2 hours for BMARS. The comparison of the results again showed that BMARS can deliver similar maps with regional gridded B-spline based method with less number of terms.

The developed method was then validated by cross-validation and single-frequency point positioning. The latter is very important since it is related to the intended use of the method. The 10-fold cross-validation results showed that the prediction error of the estimated VTEC models were around 1  $TECU^2$ . The GCV scores of the models were very close to the cross-validation results. This indicated that GCV is a powerful analytical tool to estimate the prediction error. One can expect that the prediction error of semi-parametric BMARS models are in the range of GCV scores if the level of the B-splines are limited with appropriate values. The validation with single-frequency point positioning was based on the use of VTEC maps generated by semi-parametric BMARS models and CODE GIMs. The VTEC maps were used to calculate the ionospheric delay corrections for the code pseudo-ranges and carrier-phases. The validation test was arranged so that only the ionospheric corrections were different for both models and the reference stations are not included in model building. The precise point positioning results have been calculated through JPL APPS service. The 3D distances of the estimated positions to the precise positions were compared. Although some of the reference stations were also used by CODE to estimate GIMs, the developed method gave better results for those stations as well. The semi-parametric VTEC maps in this study delivered better positions than CODE GIMs which can reach up to 8 dm difference for some stations. The point positioning results are promising for further research on single frequency precise point positioning with the method developed.

An extensible software framework was implemented in this study for semi-parametric ionospheric modeling, analysis and positioning. Python programming language has been used to develop the main parts of the algorithm. The open-source GPStk software was used for reading various exchange formats used in the GNSS community including but not limited to RINEX, IONEX, SP3 and DCB. The GPStk software was also used to model the correction terms and observation equations in point positioning. The developed library provides an extensible class hierarchy to support implementing new ionosphere modeling algorithms as well as using the existing ones. Since the software package is based on open-source components, it can be deployed without considering licensing issues.

Consequently, we conclude that the thesis has successfully achieved all of its objectives. The following section provides an outlook for the future research areas and improvements.

## 7.1 Future Work

Non-parametric and semi-parametric modeling with MARS and BMARS have already been implemented and tested in this thesis. However, the results and achievements lead to new research areas and further development directions which can be briefly listed as:

- The semi-parametric modeling can be further developed to include knot-optimization and parallelisation on Graphical Processing Units (GPU). An appropriate implementation of observation weighting will also be an important improvement.
- The software package can be extended by developing easy to use Graphical User Interfaces (GUI) for both ionosphere modeling and positioning. The single frequency point positioning software can be powered to include other correction terms to provide single frequency precise point positioning. Furthermore, an implementation of ambiguity resolution can be integrated into the software to achieve even better positioning results.
- The software can be converted to a web service with a web front-end. In this way, users of the web-service can upload their observations to obtain position estimations using various ionosphere models available. Additionally, using measurements from the EUREF-IP real-time pilot project [http://www.epncb.oma.be/euref\\_IP/](http://www.epncb.oma.be/euref_IP/) to provide near real-time VTEC maps could also give interesting results.
- The developed method and software package can be used to continuously generate VTEC maps using measurements from CORS networks particularly TUSAGA-AKTIF in Turkey. This kind of application not only provides a means for continuously monitoring the ionosphere, but also a valuable time series of ionospheric data can be obtained in the course of time, which will support future scientific research on space weather studies as well as others.

## REFERENCES

- Alcaydé, D. (Ed.) (2001). *Incoherent Scatter: Theory, Practice and Science*. EISCAT Scientific Association.
- Bakin, S., M. Hegland, and M. Osborne (1997). Computational techniques and applications conference: Can mars be improved with b-splines. *Computational Techniques and Applications*.
- Bakin, S., M. Hegland, and M. R. Osborne (2000). Parallel mars algorithm based on b-splines. *Computational Statistics* 15(4), 463–484.
- Bilitza, D. and B. Reinisch (2008). International reference ionosphere 2007: Improvements and new parameters. *Advances in Space Research* 42(4), 599 – 609.
- Brunini, C., A. Meza, F. Azpilicueta, and M. A. V. Zele (2004). A new ionosphere monitoring technology based on gps. *Astrophysics and Space Science* 290(3-4), 415–429.
- Dach, R., U. Hugentobler, P. Fridez, and M. Meindle (2007). *Bernese GPS Software Version 5.0*. University of Bern, Switzerland: Astronomical Institute.
- Dettmering, D. (2003). *The utilisation of the GPS for modelling the ionosphere in three dimensions*. Ph. D. thesis, Department of Geodesy and Geoinformatics, Universität Stuttgart, Technical Reports, Report Nr. 2003.1, in German.
- Dettmering, D., M. Schmidt, R. Heinkelmann, and M. Seitz (2011). Combination of different space-geodetic observations for regional ionosphere modeling. *Journal of Geodesy* 85(12), 989–998.
- Durmaz, M., M. O. Karslioglu, and M. Nohutcu (2010). Regional vtec modeling with multivariate adaptive regression splines. *Advances in Space Research* 46(2), 180 – 189.
- Durmaz, M. and M. O. Karslioglu (2011). Non-parametric regional {VTEC} modeling with multivariate adaptive regression b-splines. *Advances in Space Research* 48(9), 1523 – 1530.
- Friedman, J. H. (1991). Multivariate adaptive regression splines. *The Annals of Statistics* 19(1), 1–67.
- gps.gov (2013). The global positioning system.
- Hastie, T., R. Tibshirani, and J. H. Friedman (2001). *The elements of statistical learning data mining, inference and prediction*. New York: Springer-Verlag.

- Hernandez-Pajares, M. and J. M. J. J. Sanz (1999). New approaches in global ionospheric determination using ground gps data. *Journal of Atmospheric and Solar Terrestrial Physics* 61, 1237–1247.
- Hernández-Pajares, M., J. Juan, J. Sanz, Aragón-Ángel, A. García-Rigo, D. Salazar, and M. Escudero (2011). The ionosphere: effects, gps modeling and the benefits for space geodetic techniques. *Journal of Geodesy* 85(12), 887–907.
- Hernández-Pajares, M., J. Juan, J. Sanz, R. Orus, A. Garcia-Rigo, J. Feltens, A. Komjathy, S. Schaer, and A. Krankowski (2009). The igs vtec maps: a reliable source of ionospheric information since 1998. *Journal of Geodesy* 83(3-4), 263–275.
- Hernández-Pajares, M., J. M. Juan, and J. Sanz (1997). Neural network modeling of the ionospheric electron content at global scale using gps data. *Radio Science* 32(3), 1081–1089.
- Hofmann-Wellenhof, B., H. Lichtenegger, and E. Wasle (2008). *GNSS Global Navigation Satellite Systems GPS, GLONASS, Galileo more*. Austria: Springer.
- Iske, A., E. Quak, and M. S. Floater (Eds.) (2002). *Tutorials on Multiresolution in Geometric Modelling*. Springer.
- Jin, S. G., O. Luo, and P. Park (2008). Gps observations of the ionospheric f2-layer behaviour during the 20th november 2003 geomagnetic storm over south korea. *Journal of Geodesy* 82(12), 883–892.
- Jin, S. G., J. Park, J. Wang, B. Choi, and P. Park (2006). Electron density profiles derived from ground-based gps observations. *Journal of Navigation* 59(3), 395–401.
- Jin, S. G., H. P. Wang, and W. Y. Zhu (2004). Realtime prediction and monitoring of the total ionospheric electron content by means of gps observations. *Chinese Astronomy and Astrophysics* 28(3), 331–337.
- Kao, S., Y. Tu, W. Chen, D. J. Weng, and S. Y. Ji (2013). Factors affecting the estimation of gps receiver instrumental biases. *Survey Review* 45(328), 59–67.
- Karshoğlu, M. O. and M. Durmaz (2012). Regional spatio-temporal modeling of the ionospheric vertical total electron content (vtec) using multivariate adaptive regression b-splines (bmars). *Journal of Geodesy and Geoinformation* 1(1).
- Kelley, M. C. (2009). In *The Earth's Ionosphere: Plasma Physics Electrodynamics*. Academic Press.
- Koch, K.-R. (1999). *Parameter Estimation and Hypothesis Testing in Linear Model*. Springer-Verlag.
- Le, A., C. Tiberius, H. Marel, and N. Jakowski (2008). Use of global and regional ionosphere maps for single-frequency precise point positioning. In M. Sideris (Ed.), *Observing our Changing Earth*, Volume 133 of *International Association of Geodesy Symposia*, pp. 759–769. Springer Berlin Heidelberg.
- Liu, Z. and Y. Gao (2003). Ionospheric tec predictions over a local area gps reference network. *GPS Solutions* 8(1), 23–29.

Mannucci, A. J., B. D. Wilson, D. N. Yuan, C. H. Ho, U. J. Lindqwister, and T. F. Runge (1998). A global mapping technique for gps-derived ionospheric total electron content measurements. *Radio Science* 33(3), 565–582.

Mautz, R., J. Ping, K. Heki, B. Schaffrin, C. Schum, and L. Potts (2005). Efficient spatial and temporal representations of global ionosphere maps over japan using b-spline wavelets. *Journal of Geodesy* 78(11-12), 662–667.

Milborrow, S., derived from code by T. Hastie, and R. Tibshirani (2007). *Earth: Multivariate Adaptive Regression Spline Models*. R package available at <http://cran.r-project.org/src/contrib/Descriptions/earth.html>.

Misra, P. and P. Enge (2003). *Global Positioning System: Signals, Measurements, and Performance*. Massachusetts, USA: Ganga-Jamuna Press.

NIMA (2000, 1). Department of Defence World Geodetic System 1984, its definition and relationships with local geodetic systems. Technical report, National imagery and Mapping Agency, USA.

Nohutcu, M. (2009). *Development of a matlab based software package for ionosphere modeling*. Ph. D. thesis, The Graduate School of Natural and Applied Sciences of Middle East Technical University, Turkey.

Nohutcu, M., M. Karslioglu, and M. Schmidt (2010). B-spline modeling of vtec over turkey using gps observations. *Journal of Atmospheric and Solar-Terrestrial Physics* 72(7-8), 617 – 624.

Nohutcu, M., M. O. Karslioglu, B. Gucluer, M. Schmidt, C. Zeilhofer, Z. Zhang, and S. Ergintav (2007). Local modeling of tec using gps observations. In *TUJK Scientific Meeting, proceedings*, Ankara / Turkey.

Pallares, J., G. Ruffini, and L. Ruffini (2005). Ionospheric tomography using gnss reflections. *Geoscience and Remote Sensing, IEEE Transactions on* 43(2), 321–326.

Prölss, G. (2004). In *Physics of the Earth’s Space Environment: An Introduction*. Springer Berlin / Heidelberg.

Salazar, D. (2010). *Precise GPS-based position, velocity and acceleration determination: Algorithms and tools*. Ph. D. thesis, Depts. of Applied Mathematics IV and Applied Physics Universitat Politècnica de Catalunya (UPC), Spain.

Schaer, S. (1999). *Mapping and predicting the Earth’s ionosphere using the Global Positioning System*. Ph. D. thesis, University of Berne, Switzerland.

Schaer, S., W. Gurtner, and J. Feltens (1998). Ionex: The ionosphere map exchange format version 1. In *Proceedings of the IGS AC Workshop*.

Schmidt, M. (2007). Wavelet modeling in support of iri. *Advances in Space Research* 39(5), 932–940.

Schmidt, M., D. Bilitza, C. K. Shum, and C. Zeilhofer (2007a). Regional 4-d modeling of the ionospheric electron content. *Advances in Space Research* 42(4), 782–790.

- Schmidt, M., M. O. Karslioglu, and C. Zeilhofer (2007b). Regional multi-dimensional modeling of the ionosphere from satellite data. In *TUJK Scientific Meeting, proceedings*, Ankara / Turkey.
- Schunk, R. W., L. Scherliess, J. J. Sojka, D. C. Thompson, D. N. Anderson, M. Codrescu, C. Minter, T. J. Fuller-Rowell, R. A. Heelis, M. Hairston, and B. M. Howe (2004). Global assimilation of ionospheric measurements (gaim). *Radio Science* 39(1), n/a–n/a.
- Seeber, G. (2003). *Satellite Geodesy*. Berlin, Germany: de Gruyter.
- Tolman, B., R. B. Harris, T. Gaussiran, D. Munton, J. Little, R. Mach, S. Nelsen, and B. Renfro (2004, September). The GPS Toolkit: Open Source GPS Software. In *Proceedings of the 16th International Technical Meeting of the Satellite Division of the Institute of Navigation*, Long Beach, California.
- Wen, D., Y. Yuan, J. Ou, X. Huo, and K. Zhang (2007). Three-dimensional ionospheric tomography by an improved algebraic reconstruction technique. *GPS Solutions* 11(4), 251–258.
- Wielgosz, P., D. A. Grejner-Brzezinska, and I. Kashani (2003). Regional ionosphere mapping with kriging and multiquadric methods. *Journal of Global Positioning Systems* 2(1), 48–55.
- Xu, G. (2007). *GPS, Theory, Algorithms and Applications*. Springer-Verlag.
- Yuan, Y. and J. Ou (2002). Differential areas for differential stations (dads): A new method of establishing grid ionospheric model. *Chinese Science Bulletin* 47(12), 1033–1036.
- Zeilhofer, C. (2008). Multi-dimensional b-spline modeling of spatio-temporal ionospheric signals. *German Geodetic Commission, series A, 123, München*.

# APPENDIX A

## RECEIVER DCB ESTIMATES

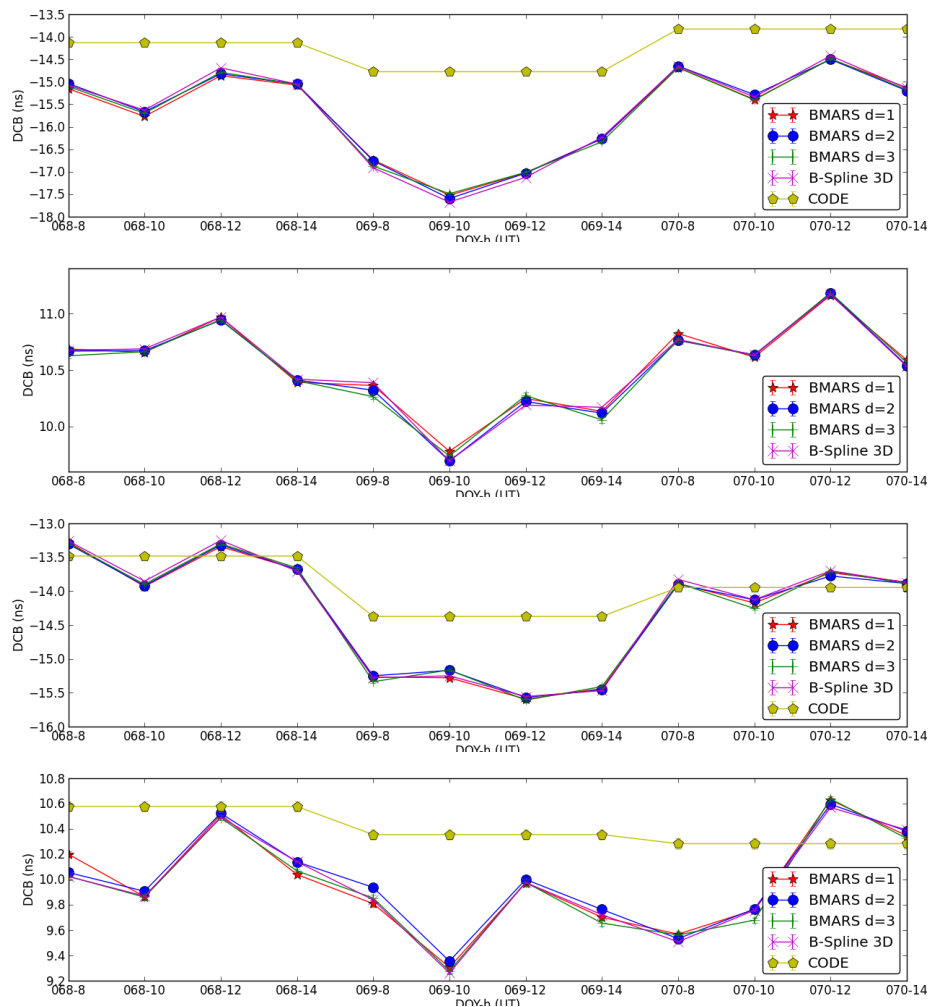


Figure A.1: DCB estimates for ground stations (ANKR, BUCU, CAGZ and GLSV from top to bottom) for each days

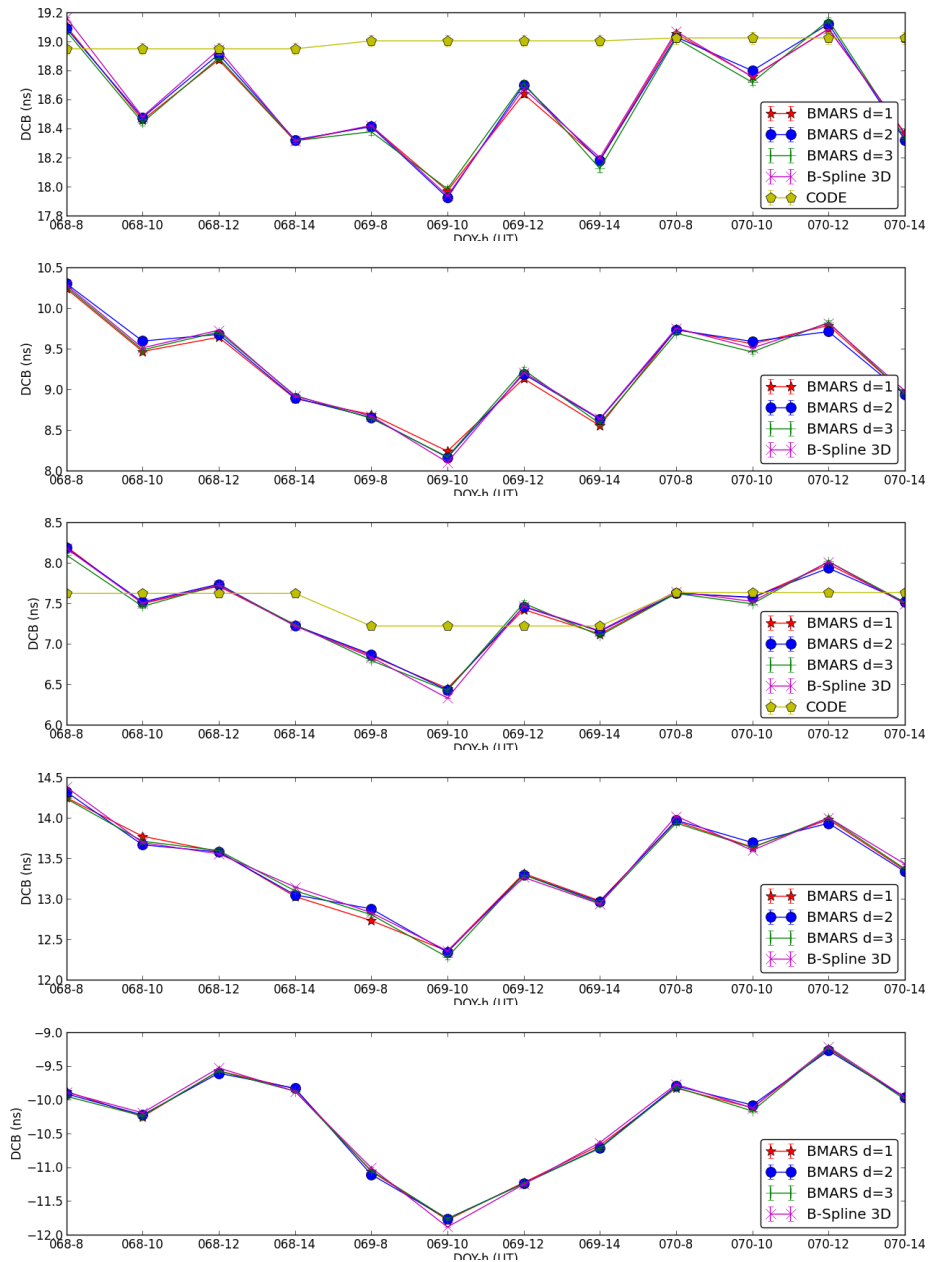


Figure A.2: DCB estimates for ground stations (GRAZ, GUIP, HERS, INVR and ISTA from top to bottom) for each days

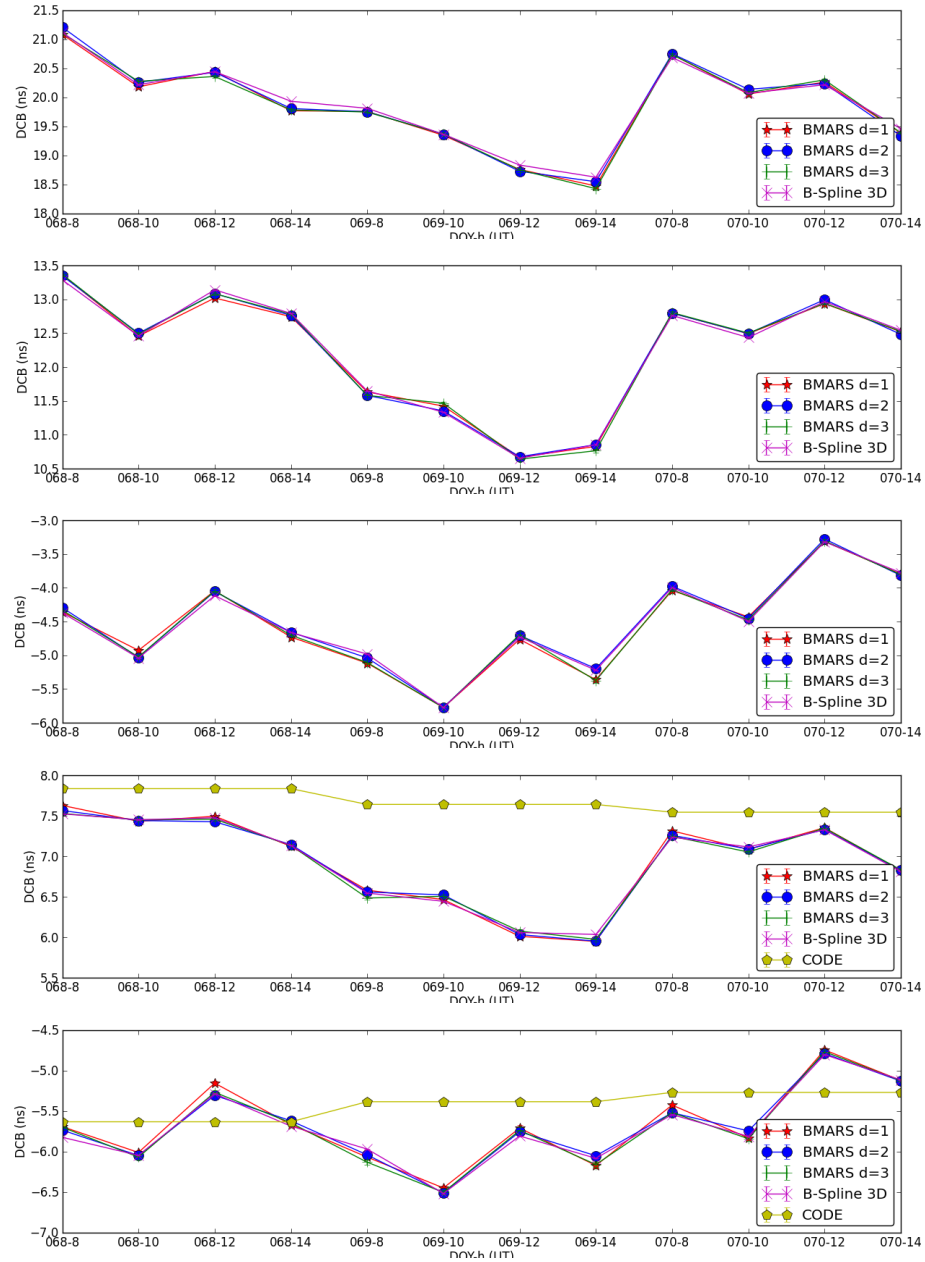


Figure A.3: DCB estimates for ground stations (LEON, MALL, MAR6, MATE and METS from top to bottom) for each days

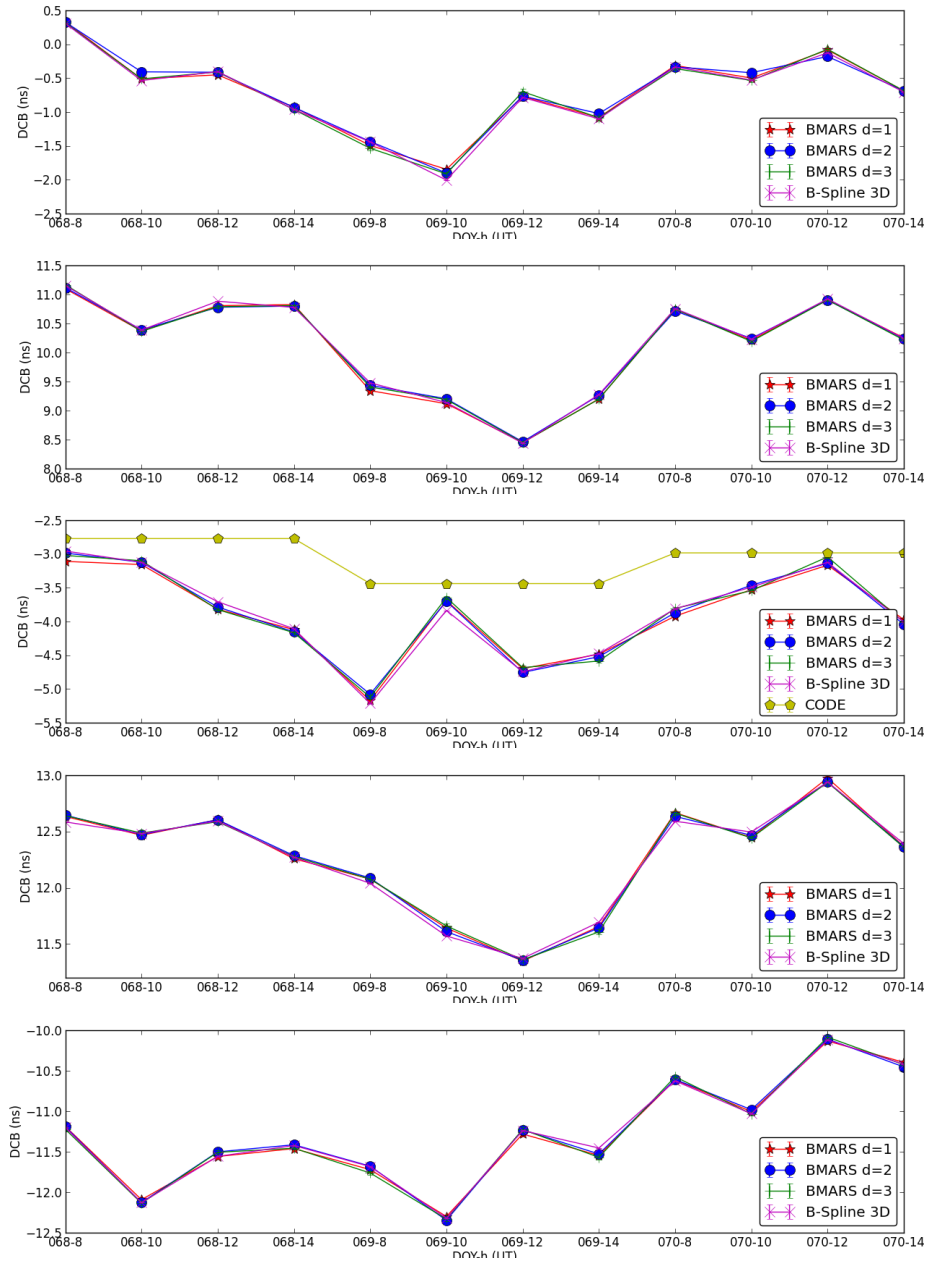


Figure A.4: DCB estimates for ground stations (NEWL, NOA1, NOT1, ORID and OSLS from top to bottom) for each days

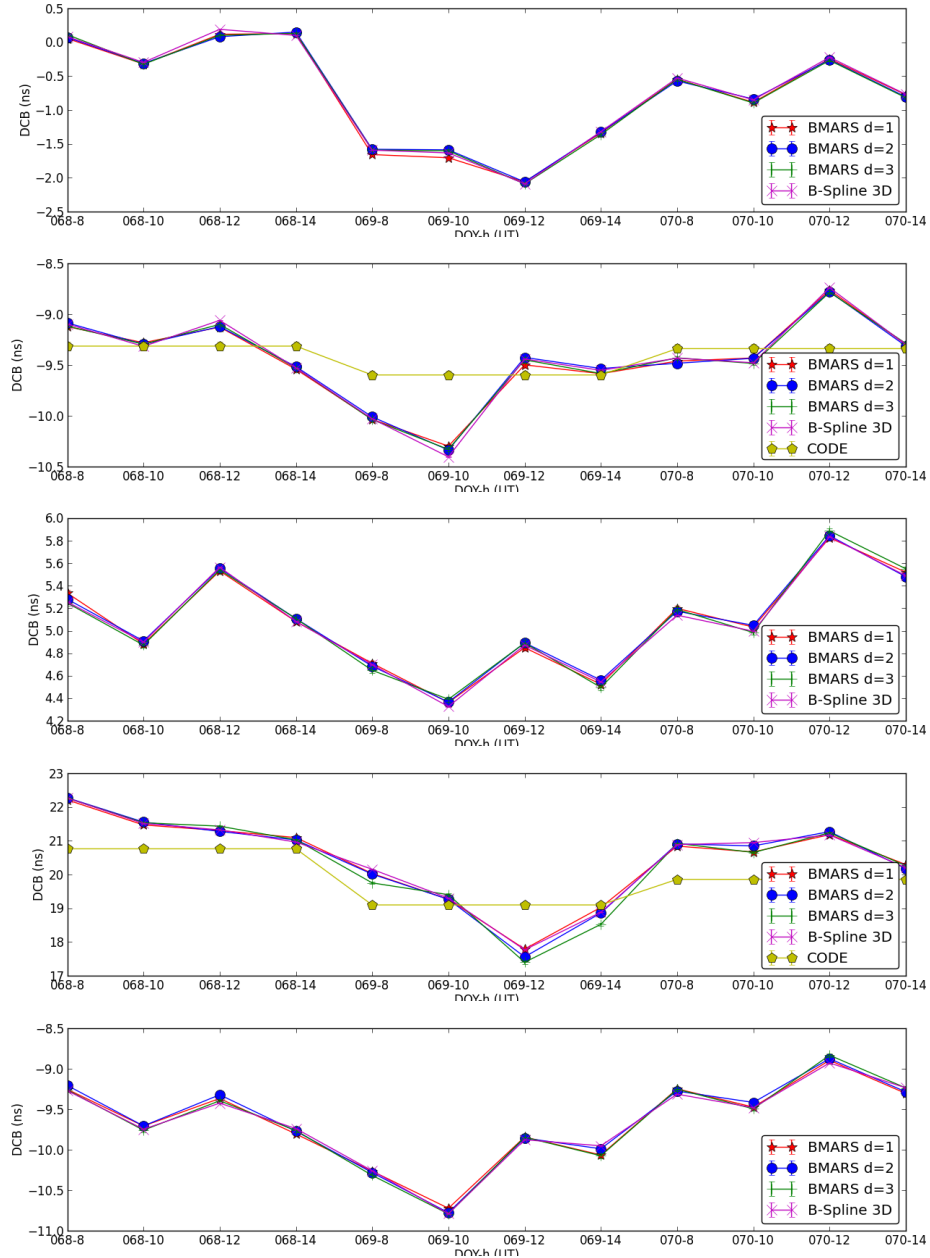


Figure A.5: DCB estimates for ground stations (PAT0, PTBB, RIGA, SFER and STAS from top to bottom) for each days

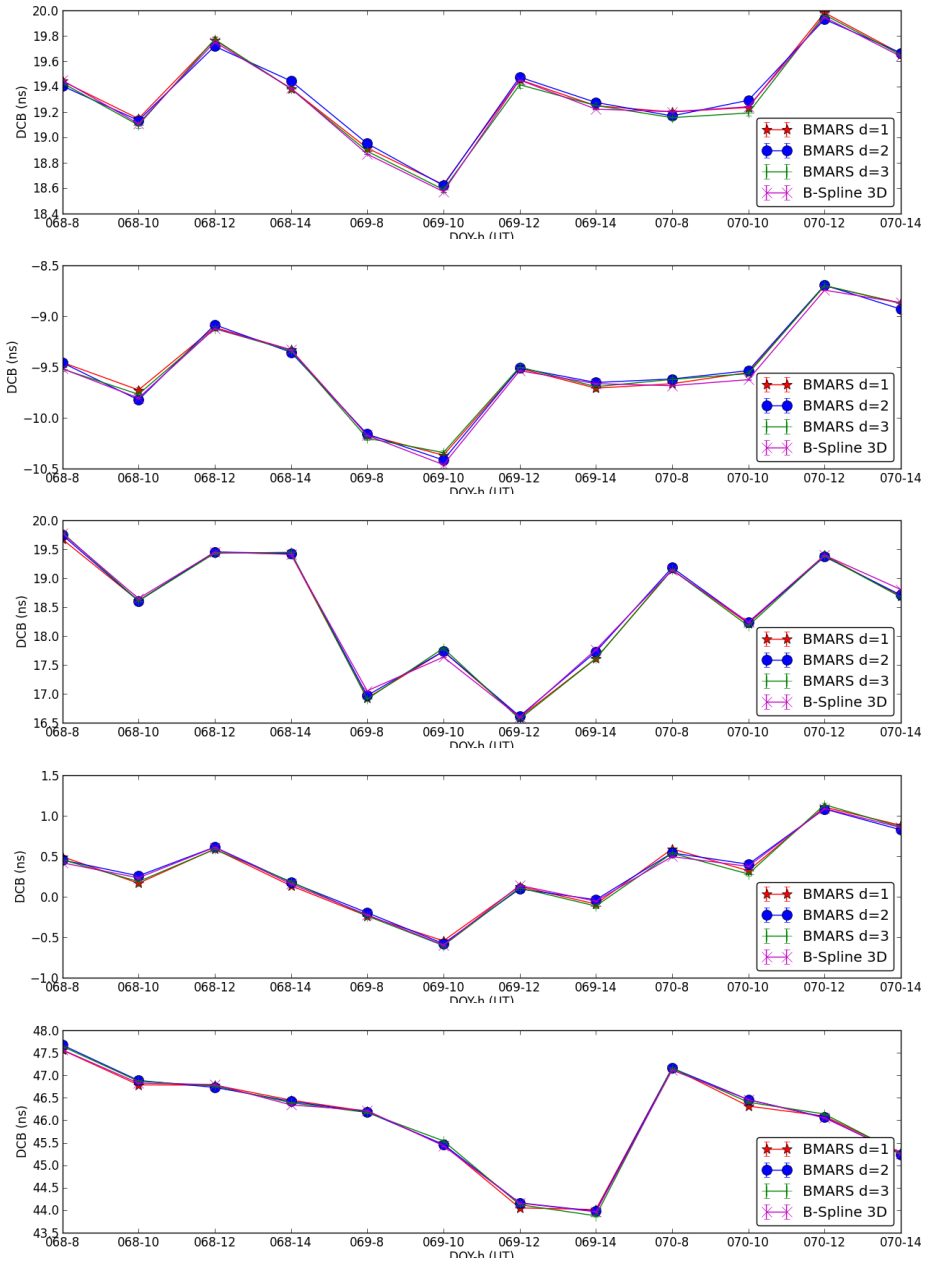


Figure A.6: DCB estimates for ground stations (SULP, SWKI, TUC2, VIS0 and YEBE from top to bottom) for each days

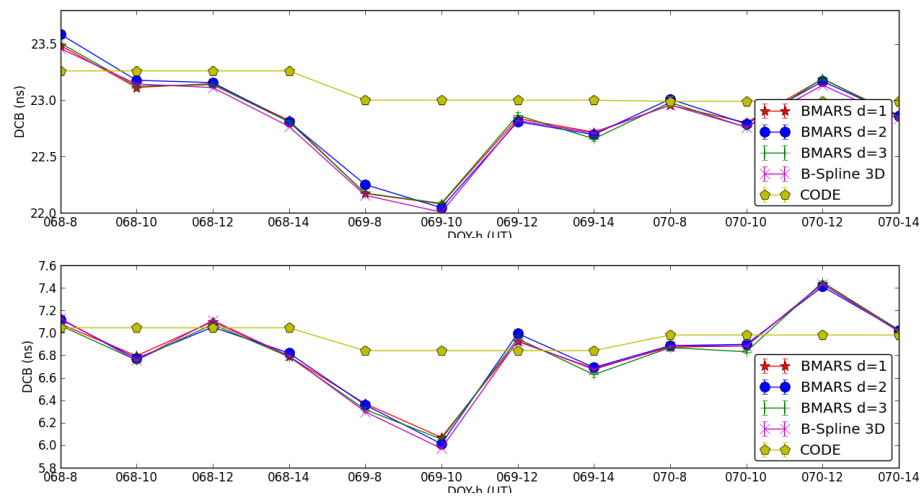


Figure A.7: DCB estimates for ground stations ZIMM and GOPE for each days



# CURRICULUM VITAE

## PERSONAL INFORMATION

**Surname, Name:** DURMAZ, Murat

**Nationality:** Turkish (TC)

**Date and Place of Birth:** 20/11/1978, Zonguldak

**Marital Status:** Married

**Phone:** 533 711 12 49

**Fax:**

## EDUCATION

Degree	Institution	Year of Graduation
M.S.	METU Geodetics and Geographic Inf. Tech.	2007
B.S.	METU Computer Engineering	2002
High School	Mehmet Çelikel High School	1996

## PROFESSIONAL EXPERIENCE

Year	Place	Enrollment
1999-2000	Sabancı university	Software Developer
2001-2013	BILGI A.Ş	Software Technologies Department Manager

## PUBLICATIONS

### International Reviewed Papers (SCI)

Murat Durmaz, Mahmut Onur Karslioglu, Metin Nohutcu, Regional VTEC modeling with multivariate adaptive regression splines, Advances in Space Research, Volume 46, Issue 2, 15 July 2010, Pages 180-189, ISSN 0273-1177, <http://dx.doi.org/10.1016/j.asr.2010.02.030>.

Murat Durmaz, Mahmut Onur Karslioglu, Non-parametric regional VTEC modeling

with Multivariate Adaptive Regression B-Splines, Advances in Space Research, Volume 48, Issue 9, 1 November 2011, Pages 1523-1530, ISSN 0273-1177, <http://dx.doi.org/10.1016/j.asr.2011.06.031>.

### **International Reviewed Papers**

Karslioglu M.O., Durmaz, M., “Regional spatio-temporal modeling of the ionospheric Vertical Total Electron Content (VTEC) using Multivariate Adaptive Regression B-Splines (BMARS)”, Journal of Geodesy and Geoinformation, Vol.1, No. 1, pp.9-16, May 2012

### **International Conference Publications**

Karslioglu M.O., Durmaz M., Regional Ionosphere Modeling using Multivariate Adaptive Regression B-Splines(BMARS), Geophysical Research Abstracts, Vol. 14, EGU 2012-3604, 2012, EGU General Assembly 2012

Karslioglu M.O., Murat Durmaz M., Multivariate Adaptive Regression B-Splines for Regional VTEC Modeling), Geophysical Research Abstracts Vol. 13, EGU 2011-9871, 2011, EGU General Assembly 2011

Karslioglu M.O., Durmaz M., Nohutcu M., “Regional VTEC Modeling over Turkey Using MARS (Multivariate Adaptive Regression Splines)”, Geophysical Research Abstracts Vol. 12, EGU 2010-6251, 2010, EGU General Assembly 2010

### **National Conference Publications**

Durmaz M., Karshoğlu M.O., “Çok Değişkenli Uyabilen Spline Regresyonu (MARS) Kullanarak Bölgesel İyonosfer Modellemesi”, 5. Ulusal Mühendislik Ölçmeleri Sempozyumu, 20-22 Ekim 2010 ZKÜ Merkez Kampüsü, Zonguldak